



HAL
open science

Behavior of scratched hydrodynamic journal bearings : a finite volume numerical analysis

Tran Anh Vo

► **To cite this version:**

Tran Anh Vo. Behavior of scratched hydrodynamic journal bearings: a finite volume numerical analysis. Mechanical engineering [physics.class-ph]. Université de Poitiers, 2021. English. NNT : 2021POIT2275 . tel-03391573

HAL Id: tel-03391573

<https://theses.hal.science/tel-03391573>

Submitted on 21 Oct 2021

HAL is a multi-disciplinary open access archive for the deposit and dissemination of scientific research documents, whether they are published or not. The documents may come from teaching and research institutions in France or abroad, or from public or private research centers.

L'archive ouverte pluridisciplinaire **HAL**, est destinée au dépôt et à la diffusion de documents scientifiques de niveau recherche, publiés ou non, émanant des établissements d'enseignement et de recherche français ou étrangers, des laboratoires publics ou privés.

THESE

Pour l'obtention du Grade de

DOCTEUR DE L'UNIVERSITE DE POITIERS

(Faculté des Sciences Fondamentales et Appliquées)
(Diplôme National - Arrêté du 25 mai 2016)

École Doctorale :

Sciences et ingénierie en matériaux, mécanique, énergétique et aéronautique - SIMMEA

Secteur de Recherche : Génie mécanique.

Présentée par :

Tran-Anh VO

BEHAVIOR OF SCRATCHED HYDRODYNAMIC JOURNAL BEARINGS:
A FINITE VOLUME NUMERICAL ANALYSIS

Directeur de Thèse : Jean BOUYER
Co-directeur de Thèse : Michel FILLON

Soutenance prévue le 23 juin 2021

devant la Commission d'Examen

JURY

BOU-SAÏD	Benyebka	Professeur	INSA de Lyon	Rapporteur
CHANGENET	Christophe	MdC, HdR	ECAM Lyon	Rapporteur
BOUYER	Jean	MdC, HdR	Université de Poitiers	Examineur
BRUNETIERE	Noel	Directeur de Recherche	Université de Poitiers	Examineur
FILLON	Michel	Directeur de Recherche	Université de Poitiers	Examineur
MASSI	Francesco	Professeur	Sapienza Università di Roma	Examineur
PAP	Balint	Ph. D	Safran Transmission Systems	Examineur
SMERDOVA	Olga	MdC	ISAE ENSMA	Examinatrice

Résumé étendu de la thèse

Dans cette thèse, un modèle thermohydrodynamique (THD) a été développé et validé ; il permet de simuler les comportements de paliers lisses rayés. Le modèle prend en compte la géométrie complète connue des profils de rayures ainsi que les effets thermiques. Le modèle a été validé avec plusieurs séries de données provenant à la fois de la littérature scientifique et des expériences menées à l'Institut Pprime.

Dans le chapitre 1, nous présentons une brève vue d'ensemble des paliers hydrodynamiques avec l'histoire de leur développement ainsi qu'une introduction aux divers types de dommages existant dans les paliers hydrodynamiques. Nous présentons également une revue bibliographique de l'état actuel des études sur les comportements des paliers lisses rayés, qui est le principal objectif d'étude de cette thèse.

Le chapitre 2 est consacré à une analyse théorique du problème avec toutes les équations nécessaires pour déterminer une solution thermohydrodynamique complète pour les paliers lisses multilobes lubrifiés avec un fluide incompressible. L'équation de Reynolds généralisée pour les champs de pression dans le film, l'équation d'énergie pour la température du fluide, l'équation de Laplace de conduction thermique pour les solides environnants, les conditions aux limites pour la pression et la température, et les paramètres globaux du palier, sont tous présentés.

Dans le chapitre 3, nous montrons une analyse numérique pour le modèle avec la discrétisation des équations différentielles partielles présentées dans le chapitre 2 en utilisant la méthode des volumes finis. Les systèmes d'équations sont résolus en utilisant la méthode de Stone (SIP- Strong Implicit Procedure) vectorisée, ce qui a permis d'améliorer significativement le temps de calcul. Différentes techniques de maillage pour le film fluide sont décrites,

en se concentrant particulièrement sur la discontinuité du domaine du film dans la direction axiale où se trouvent les rayures. Un programme Fortran a été développé et vérifié en le comparant avec des études issues des revues spécialisées dans le domaine de la tribologie. Les résultats de la simulation ont montré de bons accords avec les résultats publiés dans la littérature scientifique.

Le chapitre 4 est dédié à la validation du modèle THD pour un palier lisse avec trois cas de profondeurs de rayure différentes (peu profonde, moyenne et profonde, à comparer avec le cas sans rayure) avec un large éventail de conditions de fonctionnement, c'est-à-dire une large gamme de charges appliquées et de vitesses de rotation. Les résultats de comparaison obtenus montrent tout d'abord une très bonne concordance dans la distribution de la pression, tant au niveau de la tendance que des valeurs ; deuxièmement, une très bonne concordance dans la distribution de la température pour le lobe faiblement chargé, tant au niveau de la tendance que des valeurs, et une concordance moyenne dans la distribution de la température pour le lobe fortement chargé. Enfin, il est observé un bon accord sur la prédiction des paramètres globaux de performance du palier avec les résultats de la littérature. Il est par cela confirmé que l'existence de rayures a modifié les distributions de pression et de température. L'influence de la rayure est plus significative sur les pressions mais moins significative sur les températures (observé dans les expériences et confirmé avec le modèle THD étudié). La profondeur de la rayure est un paramètre crucial qui influence fortement les performances du palier rayé. Il est également important de noter que les résultats de comparaison obtenus sont très cohérents et ne dépendent pas de la profondeur de la rayure.

Le chapitre 5 s'intéresse généralement à l'influence d'autres paramètres de la géométrie de la rayure (largeur de la rayure, position) sur les performances des paliers lisses rayés, les profils de vitesse et les limites du modèle. Une étude de cas réel est également présentée

avec plusieurs rayures et différentes profondeurs et largeurs de rayures. Plusieurs résultats importants sont obtenus : Premièrement, la largeur de la rayure a une influence sur le palier mais seulement significative lorsque la rayure est large. Deuxièmement, la position de la rayure a une influence moins significative sur la distribution de la pression et de la température et l'influence diminue lorsque la rayure s'éloigne de la zone du plan médian du palier car elle est située dans des zones de plus faible pression hydrodynamique. Troisièmement, le nombre de rayures a une influence moins significative sur la distribution de la pression et de la température pour les cas de rayures peu profondes. Quatrièmement, une vitesse négative, qui correspond à un écoulement inverse, est observée dans les régions rayées au niveau de l'entrée du lobe chargé. En outre, il a été constaté qu'il existe une limite ou une valeur critique dans la profondeur de rayure et la charge appliquée pour les paliers rayés dans certaines conditions de fonctionnement. L'augmentation de la profondeur de rayure ou de la charge appliquée, même minime, peut entraîner une chute soudaine de l'épaisseur minimale du film calculée (proche de zéro), ce qui conduit à des valeurs très élevées de la pression calculée et empêche la convergence du modèle. Les modèles hydrodynamiques (c'est-à-dire ne tenant pas compte des effets thermiques et supposant donc un régime isotherme) et THD peuvent aboutir à des solutions très différentes pour les paliers rayés. Dans certaines circonstances, le modèle THD ne peut pas converger vers des solutions car les configurations de paliers ne sont pas admissibles, mais des solutions peuvent être obtenues en utilisant des modèles hydrodynamiques. Cependant, les résultats isothermes obtenus dans le cas étudié ont montré une grande divergence dans la distribution de la pression par rapport aux données expérimentales. Par conséquent, si les résultats isothermes doivent être utilisés sur le terrain pour observer la tendance ou les valeurs exactes, une attention particulière doit être accordée.

D'après les résultats obtenus, nous pensons que le modèle THD est capable de simuler l'influence des rayures sur les performances des paliers lisses rayés : l'épaisseur du film, les débits, la distribution de la température, l'excentricité relative, l'angle d'attitude et d'autres paramètres pertinents. En outre, il permet de déterminer les éventuelles limites critiques des conditions de fonctionnement des paliers lisses rayés et celles de la géométrie des rayures. Nous espérons que le modèle pourra être utilisé comme un outil utile pour améliorer notre compréhension du comportement des paliers lisses rayés et un outil de prédiction pour les utilisateurs de paliers afin d'éviter tout dommage sérieux dans les machines tournantes. Bien que la validation montre de bons accords entre les données calculées et mesurées, des études plus précises prenant en compte les déformations et l'échange thermique entre le coussinet et le système de support du palier devront être entreprises. En outre, le mésalignement peut avoir une influence sur la distribution de pression, particulièrement quand les profils de rayures ne sont pas symétriques et donc il doit être étudié, comme précisé dans une étude précédente [41]. Enfin, le modèle actuel avec les solutions généralisées de Reynolds a encore des limites, il peut être invalide pour les paliers endommagés de façon critique. Dans ces configurations, lorsque le palier rayé fonctionne dans des conditions sévères, il peut introduire plusieurs paramètres inconnus qui peuvent rendre l'équation généralisée de Reynolds invalide. Par conséquent, des analyses et des études plus approfondies sur ce problème devraient être envisagées dans nos futures investigations.

Acknowledgements

I would like to deeply thank my thesis directors, Dr. Jean BOUYER and Dr. Michel FILLON, for their guidance and support, valuable advice, and encouragement through my Ph.D.

I would like to thank Professor Benyebka BOU-SAÏD from the INSA de Lyon and Dr. Christophe CHANGENET from the ECAM Lyon for reviewing and evaluating my thesis.

I would like to thank Professor Francesco MASSI, Dr. Noel BRUNETIERE, Dr. Olga SMERDOVA and Dr. Balint PAP, for being members of my defense jury and their contribution.

Thank you to all the members of the lab who have supported me since my first day in the lab.

Thank you to all my friends who have had to support me through the years.

Finally, thank you from the bottom of my heart to all the members of my family who have always supported and encouraged me throughout my PhD years.

Contents

RESUME ETENDU DE LA THESE	III
ACKNOWLEDGEMENTS	1
CONTENTS.....	3
NOMENCLATURE.....	5
INTRODUCTION.....	7
CHAPTER 1. LITERATURE REVIEW	11
1.1. OVERVIEW OF JOURNAL BEARINGS	11
1.2. OVERVIEW OF STUDIES ON THERMAL EFFECTS IN HYDRODYNAMIC BEARINGS.....	14
1.3. DAMAGE IN HYDRODYNAMIC BEARINGS	17
1.4. OVERVIEW OF STUDIES ON SCRATCHED JOURNAL BEARINGS.....	22
1.5. CONCLUSIONS	25
CHAPTER 2. THEORETICAL ANALYSIS	27
2.1. GEOMETRICAL CHARACTERISTICS OF A LOBE BEARING.....	27
2.2. EQUATIONS OF HYDRODYNAMIC LUBRICATION	32
2.3. EQUATIONS IN THERMOHYDRODYNAMIC (THD) REGIME	39
2.4. BOUNDARY CONDITIONS	42
2.5. BEARING GLOBAL PARAMETERS	46
2.6. CONCLUSIONS	49
CHAPTER 3. NUMERICAL ANALYSIS	51
3.1. DISCRETIZATION	51
3.2. SOLUTIONS OF SYSTEM OF EQUATIONS.....	55
3.3. GEOMETRICAL STUDY	66
3.4. PROGRAM FLOW CHART AND VERIFICATIONS.....	73
3.5. CONCLUSIONS	86
CHAPTER 4. VALIDATION.....	87
4.1. PRESENTATION OF EXPERIMENT-SETUP AND VALIDATION DATA	87
4.2. VALIDATION FOR BEARINGS WITH ONE SCRATCH	89
4.3. VALIDATION FOR BEARINGS WITH TWO SCRATCHES.....	106
4.4. CONCLUSIONS	112
CHAPTER 5. NUMERICAL STUDIES	113
5.1. AIM OF THE STUDY.....	113
5.2. EFFECT OF SCRATCH WIDTH	113
5.3. EFFECT OF SCRATCH POSITION	117
5.4. FINDING CRITICAL VALUE OF SCRATCH DEPTH FOR THE SCRATCHED BEARING	120
5.5. FINDING CRITICAL VALUE OF APPLIED LOAD FOR THE SCRATCHED BEARING	122

5.6. NEGATIVE VELOCITY IN THE SCRATCH REGIONS.....	123
5.7. STUDY ON MULTIPLE SCRATCHED BEARINGS	127
5.8. CONCLUSIONS	136
CONCLUSIONS.....	139
PERSPECTIVES	143
BIBLIOGRAPHY	145
LIST OF FIGURES.....	151
LIST OF TABLES.....	155
APPENDIX A	157
RESUME	163
ABSTRACT	163

Nomenclature

C	horizontal clearance	m
C_b	vertical clearance	m
C_p	lubricant specific heat	J/Kg·°K
d	shaft diameter	m
d_{bext}	bush outer diameter	m
d_{ext}	support ring outer diameter	m
d_{bh}	horizontal bush inner diameter	m
d_{bv}	vertical bush diameter	m
E	Young's Modulus	Pa
F	load projection	N
h	film thickness	m
H_c	convective heat transfer coefficient	W/m ² ·°K
K	thermal conductivity of the lubricant	W/m·°K
K_b	thermal conductivity of the bush	W/m·°K
L	bearing length	m
L_s	position of scratches	
m	bearing preload	
N_x	number of volumes in the circumferential direction	
N_y	number of volumes in the film thickness direction	
N_z	number of volumes in the axial direction	
N_u	Nusselt number	
O	bearing center	
O_a	shaft center	
P	pressure	Pa
P_s	supply pressure at inlet	Pa
P_{ref}	reference pressure	Pa
r	filling	
Q_{in}	entering flow rate	m ³ /s
Q_{out}	recirculating flow rate	m ³ /s
Q_{supply}	supply flow rate	m ³ /s
Q_{axial}	axial leaking flow rate	m ³ /s
R	shaft radius	m

R_l	lobe radius	m
T	oil temperature	°C
T_{shaft}	shaft temperature	°C
T_{supply}	lubricant supply temperature	°C
T_{amb}	ambient temperature	°C
T_{in}	inlet temperature of the lobe	°C
$T_{measure}$	measured temperature	°C
T_{wall}	wall temperature	°C
T_{out}	outlet temperature of the lobe	°C
$T_{initial}$	initial temperature	°C
U	shaft speed	rpm
W	bearing load	N
x	coordinate system in the circumferential direction	m
y	coordinate system normal to the direction of rotation	m
z	coordinate system in axial direction	m

GREEK LETTERS

α	thermal expansion coefficient	K ⁻¹
ε	relative eccentricity	
θ	angular position in the lobe coordinate system	degree
θ^*	angular position in the local coordinate system	degree
μ	lubricant viscosity	Pa·s
ρ	lubricant density	kg/m ³
Σ	convergence criteria	
Φ	index function	
ϕ_0	attitude angle	degree
Ψ	global rotation angle	degree
Ω	relaxation coefficient	
δ	scratch depth	m

ABBREVIATION

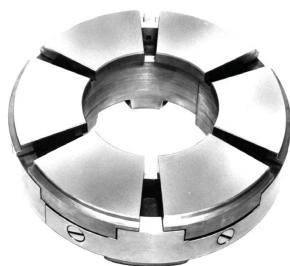
HD	Hydrodynamic
THD	Thermo-Hydro-Dynamic
PDE	Partial differential equation

Introduction

Bearings are important components in rotating machinery. The purposes of bearings are to guide and support rotating shafts and reduce friction between moving parts. Two main types of bearing are rolling element bearing and hydrodynamic bearing (Fig. 1.1). Rolling bearings provide rolling contact between moving parts with rolling elements such as balls or rollers that separate moving parts. Instead, the hydrodynamic bearings replace the rolling elements by lubricants and provide sliding contact between moving parts. Two main types of hydrodynamic bearings are thrust bearing and journal bearing. Thrust bearing supports axial forces while journal bearing supports axial forces.



(a) Rolling element bearings



Thrust bearing



Journal bearings

(b) Hydrodynamic bearings

Figure 1.1. Types of bearing.

Journal bearings are one of the most common types of hydrodynamic bearings primarily used to support high-speed rotating machinery, including turbines and compressors, pumps, and motors, etc. because of their superior durability and high load carrying capacity, and efficiency. Figure 1.2 presents one of the most basic type of journal bearings, a plain journal bearing. A journal bearing comprises a journal (a part of the shaft which is housed by the bush) which rotates in a supporting bush with a thin lubricant film separating them. The inner surface of the bush usually lined with soft bearing materials such as soft tin and lead Babbitt. Lubricants used for journal bearings can be liquid, gas, or grease, depending on the application.

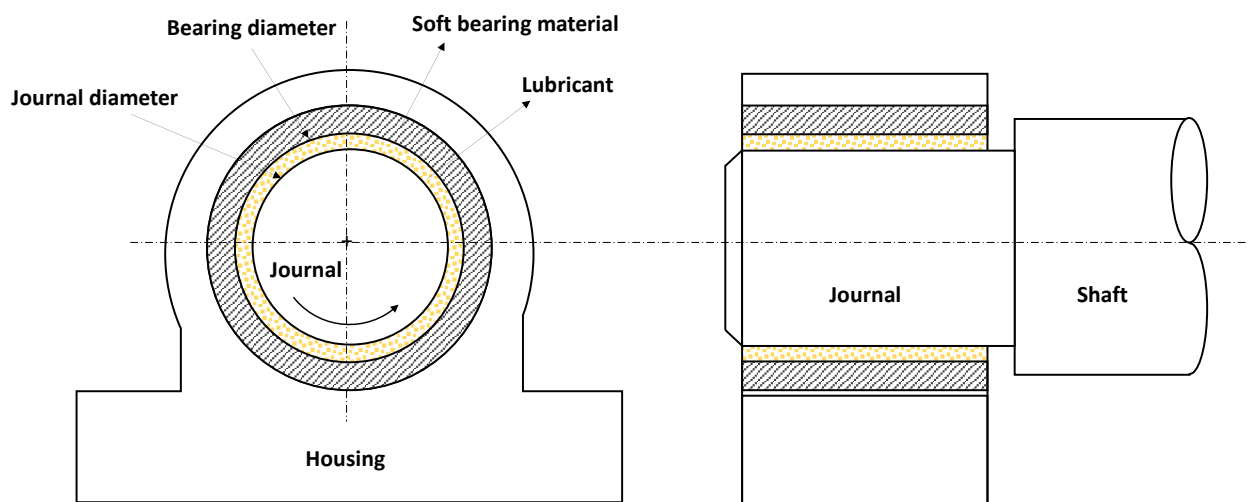


Figure 1.2. Plain journal bearing.

Well-designed journal bearings can operate efficiently for years with minimum maintenance. However, when suffering damages or failures which degrade their performance, the consequences can be catastrophic and lead to the damage of the machine or the interruption of plant operation. Forms and types of damages in journal bearings are various including damages due to the influence of particles (wear, scoring, wire wooling, corrosion,

etc.), fatigue damages, damages due to overheating, chemical corrosion, and scratches on one or the two surfaces of the bearing. The scratch is the major type of damage in journal bearings. It is observed in industrial applications that after some time of operation, especially in severe conditions, hydrodynamic bearings are often degraded because of the presence of scratches. This can cause a loss of load capacity, significantly reducing the oil film thickness because of the decrease in the active surface area. Due to the overall complexity of rotating machinery and the bearings themselves, the causes of damages are not easy to identify. To minimize the consequences of failures in journal bearings, it is important to detect the damages, identify and establish its causes and have maintenance plans to remedy those damages (checking the system, repair or replace damaged components, etc. depending on the types and state of damages). Other approaches can be considered, such predicting and preventing the failures before they happen if it is possible. To pursue these approaches, understating the complex behavior and performance of damaged journal bearings is required. The purpose can be acquired by both of numerical simulations and experiment testing. Numerical simulations help to understand the behavior of a damaged journal bearing under the influence of varying the design parameters (applied load, speed, temperature, defect geometry, etc.). The degree of reliability of simulation results is directly related to the degree of the processes of verification and validation, and these processes are mandatory for a numerical model. While verifications are often performed by comparing the simulations with previous validated results, validations are performed by comparing them with experimental tests. By understating the complex behavior damaged journal bearings both in simulations and experiments, it can help bearing users to prevent potential failures by limiting the operating conditions i.e. applied load, rotational speed, depending on the degree of failures, or deciding if the damaged bearings can still be used or should be replaced, etc.

This work contributes to the overall knowledge of the behaviors of damaged journal bearings. In particular, the influence of presence of the scratches on the performance of scratched journal bearings. A numerical thermohydrodynamic model has been developed, it is able to simulate the influence of scratches on the characteristics of the bearing, including the pressure, flow rates, temperature, operating conditions, and other relevant parameters. It is also able to determine limits of operation of scratched journal bearings. The numerical analysis of the performance of scratched journal bearings are also provided with a variety of configurations of the scratch geometry and operating conditions.

The work in this thesis was undertaken with the goals of 1) validation of a thermohydrodynamic model that is able to simulate scratched journal bearings and 2) numerical studies on behaviors of scratched journal bearings. Chapter 1 provides brief overviews on hydrodynamic journal bearings with its development history, damage types in hydrodynamic bearings, the current state of studies on the behaviors of scratched journal bearings, which is the main study aim of this thesis. Chapter 2 presents theoretical analysis with all necessary equations to determine a full thermohydrodynamic solution for multi-lobe journal bearings lubricated with an incompressible fluid. Chapter 3 presents numerical analysis, which include discretization of the equations using the finite volume method, meshing techniques, numerical procedure, and verifications for several cases. Chapter 4 validates the model by comparing the simulation results with experimental data. Chapter 5 presents numerical studies on behavior of a scratched journal bearing and the document ends with general conclusions and perspectives.

Chapter 1. Literature review

1.1. Overview of journal bearings

Journal bearings are important machine elements and one of the most common types of hydrodynamic bearings primarily used to support high speed rotating machinery, such as turbines, gas compressors, pumps, and motors. They can support very high applied load and have a very long lifetime. These are two most superior characteristics of journal bearings. A journal bearing comprises a journal (a part of the shaft which is housed by the bush) which rotates in a supporting bush with a thin lubricant film separating them. Under an applied load, the journal rotates with an eccentric position with respect to the bush which generates hydrodynamic pressures in the lubricant film to balance the applied load. Figure 1.1 presents one of the most basic type of journal bearings, a plain journal bearing. The inner surface of the bush usually lined with soft bearing materials such as soft tin and lead Babbitt. Lubricants used for journal bearings can be liquids (such as mineral or synthetic oils), gas, or grease, depending on the application.

Over the years, various types of bearing designs have been developed. They can be categorized into three main types: fixed pad non-preloaded, fixed pad preloaded journal bearings, and tilt pad bearings. In each category, there are many types of bearing designs which have been discussed widely in literature. Figure 1.3 presents one typical example for

each category of journal bearings. Each type of bearing has unique characteristics and is suitable for specific applications [1][2][3][4]. For example, fixed pad non-preloaded bearings although are subject to oil whirl, are easy to make with a low cost. Fixed pad preloaded journal bearings give good system stabilities for low to moderate speeds applications, but they are more difficult to manufacture accurately. Tilting pad bearings have high stiffness and high stability but are difficult to manufacture. They have a high cost and complex installation.

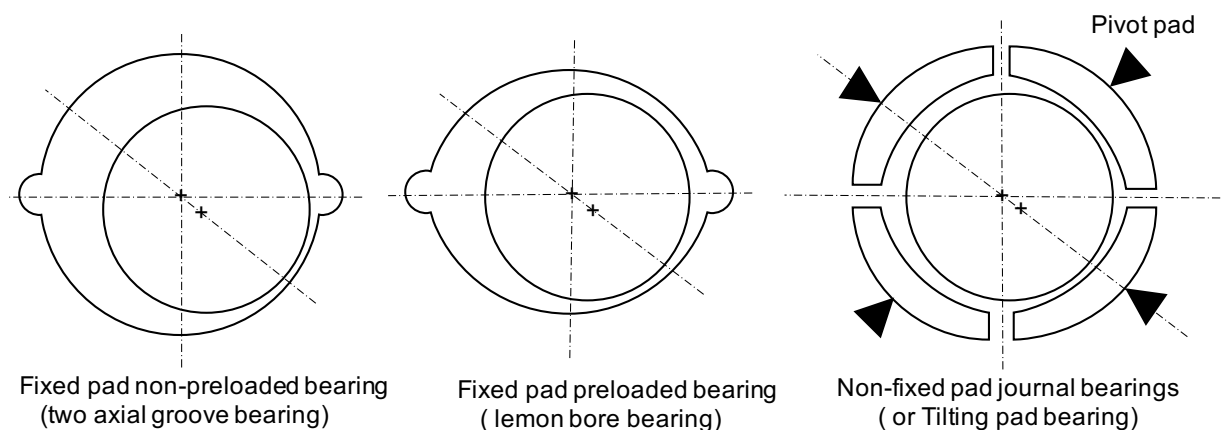


Figure 1.3. Three main categories of journal bearing (three typical examples).

The history of hydrodynamic journal bearing started before the nineteenth century but until in 1883, Tower [5] published the first of a series of reports presenting measured fluid pressures within a journal bearing. Dowson (1979) [6] in his book listed several main contributions from this report: the adequate lubrication is important; it is best to supply lubricant to the unloaded side of the bearing; with a fixed load, the lateral force acting on the journal increases with speed, friction initially decreases with increasing speed and, after exceeding a threshold, friction increases with speed; the journal and bush are separated by a film and if there is an adequate supply of lubricant; the local pressure within the load zone exceeds the mean pressure of the load. In Tower's second report [7], the pressure distribution in a journal bearing was further investigated. The experimental results showed pressure variations in

both axial and circumferential directions. Tower also showed that the integral of the pressures over the bearing circumference gives a load carrying capacity equal to the applied load.

Reynolds in 1886 [8] published the fluid film theory comprising the theory, differential equation, approximate solution, and journal bearing results described by Tower's experiments. The well-known terms such as wedge effect, Couette-type flow, Poiseuille-type flow are original from this study. He invented the classical Reynolds equation by simplifying the Navier-Stokes and the continuity of mass equations, with several assumptions. He also mentioned the possibility of oil-rupture in the cavitation zone, the possible influence of temperatures, and even wear in journal bearings.

Kingsbury (1897) [9] studied the load-carrying capacity of air-lubricated journal bearings by measuring the axial and circumferential pressure variations. Sommerfeld (1904) [10] extended the theoretical work of Reynolds to the limiting cases of the journal bearing, such as the short and the long bearings.

Another important phenomenon in journal bearings is cavitation, which was first studied by Gumbel (1914) [11]. In the author's model, the negative pressure was set to zero or ambient levels. Swift (1931) [12] and Stieber (1933) [13] later expanded the study with considering that the pressure gradient is nil at the rupture boundary. Later work by tribologists has developed various cavitation models to predict the performance of liquid-film bearings with acceptable accuracy for the various of applications; however, the physics behind the cavitation in bearings is still not satisfactory until 1957 when Dowson (1957) [14] published the first direct comparison of pressure measurements with photographs of the flow taken in the divergent zone. It is the first time that the phenomenon of cavitation has been identified just after a boundary of rupture. This invalidates the models of Swift and Stieber, which as-

sume zero pressure gradient in the circumferential direction for the rupture and film reformation boundaries. Moreover, it is shown that the film rupture occurs downstream from the point where the film thickness is minimal. The physical nature of cavitation in bearings with two basic forms, i.e. gaseous and vaporous, and the cavitation boundary applied in the Reynolds equation were presented by Dowson in [15] (1974) and [16] (1979). Braun and Hendricks [17] in the 1980s brought to the fore in the phenomenon of lubricant film rupture and reformation. During an experimental campaign, they took pictures in the divergent region of a transparent bearing. This showed that the film is ruptured, gas appearing in this region, and the sensors indicated pressures below atmospheric pressure. More recently, Cristea et al. [18] confirmed this observation in an experimental study of a circumferential grooved journal bearing. In 2011, Braun and Hannon [19] wrote an extensive experimental and numerical study about their findings around the phenomenon of lubricant film rupture and reformation.

This subsection presented a brief introduction and history of studies on journal bearings. In the next section, an overall of thermal effects in hydrodynamic journal bearings will be presented.

1.2. Overview of studies on thermal effects in hydrodynamic bearings

Thermal effects are very important in hydrodynamic lubrication and have been studied well before the nineteenth century. Hirn (1854) [20] presented experimental results obtained on a half journal bearing and contributed to two important findings: friction behaved according to the Coulomb's law in direct contact regime, and in the lubricated regime, the coefficient of friction increased proportionally to shaft speed. In addition, he proved that the coefficient of friction is proportional to the square root of the applied load, rotational speed, and area (for a moderately loaded journal bearing).

Reynolds (1886) [8] showed that there was an increase in the temperature of the lubricant and the lubricant viscosity was not constant but decreased with the rise of the temperature. He also provided an equation on the viscosity-temperature relationship of olive oil. In 1933, Kingsbury [21] published his study on heat effects in lubricant films with both theoretical and experimental parts for the fluid under axisymmetric conditions. He showed the shear stress in the lubricating fluid decrease following a rise in the temperature. He also proposed a thermal model in which viscosity variations across the film thickness were taken into account which was pioneering in thermohydrodynamic (THD) research. In 1948, Clayton and Wilkie [22] studied the temperature distribution in the bush of a journal bearing. They confirmed that the temperature field in the bearing is not uniform and that the maximum temperature of the bush was located in the minimum film thickness zone. In 1962, Dowson [23] modified the classical Reynolds equation in order to take into account lubricant viscosity variations and density variations both along and across the film. He proposed the well-known generalized Reynolds equation. When coupled with the energy equation, this describes properly the thermal phenomena in hydrodynamic lubrication. The equations form a system of non-linear partial differential equations, due to viscosity-temperature variations. Several approaches were applied to solve the system of equations. Some researchers simplified the energy equations by constant viscosity across the film [24], [25], [26]; Hansen and Lund [27][28], proposed a simplified analysis in order to reduce calculations by rewriting the energy equation with velocities deduced from isothermal theory and neglected axial temperature gradient. Boncompain and Frêne [29]-[30] presented a thermohydrodynamic solution for journal bearings, including recirculating flow. In 1983, Mitsui, Hori and Tanaka [31] carried out an experimental and theoretical study on the cooling of oil in the feeding groove. They introduced the mixing coefficient in their thermohydrodynamic model to determine the inlet

temperature distribution. In the same year, Ferron et al. [32] studied both theoretical and experimental thermohydrodynamic problem for a plain bearing in which they took into account the heat transfer between the film and both the shaft and the bush, oil recirculation, and also cavitation. They obtained satisfactory agreement between theoretical and experimental results. Ferron also showed that temperature rising in operating bearing can also lead to elastic deformations of solid parts and the deformations will change the film thickness, eccentricity, and lead to changes the pressure and temperature fields. Boncompain et al. in [29,30] also took elastic deformations into account in the model to define the film thickness. The results showed that taking elastic deformations into account allows a better approximation of the film thickness and therefore more precise results of pressures and temperatures. During the same period, Bou-Said [33] in 1985 proposed a generalized thermoelastohydrodynamic (TEHD) solution using the finite element method (FEM). In the early 1990s, Khonsari and Wang [34] presented a parametric study showing that the boundary conditions have a strong link with the thermoelastohydrodynamic characteristics. Monmousseau et al. [35,36] later in 1997-1998 carried out a TEHD study in transient state of tilting-pad journal bearings. The results emphasized the importance of considering elastic deformations during calculations in order to be able to predict the risks of seizure during the startup and shutdown phases.

M. Fillon and J. Bouyer in [37–40] focused also on thermal effects in journal bearings with presence of bearing damages due to the impact of misalignment, wear, and severe operating conditions. These phenomena modified the film thickness which changes the pressure and temperature distributions in the bearing. Recently, thermal effects on scratched bearings also was studied by Giraudeau et al. [41] and Bouyer et al. in [42].

In the following section, a more detailed presentation of damages in journal bearings will be given. Analysis of bearing damages is also a study objective in this thesis.

1.3. Damage in hydrodynamic bearings

Hydrodynamic bearings are great and important components in rotating machinery; however, when suffering failures, the consequences can be catastrophic and lead to the damage of the machine or the interruption of plant operation. To prevent or minimize the consequences, it is important to detect and identify the damage and establish its causes. Forms and types of bearing damage are various, this section presents some of the most common damage categories: damage due to the influence of particles, fatigue damage, and overheating damage.

1.3.1. Damage due to the influence of lubricant

When foreign particles find their way into the lubrication gap between the bearing and the journal, there is a great risk of bearing damage. Due to the very low thickness of the lubricating film, even small particles may disrupt operation and cause mixed friction.



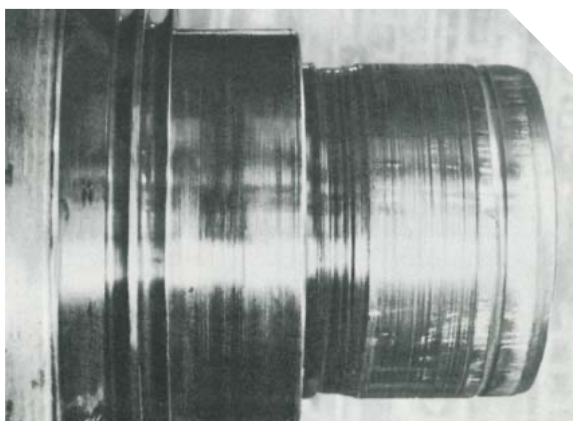
(a) White-metal lined bearing scored.



(b) Concentric scoring of a thrust pad.

Figure 1.4. Examples of scoring [43].

Scoring is a type of failure due to dirt in the lubricants which cause polishing and scoring of both bearing and mating surfaces. Two examples of scoring can be seen in Figure 1.4, one is the scoring in the white-metal lined surface of the bearing (Fig. 1.4a) and another is the scoring of thrust pad (Fig. 1.4b). The appearance of scoring are parallel grooves or scratches in the direction of sliding movement in the babbitt, journal, or bearing surfaces. The damage can range from light wear to severe scoring depending on many factors such as the dirt size and amount, the bearing material and its thickness, and operating conditions of the bearing. Sources of contamination of the lubricant can be built-in dirt on housings, shafts, oil galleries, etc., or come from outside during machine assembly or maintenance work; entrained dirt entering through air filters, metallic wear particles resulting from abrasive wear of moving parts [43–45] can also be considered. Scoring can degrade the performance of the bearings with a potential significant loss of load-carrying capacity and loss of lubricant viscosity due to hot operating temperature [46].



(a) Wire wooling on a shaft.



(b) Wire wooling on a thrust pad.

Figure 1.5. Examples of wire wooling on the journal and a thrust pad [43].

Wire wooling is a type of abrasive wear which occurs when relatively large particles embed in the Babbitt and causes severe damage to the Babbitt surface and journal. It may form a hard scab of material by contact with the journal and cause severe damage to the mating surface by acting like a cutting tool. This machining propagates until the bearings are inoperable. Two examples of scoring can be seen in Figure 1.5, one is the scoring on a shaft (Fig. 1.5a) and the other is on a thrust pad (Fig. 1.5b).

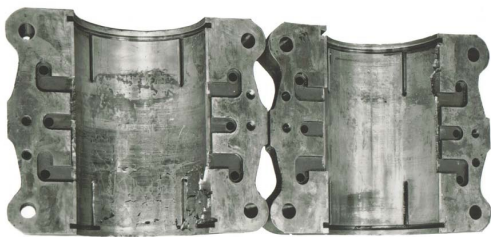
Erosion is a form of loss of material caused by the flow forces of oil. This effect is worsened by small particles broken out from the material in the cavitation regions, or from different areas of the engine, entering the lubricant system. Erosion depends on operating conditions such as high speed and low clearance, high temperature. The impact of erosion can be reduced by keeping a sufficient cooling, replacing the oil filter and oil according to the manufacturer's specifications.

In the cavitation regions, when the static pressure rises to a point where vapor bubbles collapse implosively, strong pressure surges are produced, usually at high temperatures. The large implosive forces cause the material to break off and cause material erosion. In dynamically loaded bearings the cavitation damage possibly depends on operating eccentricity, and extends around the bearing surface, since the pressure wave rotates with the journal. High temperatures may also advance cavitation. Cavitation in journal bearings can be controlled and minimized by proper location of the feeding [47], or by adjusting bearing clearance and increasing the supply pressure to the bearing.

1.3.2. Fatigue damage and wear due to mixed friction

Fatigue damage is a progressive decrease of material cohesion. The principle of fatigue failure of Babbitt metal is similar to any other metal fatigue. When the material cohesion is

exceeded locally, fatigue occurs [48]. The first crack is formed and continues to grow due to notch effect and develops a network of cracks in a mosaic pattern, and also nicks can occur in the bearing metal. Two examples can be seen in Figure 1.6, one is the fatigue damage on a bush (Fig. 1.6a) and the other is on a tilting pad (Fig. 1.6b). Fatigue cracking of Babbitt material can be due to inadequate lubrication, deflection and misalignment of shafts [49]. It can also be due to high temperatures, which accelerates material fatigue since they reduce the strength of the bearing material. There are several recommendations to remedy the fatigue damage such as using a stronger material and a thin Babbitt, checking stress of the bearings, the misalignment, or ensuring a sufficient cooling.



(a) Babbitt mechanical fatigue on a bush.



(b) Babbitt mechanical fatigue on a tilting pad.

Figure 1.6. Examples of mechanical fatigue [50].

Wear is a loss of material from the surface of a solid body, due to mechanical action. In hydrodynamic bearings, wear is caused by metallic contact due to mixed friction between the bearing and the shaft journal, which usually occur each time at the start-ups and shut-downs. When the journal starts rotating from the rest position, the bearing passes through the mixed friction range due to insufficient lubrication, and directed contact occurs between the journal and the Babbitt and wear occurs. This type of wear is due to mixed friction and can be reduced by using wear-resistant materials. In journal bearings, minimum film thickness and film damping will decrease with wear, which may affect the overall machine dynamics [46].

1.3.3. Failures due to overheating

Overheating in bearings can occur in a variety of ways and it can cause discoloration, cracks, deformation, and melting of the bearing materials. A network of cracks due to thermal fatigue and discoloration and fusion are usually visible. Overheating can come from various sources such as inadequate running clearance, inadequate oil supply, overload, excess speed, rubbing, and cooling problems.

When a bearing operates under high temperatures and high local pressure which exceeds the local yield strength of the Babbitt, it often causes deformation of the Babbitt metal in the direction of shaft rotation. It is another form of bearing damage, known as creep (Fig.1.7).

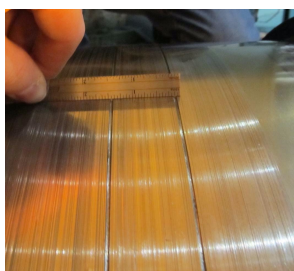


Figure 1.7. An example of babbitt material creep in a cylindrical bearing [46].

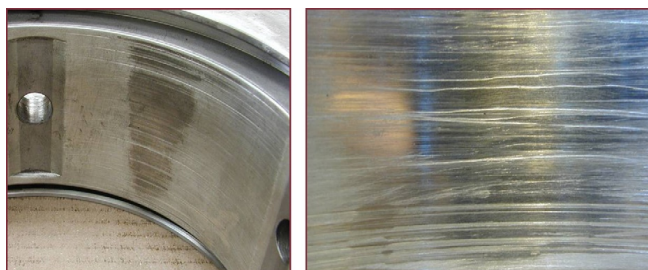
This sub section presented several types of damages in hydrodynamic bearings, possible causes and impacts as well as several ways to remedy them. It is noted that they are not all the damages that can be observed in hydrodynamic bearings, more can be found in [43,50,51].

1.4. Overview of studies on scratched journal bearings

There are various types of damage presented in the previous section. This thesis focuses on one of the most common damage which is scratches. The scratch is a major type of surface damage in Babbitted industrial bearings. Scratches on journal bearings are a common issue observed during maintenance operations by users of steam turbines, pumps, motors, etc. They are often caused by the presence of debris within the lubricating oil that are trapped in the Babbitt. A scratch has a narrow cross-section but a significant length; scratches can be shallow or deep [46]. Scratches can appear on the Babbitted surface as well as on the rotating surface. Some examples of bearing scratch can be seen in Figure 1.8a for the scratches on the journal and in Figure 1.8b for the scratches on the bearing pads.



(a) Heavily scored bearing journal on large turbine [46].



(b) Scratched bearing pads [52].

Figure 1.8. Examples scratches on hydrodynamic journal bearings.

Scratches degrade the performance of journal bearings, but their effects were neglected for a long time. One of the earliest studies on this subject was in 2012, when Dobrica and Fillon [52] conducted a numerical study on performance degradation in scratched journal bearings. They performed a parametric study, using a hydrodynamic numerical model with global thermal effects, to simulate scratched journal bearings. They evaluated several scratch parameters (depth, extent, density, etc.) and concluded that the bearing performance is

poorer in the presence of a scratch. They also highlighted that the scratch depth appears to be the most influential parameter affecting the bearing performance, especially if the depth is greater than the bearing clearance. In 2016, Giraudeau et al. [53] carried out experimental measurements of local parameters such as pressure and temperature, and global parameters such as friction torque and flow rate, for a two-lobe journal bearing with one scratch. They showed that the scratch depth influences pressure and temperature, but also that the effects depend on the operating conditions (imposed load and speed). In 2018, Bouyer et al. [42] compared thermoelastohydrodynamic (TEHD) simulation results with the experimental results of Giraudeau et al.'s study. This TEHD model made a simplification for the scratch geometry by adding the scratch depth value to the lubricant film thickness instead of meshing the real geometry of the lubricant film domain. In 2020, Bouyer et al. [17] updated their work and carried out experiments for multiple scratches on a journal bearing (two and sixteen scratches); they concluded that scratches induce a strong modification of the pressure field, increase both the maximum pressure and the maximum temperature, and significantly reduce the load-carrying capacity of the bearing. In the same year, Chatterton et al. [54] published a study on the effect of artificial scratches on pads on the static and dynamic behaviors of a tilting pad journal bearing, in which they studied the effects of scratch depth and position on the performance of the scratched bearing and the dynamic coefficients have been estimated as well. Their results confirmed a degradation of the dynamic performance of the scratched bearing by means of both simulations and experiments. In 2021, Bouyer et al. [55] investigated the influence of a multi-scratched shaft on hydrodynamic journal bearing performance and observed a significant drop in the load-carrying capacity of the bearing. The maximum pressure in the bearing mid-plane increases by more than 50% and the maximum temperature by more than 15 K in the most detrimental case.

Experimental measurements to assess scratched journal bearings are available although they are case by case studies. The experimental data show several potential problems related to the presence of the scratches on the bearings, for example, a loss in load carrying capacity and a rise in operating temperature and other relevant problems. These data also provide bearing users with a better understanding of the problems and the performance of the scratched bearings. However, to have logical insights into the problems, many unique experiments might be needed it will be highly costly and time consumed. Then, simulation modeling could be the best solution to deal with this problem. Simulation modeling can solve real-world problems safely and efficiently. Simulation enables experimentation on a valid digital representation of a system based on algorithms and equations with the aid of powerful computers. The uses of simulation are varied. For example, it is used to study design parameters or new hypotheses efficiently or used to simulate experiments that are impractical to conduct because of cost or time.

Unfortunately, to our knowledge, there are only a few valid numerical models that are able to simulate scratched journal bearings and they are still have limitations. Considering some of the main available numerical models in this research topic, for example, the model of Dobrica et al. in [52], this is an isothermal modeling in which they considered the global thermal effect with a global temperature of the fluid or not solving the energy equation to calculate the temperature of the fluid film. Therefore, the obtained results might be underestimated. Another model is the model of Giraudeau et al. in [41], this is a thermohydrodynamic model applied for a journal bearing with a single artificial scratch. In this model, the real geometry of the scratch was not modeled, instead the lubricant film thickness in the in the scratch zone was simplified by adding the scratch depth to the film thickness for the same

studied case with an assumption of no scratch. It may not produce any problems in the Reynolds equation, but for the energy equation it could introduce some differences in calculated temperatures because of different temperature boundary conditions in the scratch region. The model has no temperature boundary conditions at the interface between the fluid and the journal in the axial walls in the scratch region, it is not the same situation with the real scratch geometry considered. Therefore, the obtained results might be underestimated, especially when the bearing has more scratches.

Therefore, this study focuses on developing a full thermohydrodynamic numerical model which is able to simulate performance of journal bearings under the presence of the scratches. In this model, the real geometry of the scratch will be modeled; thermal effects will be taken into account; and the model will be able to simulate for journal bearings with multiple scratches.

1.5. Conclusions

This section presented brief overviews on hydrodynamic journal bearings with the development history, studies in the thermal effects, several damage types in hydrodynamic bearings, and the current state of studies on the behaviors of scratched journal bearings. The next sections will describe further the improvements made by the work of the thesis.

Chapter 2. Theoretical analysis

2.1. Geometrical characteristics of a lobe bearing

This chapter describes the geometry of a typical lobe bearing with a geometrical pre-load factor, geometrical calculations, generalized Reynolds equation for the hydrodynamic pressure in fluid films, the energy equation for the temperature of the fluid film, the Laplace heat-conduction for the temperature in solid parts, and boundary conditions. All these the information allow to determine a full a thermohydrodynamic solution for journal bearings.

2.1.1. Geometrical characteristics

The journal bearing includes a part of a shaft (journal) rotating inside a bushing or a bearing (comprises one or multiple lobes). Fig 2.1 describes as an example the geometrical characteristics of a three-lobe journal bearing; it can be expanded for any other multi-lobe journal bearing in the same manner, the number of lobes being comprised between one and N_l .

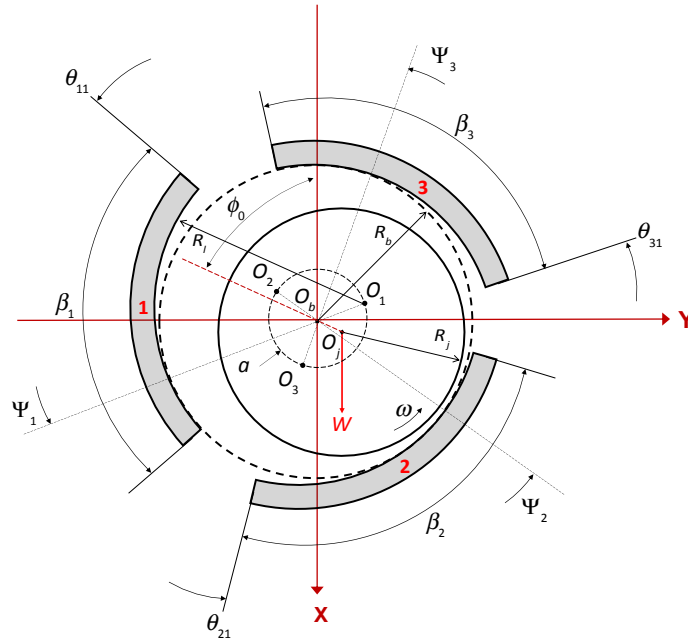


Figure 2.1. Geometrical characteristics of a three-lobe journal bearing.

The symbolic notations and the definitions for the bearing are:

- Number of lobes is N_l ; the lobe index is i^{th} .
- The center of the bearing is O_b , the center of the journal is O_j , and the center of the i^{th} lobe is O_i .
- The global coordinate system is (O_b, X, Y, Z) .
- The position of the i^{th} lobe is defined by its beginning angular position θ_{i1} and the angle Ψ_i between the center line $O_b O_i$ and $O_b X$.
- The radius of the i^{th} lobe is R_l , and its angular length is β_i .
- The radius of the journal is R_j .
- The radius of the bearing is $R_b = R_l - a$, where a is the radius of the preload circle, i.e., the circle that centers at O_b , and consists of the centers of the lobes.
- Manufacturing clearance is $C_l = R_l - R_j$

- Assembly clearance is $C_b = R_b - R_j$
- Geometrical preload is $m = (C_i - C_b) / C_i$; a preloaded bearing means that the center of curvature of the lobe is not coincident with the center of the bearing. It can be thought of as the percentage of clearance reduction. If $m=0$ or there is no preload, the bearing clearance is unchanged for a bearing with a centered shaft, but $m=50\%$ reduces the clearance by a half at the minimum clearance position.

2.1.2. Lubricant film thickness

Fig. 2.2 shows the geometry of a multi-lobe bearing; however, only one lobe is drawn in this figure for a simple visualization. All the notations and definitions are the same as described in the previous section. Here we have a local coordinate system for the current lobe (O, R_j, θ^*, y, z) and the lobe coordinate system for the lobe examined (O_i, t, r, z) is introduced in this figure. The angular position of the journal in this lobe coordinate system is denoted as θ , while it is θ^* in the local coordinate system.

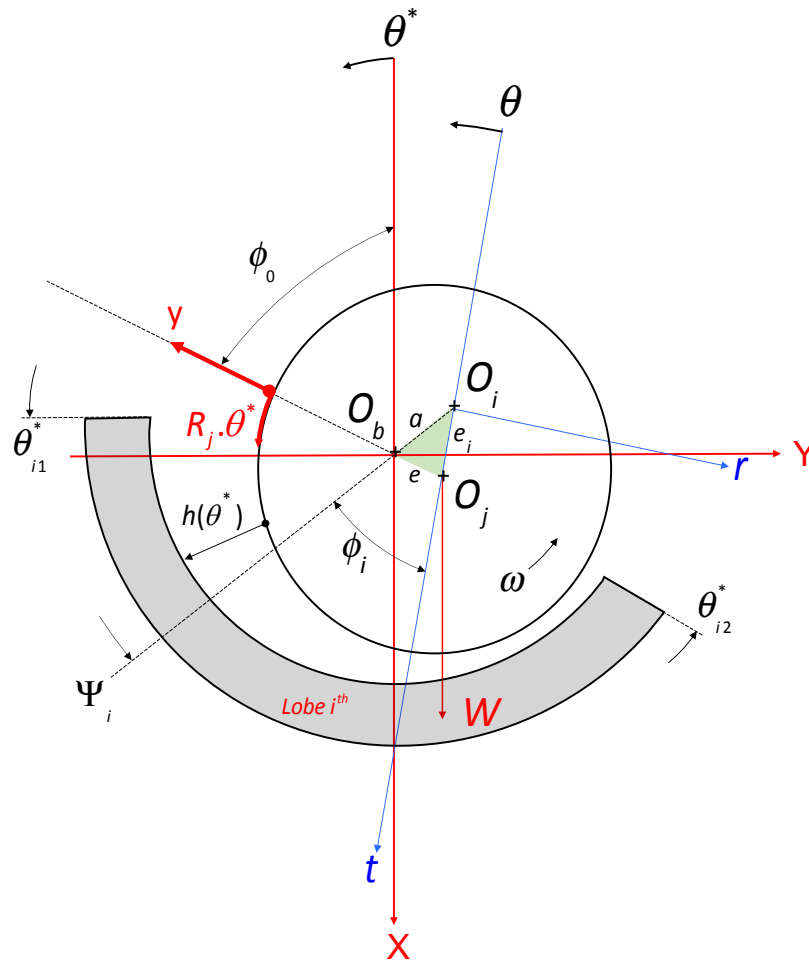


Figure 2.2. Geometry of a lobe bearing, in section $z = 0$.

At starting position, the shaft rests at bottom dead center of the bushing. When the bearing is operating, the journal, under load, shifts its location to an eccentric position on a layer of fluid film. At the centered position, the distance between the journal center and the bearing center is the bearing eccentricity e , and the distance between the journal center and the center of the i^{th} lobe is e_i . The fluid film thickness is a crucial parameter for the bearing, it is used to determine the hydrodynamic pressure developed in the fluid film. The film is unwrapped on the Cartesian coordinate system as shown in Figure 2.3 for the case of a two-lobe bearing.

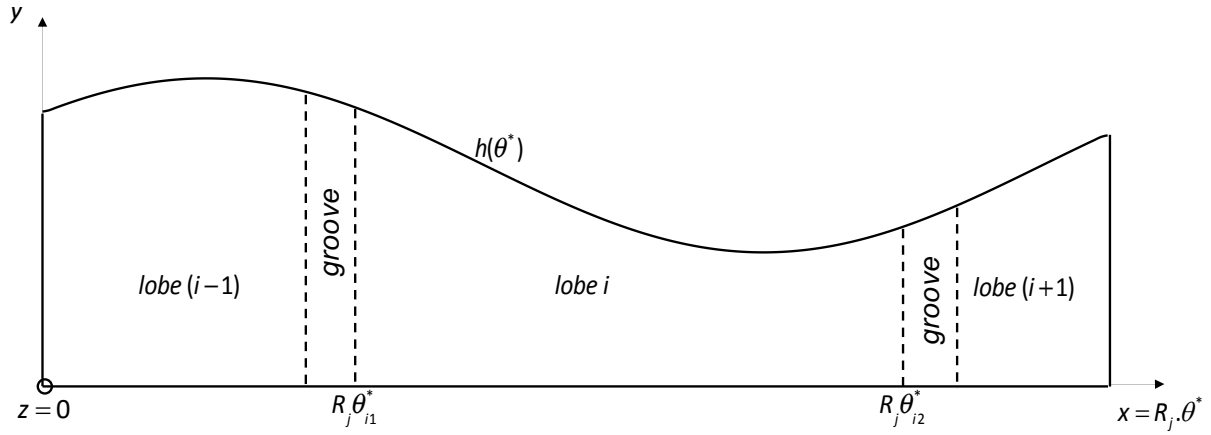


Figure 2.3. Lubricant film unwrapped for a two-lobe journal bearing without geometrical preload.

The limits of the film domain of lobe (i) can be determined as follows:

$$\begin{cases} \theta_{i1}^* \leq \theta^* \leq \theta_{i2}^* \\ 0 \leq y \leq h(\theta^*, z) \\ 0 \leq z \leq L \end{cases}$$

The lubricant film thickness h is expressed as a function of the position angle θ^* of the shaft.

Considering the lobe i in Fig. 2.3, the fluid film starts at $R_j \theta_{i1}^*$ and ends at $R_j \theta_{i2}^*$ in the circumferential direction. In the triangle $O_b O_j O_i$, we have the relationship:

$$e_i = \sqrt{e^2 + a^2 + 2ae \cos(\psi_i - \phi_i)} \quad (2.1)$$

In addition, we have the relation between the bearing coordinate system and lobe coordinate system as:

$$\theta = \theta^* + \pi - \phi_i - \psi_i \quad (2.2)$$

From Eq. (2.1), Eq. (2.2), the film thickness corresponding to the bearing coordinate system can be determined as:

$$h(\theta^*) = C + e_i \cos(\theta^* - \phi_i - \psi_i) \quad (2.3)$$

Eq. (2.3) allows to calculate the film thickness of each lobe of a multi-lobe bearing separately. Note that this equation does not consider the eventual defects of the bearing yet. If any defects exist, scratches for example in this study, they will be added to the film thickness with their location and geometry, which are known.

If the bearing has no preload ($a=0$), then the local lobe coordinate system overlaps the global bearing coordinate system. Here, the lobe bearing becomes a plain bearing and then the thin film thickness is given by:

$$h(\theta) = C + e \cos \theta \quad (2.4)$$

2.2. Equations of Hydrodynamic lubrication

2.2.1. Hypothesis

The generalized Reynolds equations for thin films are deduced from the Navier-Stokes equations (Eq. 2.5), and the mass conservation equation (Eq. 2.6), applied to a Newtonian fluid. They are the equations that govern the problems of hydrodynamic bearings.

$$\rho \left(\frac{\partial u_i}{\partial t} + u_i \frac{\partial u_i}{\partial x_i} \right) = - \frac{\partial p}{\partial x_i} + \lambda \frac{\partial^2 u_j}{\partial x_i \partial x_j} + \mu \left(\frac{\partial^2 u_i}{\partial x_j^2} + \frac{\partial^2 u_j}{\partial x_i \partial x_j} \right) + \frac{\partial u_j}{\partial x_j} \frac{\partial \lambda}{\partial x_i} + \left(\frac{\partial u_i}{\partial x_j} + \frac{\partial u_j}{\partial x_i} \right) \frac{\partial \mu}{\partial x_j} \quad (2.5)$$

$$\frac{\partial p}{\partial t} + \frac{\partial (\rho u_i)}{\partial x_i} = 0 \quad (2.6)$$

The developments require eight assumptions given below:

- All inertia forces are minor compared to the viscous shear of the fluid and, therefore,

are negligible: $\frac{\partial u_i}{\partial t} = 0$.

- The thickness of the fluid film in the y-direction is small when compared to the circumferential x-and axial length z-directions, the ratio between bearing clearance and the journal radius: $C / R \cong 10^{-3}$. This assumption allows on one hand to neglect the effects of curvature and on the other hand to consider that the journal and inner bushing have the same circumferential lengths. Therefore, as explained in section 2.1, the lubricant film can be unwrapped on a Cartesian coordinate system.
- The lubricant fluid is continuous, no gas and bubbles or film ruptured.
- The pressure variation in the y-direction is negligible.
- The lubricant fluid is Newtonian, meaning its shearing stresses vary linearly with the rate of shearing strain.
- The flow is laminar; there is no vortex flow or turbulence in the lubricant film.
- There are no body forces (gravity, centrifugal, or other external forces, etc.), acting on the fluid film.
- There is no slipping between the lubricant film and the solid boundary

2.2.2. Equation of generalized viscous thin films

Figure 2.4 describes a lubricant film domain delimited by two bounding walls 1 and 2. The coordinate system is chosen as such Y is the direction across the lubricant film. Every point M within the domain has coordinates $M(x,y,z)$ and its velocity components in X, Y, Z directions are u,v,w , respectively. On the bounding walls 1 and 2, we have points M_1 with Y coordinate H_1 , velocity components U_1,V_1,W_1 and density ρ_1 ; M_2 with Y coordinate H_2 and velocity components U_2,V_2,W_2 and density ρ_2 , respectively.

The viscosity of the lubricant μ , the density of the lubricant ρ , the pressure p , the velocity components, the temperature T at any point M within the domain are functions of its position and time, denoted as: $\mu(x,y,z,t)$, $\rho(x,y,z,t)$, $p(x,y,z,t)$, $u(x,y,z,t)$, $v(x,y,z,t)$, $w(x,y,z,t)$, $T(x,y,z,t)$, respectively.

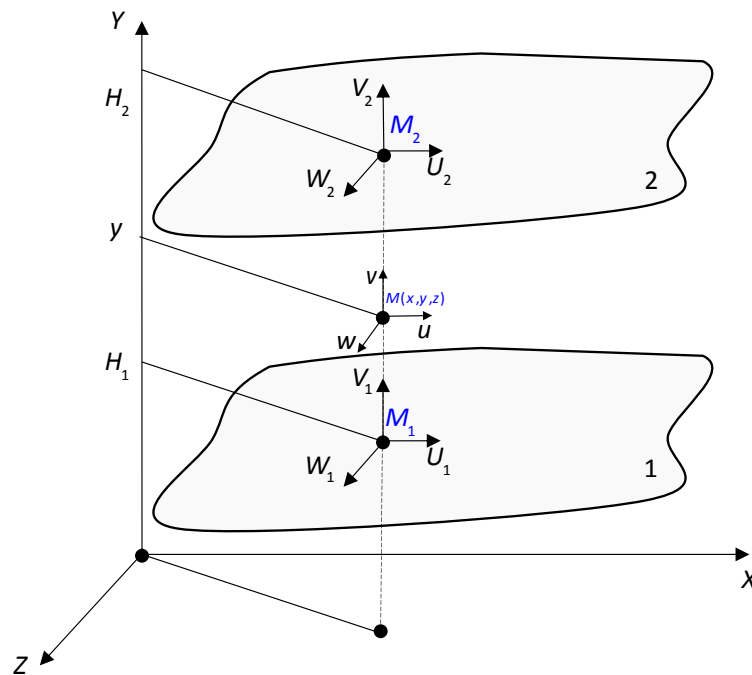


Figure 2.4. Axis system and notations.

Based on the above eight assumptions, the Navier equations are reduced to the following form:

$$\left\{ \begin{array}{l} \frac{\partial p}{\partial x} = \frac{\partial}{\partial y} \left(\mu \frac{\partial u}{\partial y} \right) \\ \frac{\partial p}{\partial y} = 0 \\ \frac{\partial p}{\partial z} = \frac{\partial}{\partial y} \left(\mu \frac{\partial w}{\partial y} \right) \end{array} \right. \quad (2.7)$$

In the following, it will be assumed that:

$$I_n(x, y, z, t) = \int_{H_1}^y \frac{y^n}{\mu(x, y, z, t)} dy \quad (2.8)$$

$$J_n(x, z, t) = \int_{H_1}^{H_2} \frac{y^n}{\mu(x, y, z, t)} dy \quad (2.9)$$

Then, the velocity components can be expressed as:

$$\begin{cases} u(x, y, z, t) = \frac{\partial p}{\partial x} \left(I_1 - \frac{I_0 J_1}{J_0} \right) + \frac{U_2 - U_1}{J_0} I_0 + U_1 \\ w(x, y, z, t) = \frac{\partial p}{\partial z} \left(I_1 - \frac{I_0 J_1}{J_0} \right) + \frac{W_2 - W_1}{J_0} I_0 + W_1 \end{cases} \quad (2.10)$$

The equation of mass conservation within the fluid is written as:

$$\frac{\partial \rho}{\partial t} + \frac{\partial(\rho u)}{\partial x} + \frac{\partial(\rho v)}{\partial y} + \frac{\partial(\rho w)}{\partial z} \quad (2.11)$$

$$\begin{aligned} \frac{\partial}{\partial x} \left(G \frac{\partial p}{\partial x} \right) + \frac{\partial}{\partial z} \left(G \frac{\partial p}{\partial z} \right) &= \frac{\partial}{\partial x} [U_2(R_2 - F) + U_1 F] - \rho_2 U_2 \frac{\partial H_2}{\partial x} + \rho_1 U_1 \frac{\partial H_1}{\partial x} \\ &+ \frac{\partial}{\partial z} [W_2(R_2 - F) + W_1 F] - \rho_2 W_2 \frac{\partial H_2}{\partial z} + \rho_1 W_1 \frac{\partial H_1}{\partial z} \\ &+ \frac{\partial R_2}{\partial t} - \rho_2 \frac{\partial H_2}{\partial t} + \rho_1 \frac{\partial H_1}{\partial t} + \rho_2 V_2 - \rho_1 V_1 \end{aligned} \quad (2.12)$$

The functions R, F and G are defined by:

$$R(x, y, z, t) = \int_{H_1}^y \rho(x, y, z, t) dy \quad (2.13)$$

$$F(x, z, t) = \frac{1}{J_0(x, z, t)} \int_{H_1}^{H_2} \frac{R(x, y, z, t)}{\mu(x, y, z, t)} dy \quad (2.14)$$

$$G(x, z, t) = \int_{H_1}^{H_2} \frac{R(x, y, z, t)}{\mu(x, y, z, t)} dy - J_1(x, z, t) F(x, z, t) \quad (2.15)$$

Eq. (2.12) is the generalized equation for thin viscous films. Solving this equation results in the hydrodynamic solution for pressure in the thin viscous films.

2.2.3. Equation of generalized viscous thin films for journal bearings

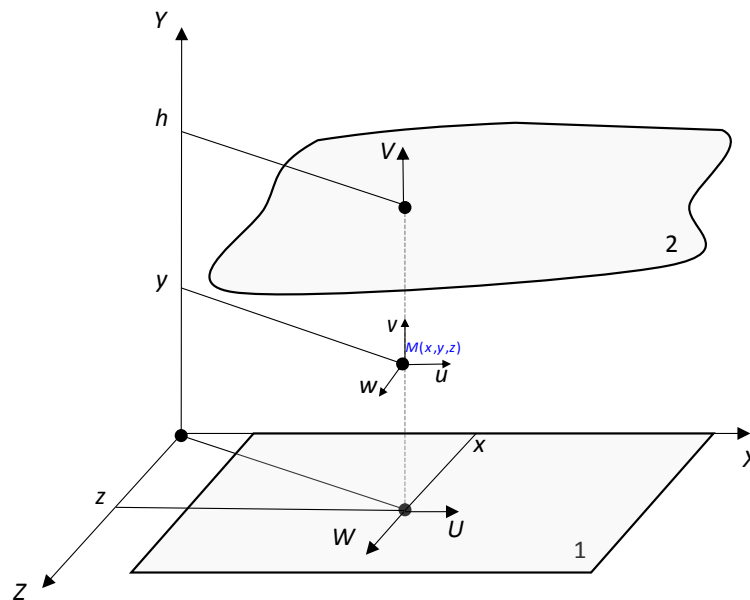


Figure 2.5. Axis system and notations for a developed journal bearing.

When applied to journal bearings, Eq. (2.12) can be simplified thanks to boundary conditions. The curvature of the walls is negligible and thus the walls can be considered as flat surfaces. The wall 1 is chosen as the reference wall for the film thickness. The velocity component in Y-direction on this wall is therefore nil, the U_2 and W_2 are simplified respectively as U and W . At the wall 2, the components U and W are nil because this plane is considered not moving, component V_2 is simplified as V . With these new considerations, Fig. 2.5 schematically represents the axis system and notations for a developed journal bearing. Taking these new references into account, Eq. (2.12) is simplified as presented in Eq. (2.16):

$$\frac{\partial}{\partial x} \left(G \frac{\partial p}{\partial x} \right) + \frac{\partial}{\partial z} \left(G \frac{\partial p}{\partial z} \right) = \frac{\partial(UF)}{\partial x} + \frac{\partial(WF)}{\partial z} + \rho V + \frac{\partial R}{\partial t} - \rho \frac{\partial h}{\partial t} \quad (2.16)$$

When the fluid is assumed to be incompressible, functions R, F and G become:

$$\begin{aligned}
 R(x, y, z, t) &= \rho y & (a) \\
 F(x, z, t) &= \rho \frac{J_1(x, z, t)}{J_0(x, z, t)} & (b) \\
 G(x, z, t) &= \rho \left[\int_0^h \frac{y^2}{\mu(x, y, z, t)} dy - \frac{J_1^2(x, z, t)}{J_0(x, z, t)} \right] & (c)
 \end{aligned}
 \tag{2.17}$$

Assuming that the journal does not have any axial movement, the velocity component W for velocity is nil. By replace the squeeze velocity V component with the derivative of the film thickness over time. By taking into account these assumptions with Eq. (2.16), Eq. (2.17) become:

$$\frac{\partial}{\partial x} \left(G \frac{\partial p}{\partial x} \right) + \frac{\partial}{\partial z} \left(G \frac{\partial p}{\partial z} \right) = \frac{U}{2} \frac{\partial(\rho h)}{\partial x} + \frac{\partial(\rho h)}{\partial t}
 \tag{2.18}$$

Eq. (2.18) is the generalized Reynolds equation for hydrodynamic journal bearings with an uncompressible fluid. Solving this equation results in obtaining the expression of the pressure in the lubricating film. This equation, however, does not consider the lubricant film rupture in the cavitation regions.

2.2.3. The Reynolds equation considering film rupture

The generalized Reynolds equation described in section 2.2.2 can only be applied to find hydrodynamic solutions for a full lubricant film without cavitation, i.e. the film is not ruptured. Experimental observations earlier show that the lubricant fluid does not occupy all the space between the bounding walls in journal bearings. In reality, there are several zones of the film domain which are filled with gas, which might come from the outside of the bearing. Fig. 2.6 presents a film domain with two sub-domains: active and inactive zone. The active zones are defined as the zones which are filled completely by the lubricant; in contrast, the

inactive zones are where the film rupture occurs. The rupture zones are developed from the active zones when the pressure p within the fluid becomes less than the saturating vapor pressure p_{ref} of the fluid. As a result, the fluid cannot withstand the tensions and loses its cohesiveness. It is known as cavitation. In a summary, when the pressure p is equal or larger than the reference pressure p_{ref} , the film is full filled; otherwise, the film is ruptured or there are cavitation zones in that domain of the film.

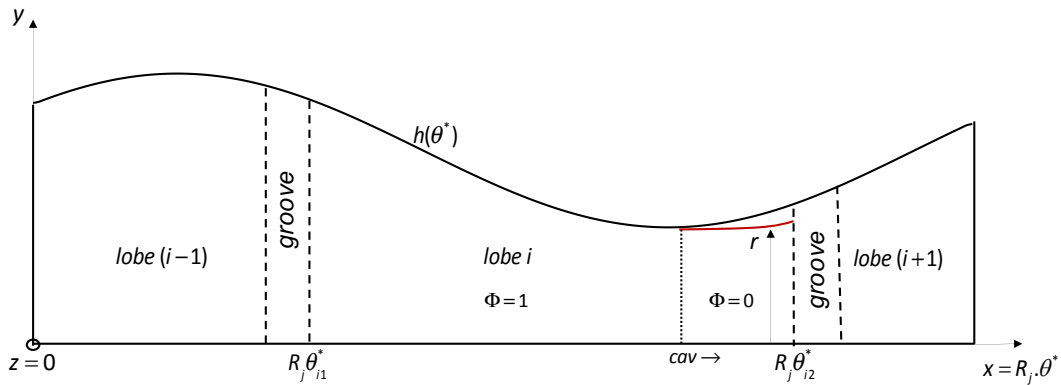


Figure 2.6. Cavitation representation in the film.

In the cavitation zones, we assume that the fluid filling the space between the bounding walls is a homogeneous mixture of lubricant and gas and has a density ρ_m . Introduced r is the filling which presents the thickness of fluid film available in the inactive zones.

In the active zones, the value of r equals thin film thickness h and in the inactive zones its value is less than h . Because of considering the cavitation phenomenon, the generalized Reynolds equation should be changed as below:

$$\Phi \left[\frac{\partial}{\partial x} \left(G \frac{\partial p}{\partial x} \right) + \frac{\partial}{\partial z} \left(G \frac{\partial p}{\partial z} \right) \right] = \frac{U}{2} \frac{\partial(\rho h)}{\partial x} + \frac{\partial(\rho h)}{\partial t} + (1 - \Phi) \left[\frac{U}{2} \frac{\partial(\rho D)}{\partial x} + \frac{\partial(\rho D)}{\partial t} \right] \quad (2.19)$$

In this equation, the index function Φ and universal function D were introduced as:

$$\begin{cases} D = p - p_{ref} \geq 0 & \text{then } \Phi = 1 \text{ or the film is full} \\ D = r - h < 0 & \text{then } \Phi = 0 \text{ or the film is ruptured} \end{cases}$$

When the pressure p is higher than p_{ref} then Φ is equal to 1; therefore, the last term in Eq. (2.19) becomes 0 and results in the generalized Reynolds equation. In contrast, when the filling r is less than h or $\Phi = 0$, the last term in this equation is not equal to 0, but all terms in the left side of the equation disappear. It turns Eq. (2.19) into the mass conservation equation. As the result, equation Eq. (2.19) allows to calculate the pressure distribution in the full film zones and the mass conservation in the ruptured zones. In conclusion, hydrodynamic solutions for the whole film domain were obtained by solving Eq. (2.19).

2.3. Equations in thermohydrodynamic (THD) regime

2.3.1. Generalized Reynolds equation

In the previous section, the hydrodynamic Reynolds solution is developed to determine the hydrodynamic pressure within the lubricant film. This section describes the thermohydrodynamic Reynolds solution, where the energy equation of the fluid is coupled to the Reynolds equation through velocity, density, and dynamic viscosity. The connections of the temperature of the fluid and the surrounding solids are also taken into account. Consequently, the generalized Reynolds equation can be rewritten as follows:

$$\Phi \left[\frac{\partial}{\partial x} \left(G \frac{\partial p}{\partial x} \right) + \frac{\partial}{\partial z} \left(G \frac{\partial p}{\partial z} \right) \right] = \rho \left[U \frac{\partial (J_1 / J_0)}{\partial x} + (1 - \Phi) \frac{U}{2} \frac{\partial D}{\partial x} \right] \quad (2.20)$$

, where:

$$J_n = \int_0^h \frac{y^n}{\mu(x, y, z)} dy \quad (2.21)$$

$$G(x, z) = \rho \left[\int_0^h \frac{y^2}{\mu(x, y, z)} dy - \frac{J_1^2(x, z)}{J_0(x, z)} \right] \quad (2.22)$$

; and p is the fluid pressure, U is the rotational speed of the journal, ρ is the fluid viscosity, and h is the fluid film thickness.

2.3.2. Velocity

From Navier-Stokes equation and mass conservation equation, velocity components u , v , w can be derived:

$$u(x, y, z) = \frac{\partial p}{\partial x} \left(I_1 - I_0 \frac{J_1}{J_0} \right) + U \left(1 - \frac{I_0}{J_0} \right) \quad (2.23)$$

$$w(x, y, z) = \frac{\partial p}{\partial z} \left(I_1 - J_1 \frac{I_0}{J_0} \right) \quad (2.24)$$

, where:

$$I_n = \int_0^y \frac{y^n}{\mu(x, y, z)} dy \quad (2.25)$$

Velocity component v along the thickness of the film then is obtained from the mass conservation equation for an incompressible fluid, Eq. (2.26):

$$\frac{\partial u}{\partial x} + \frac{\partial v}{\partial y} + \frac{\partial w}{\partial z} = 0 \quad (2.26)$$

which leads to:

$$v(x, y, z) = - \int_0^y \left(\frac{\partial u(x, y, z)}{\partial x} + \frac{\partial w(x, y, z)}{\partial z} \right) dy \quad (2.27)$$

2.3.4. Energy equation

Energy equation is derived from the first thermodynamic principle. For simplifications, external forces, gravity effects, expansion energy, and velocity change in y-direction are neglected. In addition, thermal coefficient C_v and conduction coefficient K_f are constant throughout thin film, then energy equation can be calculated as:

$$\rho C_p \left(u \frac{\partial T}{\partial x} + v \frac{\partial T}{\partial y} + w \frac{\partial T}{\partial z} \right) = K_f \frac{\partial^2 T}{\partial y^2} + \mu \left[\left(\frac{\partial u}{\partial y} \right)^2 + \left(\frac{\partial w}{\partial y} \right)^2 \right] \quad (2.28)$$

This equation is applied on the film in the full film zones. In rupture zones the fluid characteristics such as the density, the conduction coefficient, the specific heat coefficient, and the viscosity must be changed properly. For this purpose, equivalent coefficients μ_{equi} , ρ_{equi} , K_{equi} , $C_{p\ equi}$ are introduced for these characteristics, in relation with the ratio between the filling and the thin film thickness:

$$\mu_{equi} = \frac{r}{h} \mu_f + \left(1 - \frac{r}{h} \right) \mu_g \quad (2.29)$$

$$\rho_{equi} = \frac{r}{h} \rho_f + \left(1 - \frac{r}{h} \right) \rho_g \quad (2.30)$$

$$K_{equi} = \frac{r}{h} K_f + \left(1 - \frac{r}{h} \right) K_g \quad (2.31)$$

$$C_{p\ equi} = \frac{r}{h} C_{p\ f} + \left(1 - \frac{r}{h} \right) C_{p\ g} \quad (2.32)$$

where the subscript “f” denotes the characteristics in the full film zones, while the subscript “g” denotes the characteristics in the ruptured film zones. The energy equation is rewritten as follows:

$$\rho_{equi} C_{p_{equi}} \left(u \frac{\partial T}{\partial x} + v \frac{\partial T}{\partial y} + w \frac{\partial T}{\partial z} \right) = K_{equi} \frac{\partial^2 T}{\partial y^2} + \mu_{equi} \left[\left(\frac{\partial u}{\partial y} \right)^2 + \left(\frac{\partial w}{\partial y} \right)^2 \right] \quad (2.33)$$

The viscosity of the fluid is not constant but changes as a function of temperature. This is taken into account by using the equation proposed by McCoull and Walther:

$$\log_{10} \log_{10}(v + a) = -m \log_{10} T + n \quad (2.34)$$

, where v is kinematic viscosity; a , m , and n are constants depended on the temperature of the fluid.

2.3.5. Heat conduction equation

Heat transfer in the bushing is governed by a Laplace type equation, which takes the following form:

$$\frac{\partial^2 T_b}{\partial r_b^2} + \frac{1}{r_b} \frac{\partial T_b}{\partial r_b} + \frac{1}{r_b^2} \frac{\partial^2 T_b}{\partial \theta_b^2} + \frac{\partial^2 T_b}{\partial z^2} = 0 \quad (2.35)$$

, where: T_b is the lobe temperature, r_b is the radius of the bushing, and θ_b is the bushing angular position.

2.4. Boundary conditions

2.4.1. On pressure

The boundary conditions for pressure are as follows:

- At the leading edge, the pressure at the entering positions of the lobes equals the supply pressure.

$$p \Big|_{x=x_{in}} = p_{supply} \quad (2.36)$$

- At the exiting leading edge:

$$p \Big|_{x=x_{out}} = p_{supply} \quad (2.37)$$

- At the side edges:

$$p \Big|_{z=0, L} = 0 \quad (2.38)$$

2.4.2. On temperature

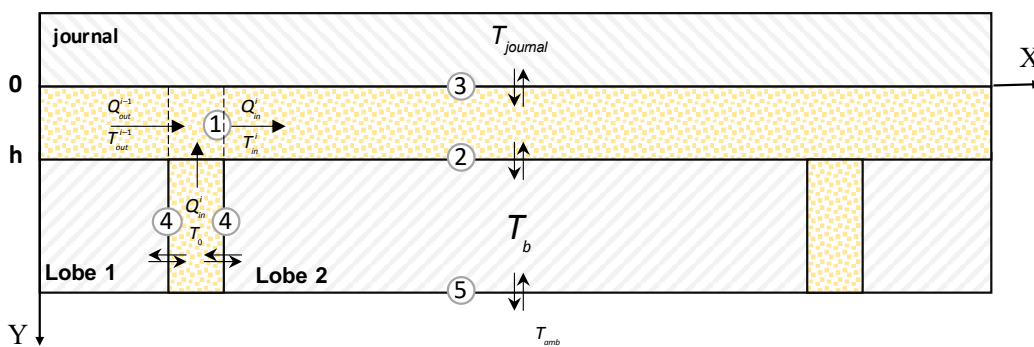


Figure 2.7. Thermal boundary conditions of a fixed geometry two-lobe journal bearing.

Fig. 2.7 describes the thermal boundary conditions of a fixed geometry two-lobe journal bearing. It is divided into five zones: zone 1 is the zone of the fluid entering the lobe i from previous lobe $(i-1)$ and from supply groove; zone 2 is at the film/bushing interface; zone 3 is at the film/journal interface; zone 4 is at the film/groove interfaces, and zone 5 is at the outer of the bush/outside medium interface.

2.4.2.1. Film inlet temperature

The first boundary condition is the entering temperature of the lubricant. It is an assumption that a portion of the lubricant from the previous lobe is mixed with the fresh lubricant fed before entering to the current lobe. The conservation of heat fluxes gives the following equation:

$$T_{in}^i = \alpha^i \left(\frac{Q_{out}^{i-1}}{Q_{in}^i} \right) T_{out}^{i-1} + \left(\frac{Q_0}{Q_{in}^i} \right) T_0 \quad (2.39)$$

, where Q_{in}^i , T_{in}^i are the entering flow rate and entering temperature of lobe i^{th} ; and Q_{out}^{i-1} , T_{out}^{i-1} are the recirculating flow rate and recirculating temperature of lobe $(i-1)^{th}$, respectively; Q_0 is the supplied flow rate, which is the same amount as the leakage flow rate out of sides. More details on this will be given in the appendix A.

2.4.2.2. At film/bushing interface

At $y=h$, the heat fluxes will be equal, and the temperatures will be:

$$T = T_b \quad (2.40)$$

$$K_f \frac{\partial T}{\partial y} \Big|_{y=h} = -K_b \frac{\partial T_b}{\partial r} \Big|_{r=R_f} \quad (2.41)$$

, where K_f is the conduction coefficient of the fluid, and K_b is the conduction coefficient of the bushing.

2.4.2.2. At film/journal interface

At $y=0$, it is considered that the temperature of the journal is constant because it usually rotates with high speeds. Therefore, the temperature of the lubricant film in these contact zones is equal to the journal temperature:

$$T \Big|_{y=0} = T_{journal} \quad (2.42)$$

$$\sum_{i=1}^{N_f} \int_{x_{in}^i}^{x_{out}^i} \frac{\partial T}{\partial y} \Big|_{y=0} dx = 0 \quad (2.43)$$

2.4.2.3. At outside bushing surfaces

The heat exchange equation:

$$K_b \frac{\partial T_b}{\partial r} \Big|_{r=R_{l,outer}} = H_{c_{ext}} \left(T_b \Big|_{r=R_{l,outer}} - T_{amb} \right) \quad (2.44)$$

, where $H_{c_{ext}}$ is convection heat transfer coefficient of the bush to outside air medium; $R_{l,outer}$ is the outer radius of the bush.

2.4.2.4. At lubricant/groove wall interface

The heat exchange equations:

$$K_b \frac{\partial T_b}{\partial x} \Big|_{x=x_{in}} = H_{c_{groove}} \left(T_b \Big|_{x=x_{in}} - T_0 \right) \quad (2.45)$$

$$K_b \frac{\partial T_b}{\partial x} \Big|_{x=x_{out}} = -H_{c_{groove}} \left(T_b \Big|_{x=x_{out}} - T_0 \right) \quad (2.46)$$

, where $H_{c_{groove}}$ is thermal exchange coefficient of the groove to the lubricant in the groove regions; x_{in}, x_{out} are the Cartesian coordinates at the inlet and outlet sections, respectively.

The coefficients of thermal exchange can be calculated for as follows:

$$H = \frac{K_L Nu}{D} \quad (2.47)$$

, where K_L is conduction coefficient of the lubricant; Nu is Nusselt number; and D is outer diameter of the bush. However, calculating the thermal heat exchange coefficients using the Nusselt number may be not accurate for journal bearing; therefore, the coefficients often chosen based on experience in studies on journal bearings.

2.5. Bearing global parameters

2.5.1. Lubricant film force and load capacity

Fig. 2.8 describes all the forces acting on the bearing. The lubricant film force F is obtained by integrating the oil film pressure p in circumferential and axial directions.

$$F = \int_0^L \int_0^{2\pi R_j} p dx dz \quad (2.48)$$

This force equal to the applied load on the bearing W . The position at which the hydrodynamic force balances the applied load is the equilibrium position of the bearing. By projecting both this force and the applied load W to the coordinate system $(O_j k \ell)$, where the axis $O_j k$ is coincident to the center line and $O_j \ell$ is perpendicular to the axis $O_j k$, we have:

$$\begin{cases} F_k = \int_0^L \int_0^{2\pi R_j} p \cos(\theta^* - \phi_0) dx dz \\ F_\ell = \int_0^L \int_0^{2\pi R_j} p \sin(\theta^* - \phi_0) dx dz \end{cases} \quad (2.49)$$

The force equilibrium equations of the bearing can be determined as follows:

$$\begin{cases} W \cos \phi_0 = F_k \\ W \sin \phi_0 = F_\ell \end{cases} \quad (2.50)$$

The attitude angle ϕ_0 then can be calculated as follows:

$$\phi_0 = \arctg\left(\frac{F_\ell}{F_k}\right) \quad (2.51)$$

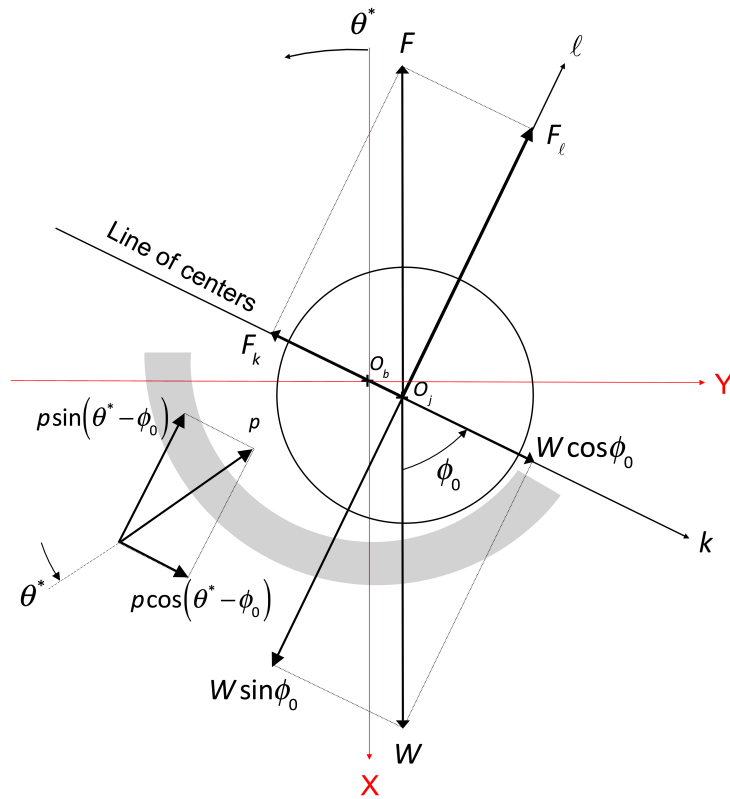


Figure 2.8. Hydrodynamic forces and applied bearing load.

2.5.2. Flow rates

Fluid flow rates are important parameters which are used to evaluate the heat exchange of the fluid at the entering and exiting regions of the fluid, but also the flow balance which corresponds to the conservation of mass of the bearing. The flow rates calculated for each lobe of the bearing are calculated as follows:

- The entering flow rate at the fluid section $x = x_{in}$ (or $\theta = \theta_{i1}$) is calculated by integrating the velocity component u over the axial direction and the film-across direction:

$$Q_{in} = \int_0^L \int_0^h u(x_{in}, y, z) dx dz \quad (2.52)$$

- The exiting flow rate at the fluid section $x = x_{out}$ (or $\theta = \theta_{i2}$) is calculated in the same way:

$$Q_{out} = \int_0^L \int_0^h u(x_{out}, y, z) dx dz \quad (2.53)$$

- The axial flow rates or the leaking flows at the sides of the bearing are calculated by integrating the velocity component w in the circumferential direction and the film-across direction:

$$Q_{axial} = \int_{x_{in}}^{x_{out}} \int_0^h w(x, y, 0) dx dy + \int_{x_{in}}^{x_{out}} \int_0^h w(x, y, L) dx dy \quad (2.54)$$

- To evaluate the flow conservation, a flow balance parameter B_{flow} is defined as:

$$B_{flow} = \frac{Q_{in} - (Q_{out} + Q_{axial})}{Q_{in}} \quad (2.55)$$

- In an ideal case where the volume flow rates are fully conserved, the flow balance equal to 0, others will be greater than 0.

2.5.3. Friction torque and power losses

- Shearing stress acting on the surface of the bushing is calculated as follows:

$$\tau_{l,xy} = \left(h - \frac{J_1}{J_0} \right) \frac{\partial p}{\partial x} - \frac{\omega R_l}{J_0} \quad (2.56)$$

- The friction torque on the bushing surface is calculated as:

$$M_l = \int_0^L \int_0^{R_l} \tau_{l,xy} \Big|_{y=h} R_l dx dz \quad (2.57)$$

- Shearing stress acting on the surface of the journal is calculated as follows:

$$\tau_{j,xy} = \frac{J_1}{J_0} \frac{\partial p}{\partial x} - \frac{\omega R_j}{J_0} \quad (2.58)$$

- By integrating the shearing stress in the circumferential and axial directions, the friction torque on the journal is obtained:

$$M_j = \int_0^L \int_0^{R_j} \int_0^{2\pi} \tau_{j,xy} \Big|_{y=0} R_j dx dz \quad (2.59)$$

- By multiplying the friction torque with the angular velocity of the journal, the power loss of the bearing is determined:

$$P = M_j \omega \quad (2.60)$$

2.6. Conclusions

This chapter provided all necessary equations to determine a full thermohydrodynamic solution for multi-lobe journal bearings lubricated with an incompressible fluid. The generalized Reynolds equation for pressure fields in the film, the energy equation for fluid temperature at every point of the film, the Laplace heat conduction equation for the surrounding solids, and bearing global parameters, were all developed. Next chapter will present methods to solve these equations and applications for scratched journal bearings.

Chapter 3. Numerical analysis

3.1. Discretization

The partial differential equations in chapter 2 must be discretized into a system of algebraic equations and solved numerically. There are several methods to do this discretization, the most three popular methods are finite difference, finite element, and finite volume methods. These three methods have both of their advantages and disadvantages.

In the finite difference method, the partial derivatives are replaced with a series expansion representation, usually a Taylor series with an optional truncation of terms. The higher number of terms in the expansion causes higher complexity of the system of equations and higher difficulty for a solution convergence. One of the most advantage of this method is that it is straightforward to apply for regular shape geometry. However, for the irregular or discontinuity shaped geometries it might introduce sorts of problems mesh generation and general convergence.

In the finite element method, methods of weighted residuals are generally used. In this method, the governing partial differential equations are integrated over an element after having been multiplied by a weight function. The dependent variables are represented on the element by a shape function, which is the same form as the weight function. The major drawback of finite elements is that it is a heavily mathematical approach and leads to less physical significance. This method is widely used in solid mechanics.

In the finite volume method, the governing equations are integrated over a control volume, using an assumption of a piece-wise linear variation of the dependent variables. By using these integrations, fluxes across the boundaries of the individual volumes must be balanced. This is a major advantage of this method in terms of physical significance when fluxes e.g. mass and heat flux, are crucial. Finite volume method can be applied straightforward for a regular domain, however, for irregular domains it might require further effort to calculate fluxes correctly.

We chose the finite volume method for the discretization because the fluxes and mass balance are crucial variables in this study. Another reason is this method also allows to solve the discontinuous problem of the domain mesh because of the presence of scratches on the shaft that cannot be solved by using the finite difference method. The development programming language used is Fortran 90 [56], in order to take advantage from the codes developed by previous researchers (codes of Jean Bouyer and Celia Giraudeau) , and it is one of the speediest computer programming for numerical computing. Resolution of hydrodynamic and thermal-hydrodynamic resolution are presented. Initially, we are interested in choosing discretization and resolution method for the calculation of the pressure field. During this study, several methods of resolution are reviewed and compared to explain the choice made. Finally, several case studies are presented to illustrate and verify the development.

Bonneau et al. in [57,58] describe in detail three discretization methods used to solve hydrodynamic bearing problems: finite differences, finite volumes, and finite elements. They proposed a discretization of the global generalized Reynolds equation, which allows to obtain the pressure and filling fields simultaneously for the three methods.

Finite volume method is well known and described in detail in works of many specialists, such as Versteeg and Malalasekiva [59], Patankar [60], [61] and many others. Therefore,

it will not be presented here, we only present an application for our study of a journal bearing of uniform width, in a developed bearing configuration. Fig. 3.1 presents a 2D mesh domain Ω deployed into rectangular volumes, and each volume has dimensions Δx and Δz in X, Z directions, respectively. The computational points are located in the center of the volumes and also on the bearing edge for the boundary conditions. The distances between the centers of the control volumes are dx and dz . Fig. 3.2 shows a typical control volume named as P, it has four adjacent or neighbor volumes designated as capital letters W, E, S, N, which represents the adjacent volumes from west, east, south, and north sides, respectively. The adjacent edges of the volume P to the west, east, south, and north neighbor volumes are notated as lower letters w, e, s, n respectively.

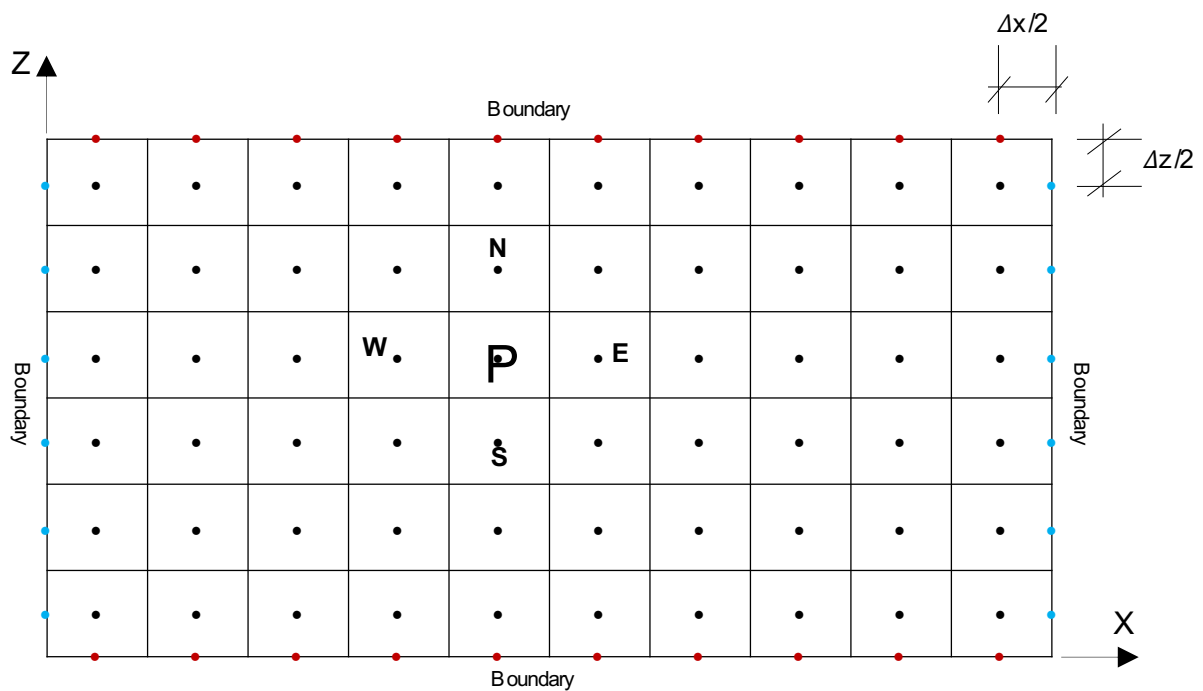


Figure 3.1. Finite volume mesh.

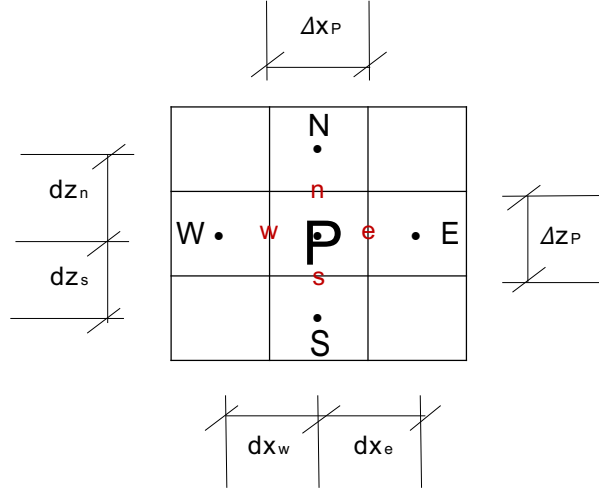


Figure 3.2. Typical control volume.

To apply the finite volume method, the generalized Reynolds equation is integrated on each typical control volume:

$$\int_s^e \int_w^e \left(\Phi \left[\frac{\partial}{\partial x} \left(G \frac{\partial D}{\partial x} \right) + \frac{\partial}{\partial z} \left(G \frac{\partial D}{\partial z} \right) \right] - \rho \left[U \frac{\partial (J_1 / J_0)}{\partial x} + (1 - \Phi) \frac{U}{2} \frac{\partial D}{\partial x} \right] \right) dx dz = 0 \quad (3.1)$$

with approximations:

$$\begin{aligned} \int_s^e \int_w^e \Phi \frac{\partial}{\partial x} \left(G \frac{\partial D}{\partial x} \right) dx dz &= \left[G_e \frac{\Phi_e D_e}{dx_e} - G_w \frac{\Phi_w D_w}{dx_w} \right] \Delta z_p \\ \int_s^e \int_w^e \Phi \frac{\partial}{\partial z} \left(G \frac{\partial D}{\partial z} \right) dx dz &= \left[G_n \frac{\Phi_n D_n}{dz_n} - G_s \frac{\Phi_s D_s}{dz_s} \right] \Delta x_p \\ \int_s^e \int_w^e \frac{\partial D}{\partial x} dx dz &= \left(\frac{D_e + D_w}{2 \Delta x} \right) \Delta z_p \end{aligned} \quad (3.2)$$

By carrying over these expressions in equation (3.1), the discretization equation for each typical control volume is obtained:

$$A_p D_p + A_w D_w + A_e D_e + A_s D_s + A_n D_n + S_c = 0 \quad (3.3)$$

By applying the equation is for each control volume and taking into account boundary conditions at boundary points, a system of global linear equations is obtained and can be expressed in a matrix notation:

$$[A]\{D\} = \{S\} \quad (3.4)$$

where $[A]$ is a coefficient matrix, $\{D\}$ is the vector matrix of the volume variable values, and $\{S\}$ is the corresponding vector matrix of source terms. Each row of the matrix A includes coefficients of the unknown variables in one equation of the system. Next subsection describes methods to achieve the solution.

3.2. Solutions of system of equations

Solution of large sets of equations in Eq. (3.4) can be achieved by both direct and iterative methods. A direct method achieves the solutions in a finite number of steps, and the solution is equivalent to $\{D\} = [A]^{-1}\{S\}$. One of the most popular direct methods is Gaussian elimination and LU decomposition. These methods usually require excessive computational effort. On the other hand, iterative methods obtain a sequence of approximations $\{D\}^{(k)}$ ($k = 1, \dots, n$) to the solution $\{D\}$ with a pre-defined a stopping criterion.

3.2.1. Direct solutions

Direct solution of linear algebraic systems is obtained by the method of substitution in which equations are substituted into other equations to reduce the number of unknowns until they are all determined. The direct solution obtained by a direct solver is considered as a numerical exact solution. The only sources of error are truncation and round-off errors, and of course the discretization approximation errors. It is the advantage of the direct solution. Gaussian elimination is the most general method of the direct solution, which based on addition and elimination operations. This method is time-consuming because the entire coefficient matrix, including all zeroes, is stored and used; therefore, it is inefficient and prohibitive for

solution of large systems. The LU decomposition is a better way to implement Gauss elimination. In this method, matrix $[A]$ is written as a product of a lower triangular matrix $[L]$ and an upper triangular matrix $[U]$:

$$[A] = [L][U] \quad (3.5)$$

Then, Eq. (3.4) became:

$$[L][U]\{D\} = \{S\} \Leftrightarrow \begin{cases} [L]\{y\} = \{S\} & (a) \\ [U]\{D\} = \{y\} & (b) \end{cases} \quad (3.6)$$

The system (a) is solved to find the vector $\{y\}$, then the system (b) is solved to find the vector $\{D\}$. The resolution is facilitated by the triangular shape of the matrices and less computer cost compare to the Gauss elimination method. Another noting point is that the calculation of matrices $[U]$, $[L]$ uses only coefficients of matrix A and does not use the source term vector $\{S\}$, which differs from the Gauss elimination method. It means that once the decomposition is successfully obtained, it can be used for different values of vector $\{S\}$. However, both LU decomposition and Gauss elimination require $O(N^3)$ operations. It is the major disadvantage of these methods, especially when the system of equations is large; therefore, applying the direct methods is inefficient from a memory usage and a computational efficiency standpoint.

3.2.2. Indirect solutions

Because of the drawbacks of the direct solution methods, iterative solution methods are good alternatives. In this section, two of the most popular iterative solution methods, namely Gauss-Seidel method, and Stone's Strongly Implicit method (SIP) are described.

3.2.2.1. Gauss-Seidel and SOR methods

The principle of this method is to iteratively solve equation Eq. (3.3) explicitly for every calculation point until convergence is obtained for all the mesh points of the domain.

To perform it, Eq. (3.3) is rewritten in an iterative form as Eq. (3.7).

$$D_p^{(k)} = \frac{S_p - A_W D_W^{(k-1)} + A_E D_E^{(k-1)} + A_S D_S^{(k-1)} + A_N D_N^{(k-1)}}{A_p} \quad (3.7)$$

This equation is solved iteratively until a convergence criterion condition ε_p for the solution is reached as defined in Eq. (3.8):

$$\left| \frac{D_p^{(k)} - D_p^{(k-1)}}{D_p^{(k)}} \right| < \varepsilon_p \quad (3.8)$$

This method has been used widely although it has some disadvantages: for example, it is still slow, and sometimes, it produces oscillations in solution. However, these drawbacks can be improved by introducing the relaxation coefficients added to the equation, and these methods are known as successive over relaxation (SOR) methods, Eq. (3.9):

$$D_p^{(k)} = \omega D_p^{(k)} + (1 - \omega) D_p^{(k-1)} \quad (3.9)$$

, where ω is the relaxation coefficient. When $\omega = 1$, it becomes Gauss-Seidel, when $\omega > 1$, it accelerates the iterations to the solution and is called over-relaxation. When $\omega < 1$, it decelerates the iterations towards the solution and is called under-relaxation. The over-relaxation is usually used at the first iterations to save computing time and turn to under-relaxation when the current solution is getting close to the exact solution, thus allowing to prevent oscillations mentioned before. It has been proved in literature that these methods are faster in orders of ten times compared to direct methods mentioned before.

3.2.2.2. Stone's Strongly Implicit method

This strongly implicit method for banded systems was first proposed by Herbert Stone in 1968 [62]. Since then, it has grown tremendously in popularity, and is now considered one of the most efficient solvers for banded systems arising out of discretization of a multidimensional partial differential equation (PDE). In this section, we will discuss its formulation in the context of the five-band system arising out of discretization of a 2D PDE. The idea of Stone is to convert the five-band equation to their correction form so that it can be solved iteratively.

$$[M]\{\{D^{(k+1)}\}-\{D^{(k)}\}\}=\{S\}-[A]\{D^{(k)}\} \quad (3.10)$$

$$[M]\{\delta^{(k)}\}=\{R^n\} \quad (3.11)$$

where $[M]$ is an iteration matrix; $\{\delta^{(k+1)}\}=\{D^{(k+1)}\}-\{D^{(k)}\}$ is the correction vector from iteration k^{th} to $(k+1)^{\text{th}}$; $\{R^n\}=\{S\}-[A]\{D^{(k)}\}$ is the residual after iteration k^{th} .

Stone proposed factorizing the matrix $[M]$ into a lower triangular matrix $[L]$, and an upper triangular matrix $[U]$:

$$[L][U]\{\delta^{(k)}\}=\{R^n\} \Rightarrow \begin{cases} \{Y^{(k)}\}=[U]\{\delta^{(k)}\} & (a) \\ [L]\{Y^{(k)}\}=\{R^{(n)}\} & (b) \end{cases} \quad (3.12)$$

Then, equations (3.12a) and (3.12b) enable the splitting of the solution into a two-step process of one forward and one backward substitution. First, Eq. (3.12a) is solved with a forward substitution to obtain vector $\{Y^{(k)}\}$. Next, Eq. (3.12b) is solved by a backward substitution to obtain vector $\{\delta^{(k)}\}$. The solution of these two equations can be considerably more efficient because both $[L]$ and $[U]$ matrices are already triangular and would only require either a forward or backward substitution, but no forward elimination, which is the most time-consuming part of the Gaussian elimination algorithm. It becomes clear why solution of Eq.

This equation provides the relationships necessary to compute the elements of the [L] and [U] (Fig. 3.4) from the elements of the original [A] matrix. These relationships are based on the approximate factorization with Stone's factor α . The range of $\alpha = 0.92 \div 0.94$ is also recommended by Stone.

The two most time-consuming steps in the SIP solution are the forward and backward substitution steps to find $\{\delta^{(k)}\}$ and $\{Y^{(k)}\}$. Since both the [L] and [U] matrices have only three bands each, the long operation count in the forward substitute on step is only $O(3N)$, compare to $O(N^3)$ in Gauss and general LU solution [63]. Therefore, theoretically the SIP method results in a good scalability as far as the long operation count is concerned, making it one of the most efficient method for banded linear systems. Giraudeau et al. [41] also confirmed it in their works.

3.2.2.3. Stone's Strongly Implicit procedure for 3-D problems

The SIP method described in section 3.2.1.2 is for a resolution of a system with a five-diagonal coefficient matrix in 2-D problems, this section presents the SIP solution developed for three-dimensional cases with a seven-diagonal coefficient matrix. Now, we consider the system in Eq. (3.4), where [A] is a (N.N) square coefficient matrix; with $N = (N_x \cdot N_y \cdot N_z)$ the number of control volumes (N_x, N_y, N_z are the number of volumes in three directions X, Y, Z, respectively); {D} is the vector of the variables, and {S} is the vector of the corresponding source terms.

The one-dimensional storage index of the variable vector {D}, ijk , is calculated from the three-dimensional grid indices i, j and k in X, Y, Z directions, respectively. The storage index is defined as follows:

$$ijk = (k - 1)N_{xy} + (j - 1)N_x + i \quad (3.14)$$

where $i = 1, \dots, N_x$; $j = 1, \dots, N_y$; $k = 1, \dots, N_z$; $N_{xy} = N_x \cdot N_y$ is the number of volumes in XY plane and $N_{xyz} = N_x \cdot N_y \cdot N_z$ is the number of total control volumes. Thus, the indices of neighboring volumes are $(ijk - 1)$, $(ijk + 1)$, $(ijk - N_x)$, $(ijk + N_x)$, $(ijk - N_{xy})$, $(ijk + N_{xy})$ associated with the west, east, south, north, bottom, and top volume, respectively (Fig. 3.5).

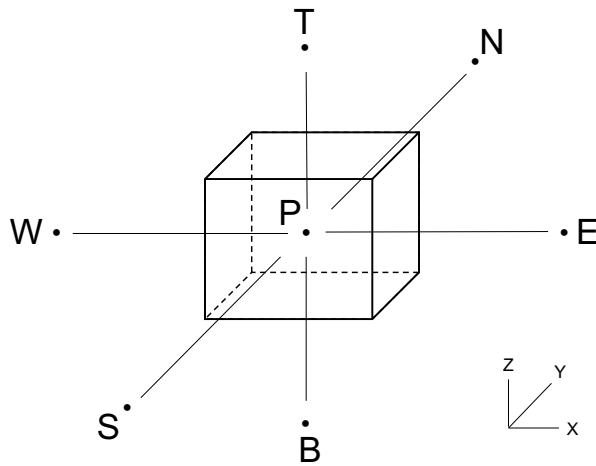


Figure 3.5. A 3-D typical control volume.

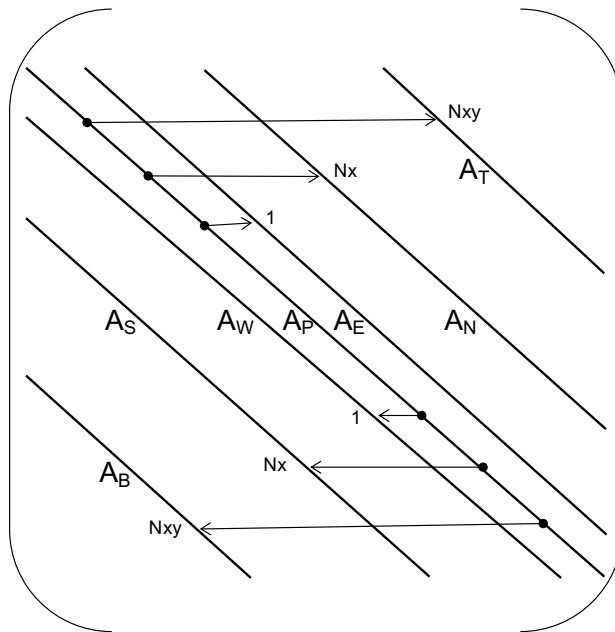


Figure 3.6. A 3-D SIP iteration matrix [M].

3.2.2.4. Vectorizing the Stone's Strongly Implicit Procedure

It has to be observed that the system in Eq. (3.12) is strongly recursive, which involves data dependency; for example, computer operation at one loop step depends on the previous step. This type of structure limits the advantage of vector computers. However, the recursive structure of SIP can be resolved partly by restructuring the program in a vectorized form to take the advantage of vector or parallel computing [64] [65], . A restructured scheme for a two-dimension case is shown in Fig. 3.8. In a normal order, computer points are calculated in row and column order, which is in such a way that index k in Z direction is constant and stacked one above another, and within one k , the index i in X direction is increased. This structure is recursive because calculating point index $ik = (k-1)N_x + i$ requires newly computed point $(ik-1)$ of the left; thus, point $(ik-1)$ must be calculated first. The dependency is the same for the other points in the same row. This limitation can be solved partly by calculating points in diagonal order, instead of normal row and column order. It can be seen that all points on the same diagonal can be calculated independently from the previous point because they only depend on the points on the left diagonal. Therefore, all points in one diagonal can be calculated independently and parallel. Thus, the recursion in a level of scalar points in each diagonal can be eliminated, and only exist in a level of diagonals; in other way, it is partially resolved as mentioned before. This technique can be applied for a three-dimensional solution in the same manner. Imagine a three-dimension domain in which computer points on any diagonal planes are calculated without recursion. These planes can be triangle or polygon; an example of a triangle plane cut is shown in Fig. 3.9. Leister et al. [66] successfully deployed this technique in their works and recommended choosing the plane cuts such that all the computer points should be from one coordinate surface, e.g. $(i+j+k) = \text{constant}$. All data points

from each plane can be assigned in one vector called a SIP vector, and computing process starts for one SIP vector to another sequentially. The details can be found on [66].

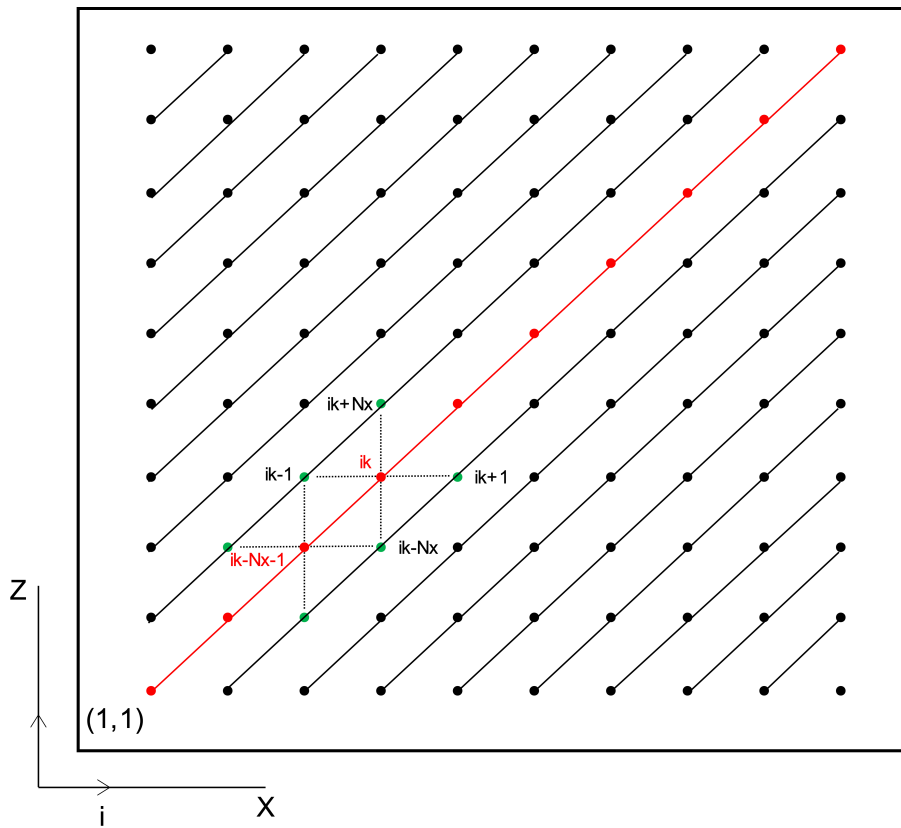


Figure 3.8. A 2-D restructured scheme.

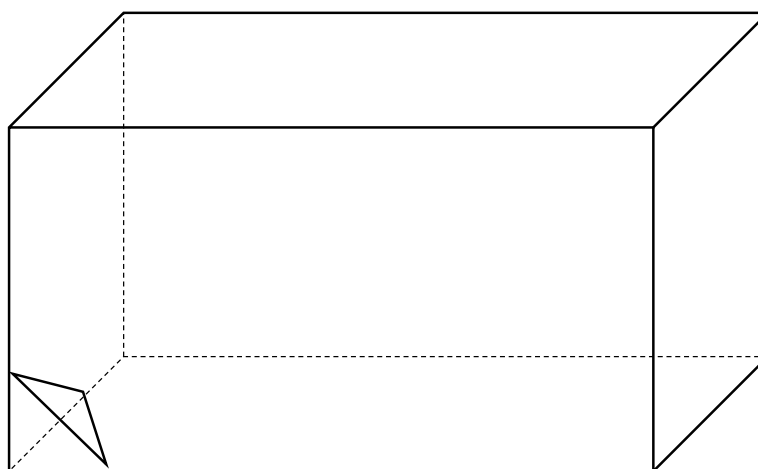


Figure 3.9. A 3-D restructured scheme.

Fig. 3.10 shows a comparison between three-dimension non-vectorized SIP structure and its vectorized version for several numbers of grids. The case study is a two-lobe preloaded journal bearing with a high applied load of 8000 N and high speed of 3500 rpm, with THD simulations. It can be seen that the computing time of the vectorized structure decreases by about 40% compared to the non-vectorized structure. In the works of Giraudeau et al. [41], it is shown that SIP solvers run faster than Gauss- Seidel and LU solvers with an order of ten times. This study shows that it can be even faster by restructuring the solution in a vectorized form.

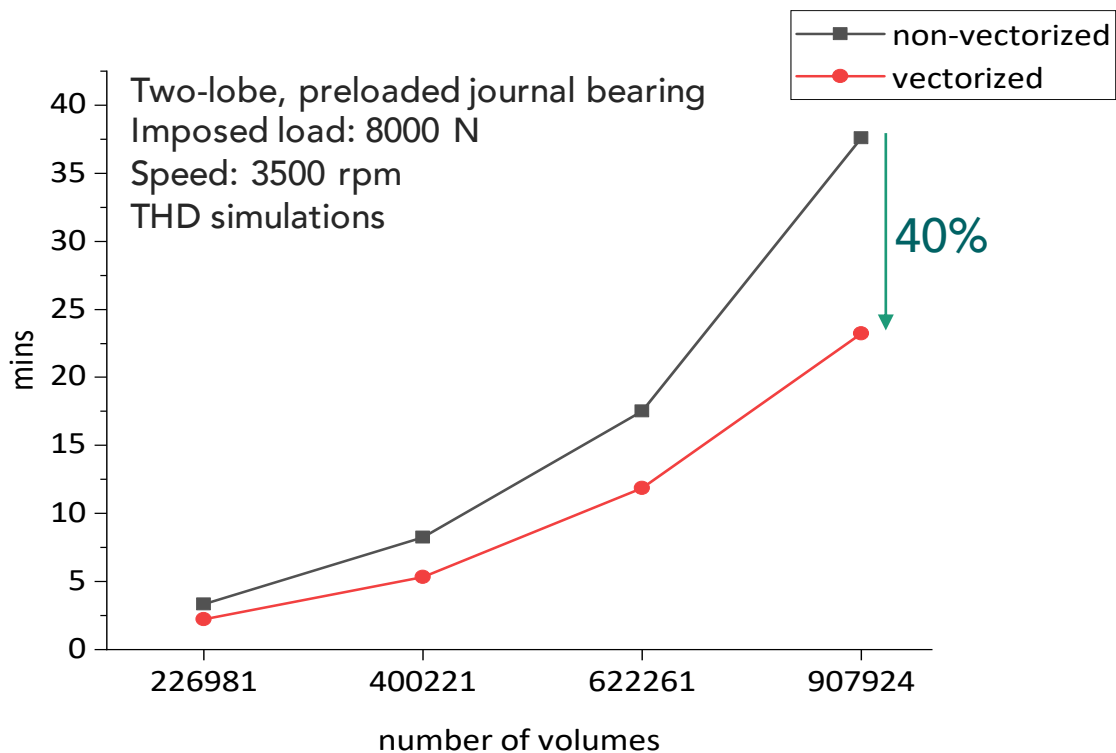


Figure 3.10. Computer time for non-vectorized SIP versus vectorized SIP.

As a conclusion, the SIP method outperforms the direct methods in terms of both computer storage and calculation time. The recursion of the solution algorithm unfortunately is unavoidable; however, it can be resolved partially by restructuring the program so that it can be processed in a vectorized manner. The performance of the vectorized SIP method was

proven, with high efficiency, fast convergence, low computing time. For those reasons, in this study we chose this method to build our solver.

3.3. Geometrical study

3.3.1. Two-lobe journal bearing geometry

Fig. 3.11 describes the geometry of a two-lobe journal bearing which is the object of this study. This bearing was used for Yann Alexandre's experimental studies and the data was available for comparing with the simulation results in this study [55]. The bearing has a preload factor a , other dimensions and lubricant characteristics can be found on Table 3.1. Fig. 12 shows a scratch profile which is machined on the surface of the shaft in circumferential direction. Three main parameters to define the scratch are: the scratch width, w , which varies from 1 mm to 8 mm; the scratch depth, δ , which varies as a function of the bearing clearance from 0 to $2C$, and the axial position of the scratch, L_s .

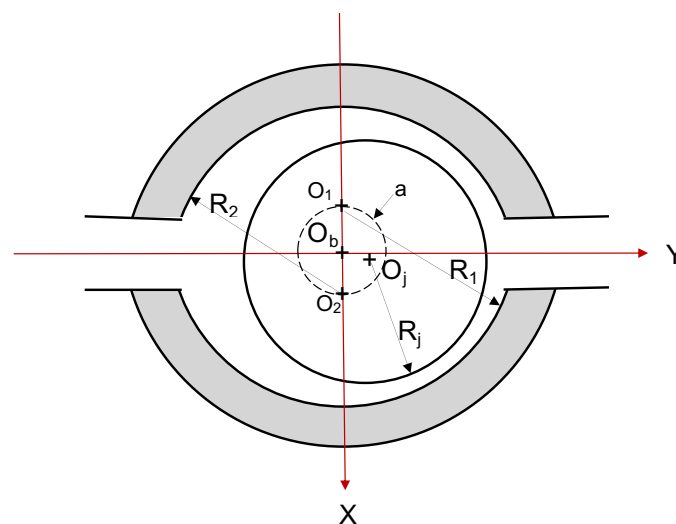


Figure 3.11. A two-lobe journal bearing.

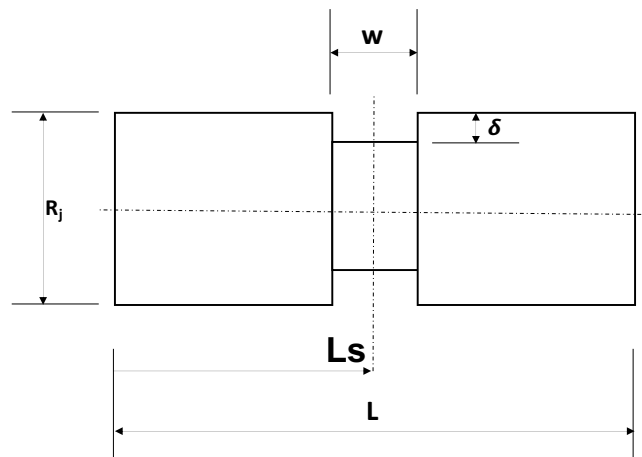


Figure 3.12. Three main parameters of a scratch on the journal.

Table 3.1. Bearing and lubricant characteristics.

PARAMETERS		unit
Bearing dimensions		
Shaft diameter	99,908	mm
Lobe diameter	100,058	mm
Bearing length	68,4	mm
Angular lobe length	145	deg
Preload	0.524	
Scratch geometry		
Scratch width	1-8	mm
Scratch depth	0-2C	μm
Scratch position	$L/2, L/3, L/6, L/12, \dots$	
Number of scratches	0-16	
Lubricant properties		
Lubricant viscosity at 40 °C	0.0416	Pa·s
Lubricant viscosity at 60 °C	0.0191	Pa·s
Lubricant density	870	kg/m^3
Feeding pressure	0.17	MPa
Ambient pressure	0.1	MPa
Feeding temperature	43	°C
Operating conditions		
Load	1000-10000	N
Shaft speed	500-3500	rpm

3.3.2. Study of lubricant film domain

3.3.2.1. Meshing methods

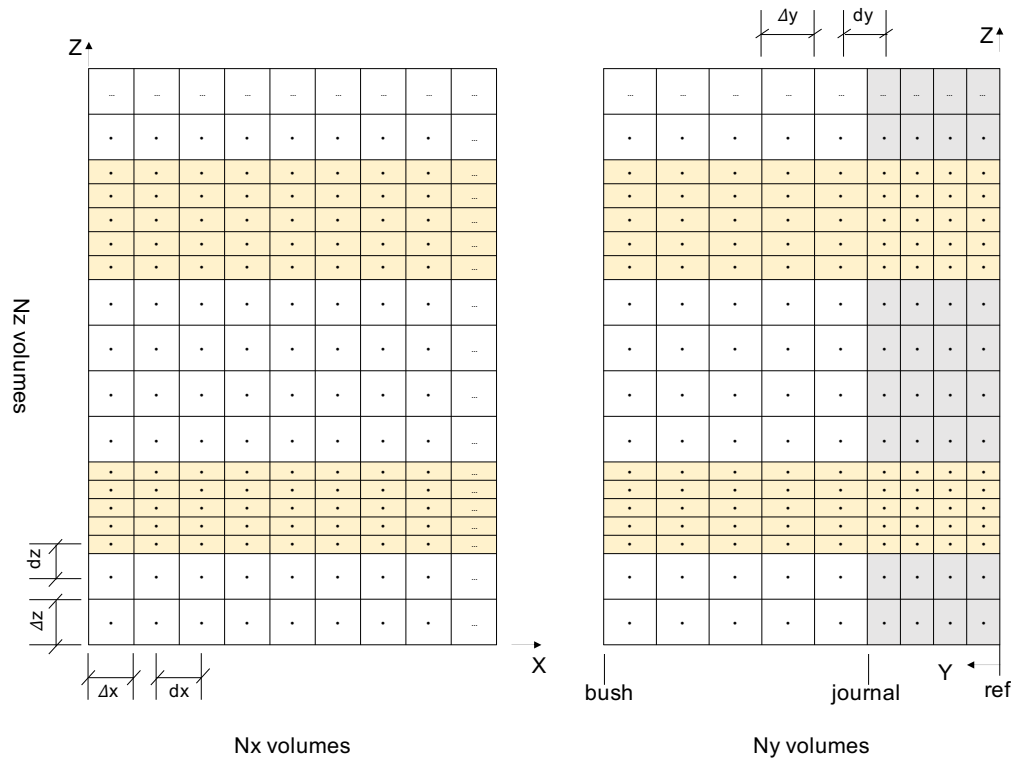


Figure 3.13. Lubricant film mesh.

Three-dimensional lubricant domain is deployed to 2D planes XZ and YZ in Fig. 3.13 which gives the example of a two-scratch case. The X, Y, Z directions correspond respectively to the bearing circumferential direction, the direction across the lubricant film, and the bearing axial direction. The number of control volumes in X, Y, Z directions are N_x , N_y , N_z , respectively. The sizes of control volumes can be uniform or non-uniform, each volume has a size of $\Delta x \cdot \Delta y \cdot \Delta z$. The shaded yellow regions are scratch zones, the gray shaded regions are virtual volumes. The real physical positions of these virtual volumes are in the journal, but we meshed them together with the lubricant film to keep the mesh shape in YZ direction as a rectangle. This sort of mesh facilitates the process of indexing the computer points and loops,

and of imposing boundary values. It is especially useful when there are multiple scratches on the shaft surface where it becomes hard to perform the mesh.

The size of volumes in circumferential direction Δx are designed uniform because there is no mesh discontinuity in this direction. The volume sizes across the film direction Δy are different and dependent on the lubricant film thickness at each section in the circumferential direction.

The volume sizes in the axial direction Δz however more complex because the scratches arranged along with this direction and create a discontinuity in the mesh. Fig. 3.14 describes three methods to design the mesh in axial direction Z: uniform mesh, adaptive mesh redistribution, and adaptive mesh redistribution with uniform subsections.

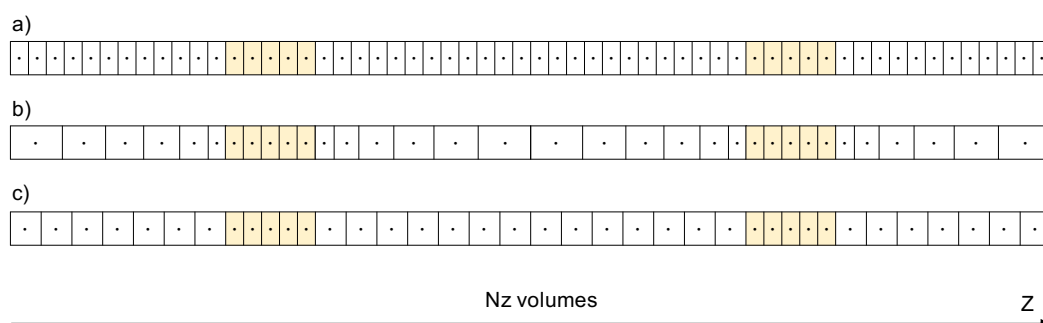


Figure 3.14. Three meshing methods: a) uniform mesh; b) adaptive mesh redistribution; c) adaptive mesh redistribution with uniform subsections.

The scratch widths are small compare to the length of the bearing in general, so the volume size Δz of volumes inside scratches are designed with a uniform size, and the number of volumes in each scratch zone must be greater than three volumes. Fig. 3.14(a) presents the uniform mesh method in which all the volume size Δz is uniform; it is the most straightforward method to create the domain mesh. However, the major drawback of this method is that the number of volumes in this direction will be large because the ratio between the length of the bearing and the scratch width is usually large.

To deal with this problem, adaptive mesh redistribution methods can be applied, in which the volume sizes Δz are not necessary uniform, but can be of different sizes in different mesh regions. Fig. 3.14(b) and Fig. 3.14(c) show two different ways to perform the adaptive mesh redistributions. In the mesh in Fig. 3.14(b), volume sizes Δz are designed by the means of a geometric sequence in which each volume size is calculated by multiplying the previous volume size by a pre-defined constant value called common factor. By applying this method, the number of volumes in the z direction will be decreased, but still keeping the resolution in particular locations of the domain. The mesh in Fig. 3.14(c) is another adaptive mesh redistribution, in which the volume size in each subsection is uniform, this method can either reduce the number of volumes as well.

In order to evaluate and compare the three mesh methods, a simulation test in isothermal condition with imposed load of 8,000 N and speed of 3,500 rpm, two 50 μm scratches at $L/2$ and $L/3$, was done and the results presented in Table 3. 2. The number of volumes in X, Y directions are 202 and 122, respectively. The number of volumes in Z direction for three meshing methods a), b), and c) are 117, 72, 76, respectively. Important global parameters of bearing performance i.e. the calculated eccentricity ratio, attitude angle, minimum film thickness, maximum pressure are compared to evaluate the accuracy of the calculated solutions. Computing time, which is a crucial parameter for simulation studies, is also compared as well. The relative standard deviation (RSD) of the criteria are calculated to evaluate the distribution of the solutions among the three methods. It can be seen that RSDs for calculated eccentricity ratio and attitude angle are less than 0.1%, and that of the minimum film thickness and the maximum pressure are less than 0.2%. These results show that the differences in the solutions among the three methods are small, meaning all the

three methods can perform same work and result in similar solutions. However, the computing time for the regular uniform mesh method is almost double compared to the two adaptive mesh redistribution methods. Therefore, the adaptive mesh redistributions are encouraged, and they are used in this study.

Table 3.2. A comparison among the three methods with: $N_x=202$, $N_y=122$.

Parameters	method a	method b	method c	RSD (%)
Nz	117	72	76	
Total volume	23,634	14,544	15,352	
Relative eccentricity	0.3407	0.3411	0.3412	0.0644
Attitude angle (°)	86.0204	86.0089	85.9906	0.0143
Hmin (μm)	50.8000	50.7000	50.7000	0.0929
Pmax (MPa)	3.5635	3.5539	3.5707	0.1928
Computing time (min)	5.7549	2.6036	3.1122	

3.3.2.2. Influence of mesh density

This section studies the density of the lubricant film mesh, i.e., the number of control volumes along three directions to evaluate the influence of them on the convergence and the accuracy of solutions. Table 3.3, Table 3.4, and Table 3.5 show results on the influences of number of volumes in X, Y, Z directions, respectively, to solution accuracy. The method of evaluating the differences in accuracy of solutions is the same as the previous simulation, using the relative standard deviation of solutions. The RSD values for the all the converged variables ranged from 0.03 to 0.2%. This small range of RSD values leads to two main conclusions: the first one is that the program successfully converged to solutions; and the second one is that using many control volumes is not necessary because the solution accuracy does not change much.

On the other hand, using large number of volumes scales up the computing time. For example, increasing N_x from 102 to 402 rises sixfold the computing time. Increasing N_z from

72 to 248 results in the same ratio. By rising N_y for 30 to 244 only increase computer time 47%. As a conclusion, the number of control volumes must be chosen properly to have efficient computing, from a balance between solution accuracy and computing time.

Table 3.3. Effect of number of volumes in circumferential direction N_x ($N_y=122$, $N_z=140$).

Parameters	42	102	202	402	RSD (%)
Total volume	5880	14280	28280	56280	
Relative eccentricity	0.3223	0.3218	0.3219	0.3219	0.0717
Attitude angle (°)	85.7910	85.9326	85.9552	85.9626	0.0938
Hmin (µm)	52.1332	52.2756	52.2789	52.2834	0.1399
Pmax (MPa)	3.7680	3.7635	3.7684	3.7669	0.0585
Computing time (min)	1.5935	3.9573	9.4844	24.0010	

Table 3.4. Effect of number of volumes in cross-film direction N_y ($N_x=102$, $N_z=140$).

Parameters	30	62	122	244	RSD (%)
Relative eccentricity	0.3225	0.3221	0.3219	0.3217	0.1033
Attitude angle (°)	86.2972	86.0594	85.9582	85.9073	0.2011
Hmin (µm)	52.4626	52.3359	52.2877	52.2657	0.1683
Pmax (MPa)	3.7583	3.7635	3.7665	3.7681	0.1145
Computing time (min)	8.6117	8.2297	9.5568	12.2742	

Table 3.5. Effect of number of volumes in axial direction N_z ($N_x=101$, $N_y=122$).

Parameters	46	72	140	248	RSD (%)
Total volume	4646	7272	14140	25048	
Relative eccentricity	0.3227	0.3222	0.3219	0.3221	0.1133
Attitude angle (o)	85.8771	85.9219	85.9552	85.9318	0.0381
Hmin (µm)	52.1564	52.2320	52.2789	52.2422	0.0984
Pmax (MPa)	3.7746	3.7759	3.7684	3.7661	0.1258
Computing time (min)	2.4995	4.0724	9.4844	21.1766	

3.4. Program flow chart and verifications

3.4.1. Schematic flow chart of the numerical program

Fig. 3.15 describes the flowchart for the numerical program for THD solutions. The governing equations consisted in a two-dimensional Reynolds equation, a three-dimensional energy equation of the lubricant film, a three-dimensional Laplace heat conduction in the solids, and a viscosity-temperature relation.

The program starts by reading input data, and initial values of parameters e.g. initial pressure, temperature, attitude angle, eccentricity, and other necessary parameters, as a first step. The second step is to calculate the fluid film thickness. The third step is to calculate the viscosity with an initial temperature (which will be updated from the second iteration of the loop). Next, the program solves the Reynolds equation to obtain the film pressure, and the calculate the velocity using the calculated pressure data. After having the velocity data plus initial boundary conditions of the film (which will be updated from the second iteration of the loop), it solves the energy equation for the film temperature and update at the temperatures at the boundaries (at film/journal, film/bush interface, inlet, and outlet). The film/bush interface temperature is calculated by the heat continuity equation at that surface. Next step solves the Laplace equation for the heat-conduction for the bush temperature. All the steps from the third step to the current step are repeated with newly updated temperatures until the stop criteria in temperatures are met. After the temperatures are converged, next step calculates the load capacity and the attitude angle of the bearing. All the steps from the second step to the current step are repeated with a newly updated attitude angle until the stop criteria in the attitude angle is met. When the attitude angle is converged, the next step is to

check the stop criteria in load capacity. If it is not met, then all the step from the second step to current step are repeated with a newly updated eccentricity until the stop criteria in the load capacity is met. Last step is to write results to files and finish the program.

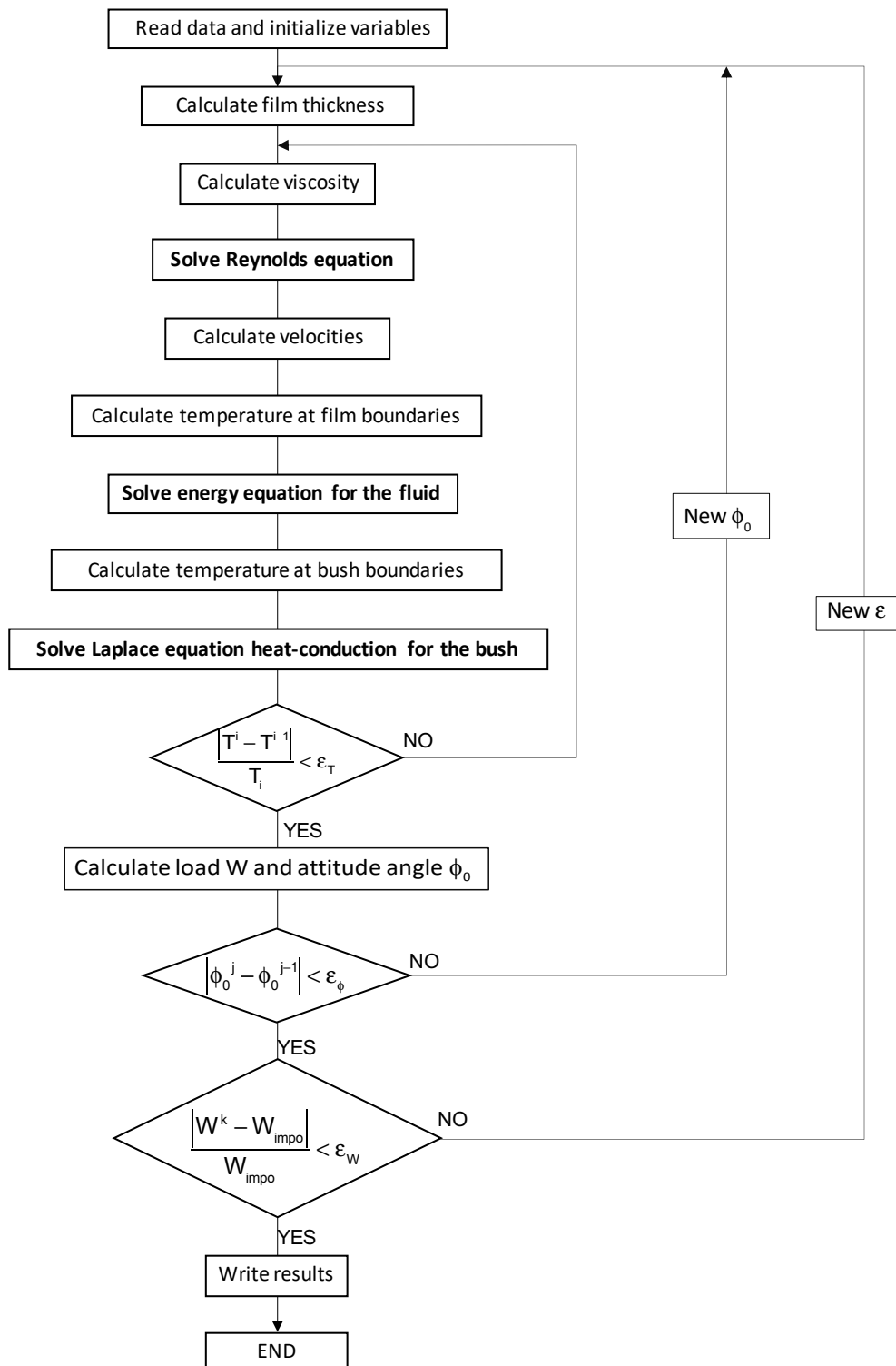


Figure 3.15. Flow chart of the numerical program.

3.4.2. Verifications

3.4.2.1. Study of several bearing global parameters

Isothermal simulations were performed to check and evaluate the evolution of global parameters of the bearing. In this section, it is considered that the bearing has no preload and no scratch on the journal. Bearing global parameters of the bearing such as the minimum film thickness, the maximum pressure, the volume flow rate, the flow balance, and the power loss, are studied.

Fig. 3.16 describes the evolution of the minimum film thickness, the maximum pressure, and the power loss as a function of eccentricity. At $\varepsilon = 0$, the minimum film thickness is equal to the bearing clearance and the maximum pressure is nil. Increasing the bearing eccentricity results in an increase in maximum pressure and a decrease in minimum film thickness. At $\varepsilon = 0.99$ the minimum film thickness is almost nil. The power loss in the bearing also increases with the increase of the eccentricity. The tendencies are all reasonable.

Fig. 3.17 shows results of lubricant flow rates as a function of eccentricity ratio ε . At $\varepsilon = 0$, the entering flow equals the exiting flow and there is no axial flow. Increasing the eccentricity ratio leads to a decrease in both enter and exit flow and an increase in the axial flow. It is predictable because the higher eccentricity reduces the minimum film thickness and increases the pressure gradients and flows in the fluid film.

These two simple verifications show that the evolution of the results of global bearing parameters is reasonable, and validates that the code is correctly programmed.

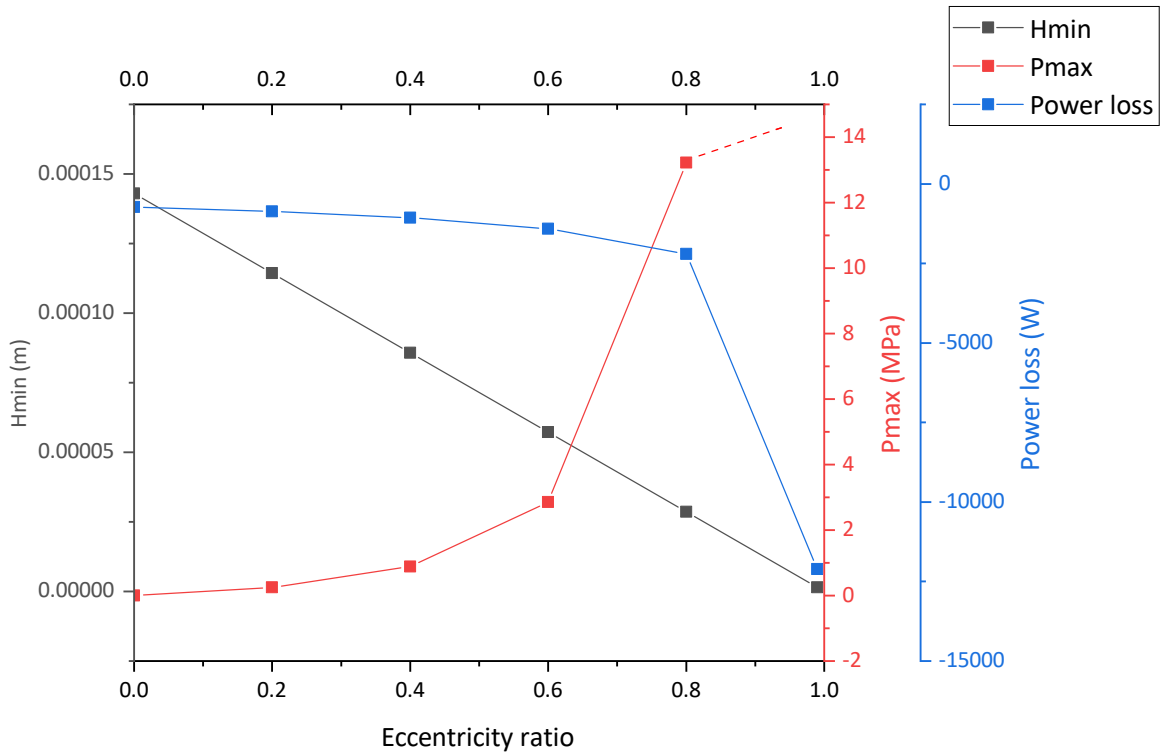


Figure 3.16. Hmin ,Pmax, and Power loss versus eccentricity.

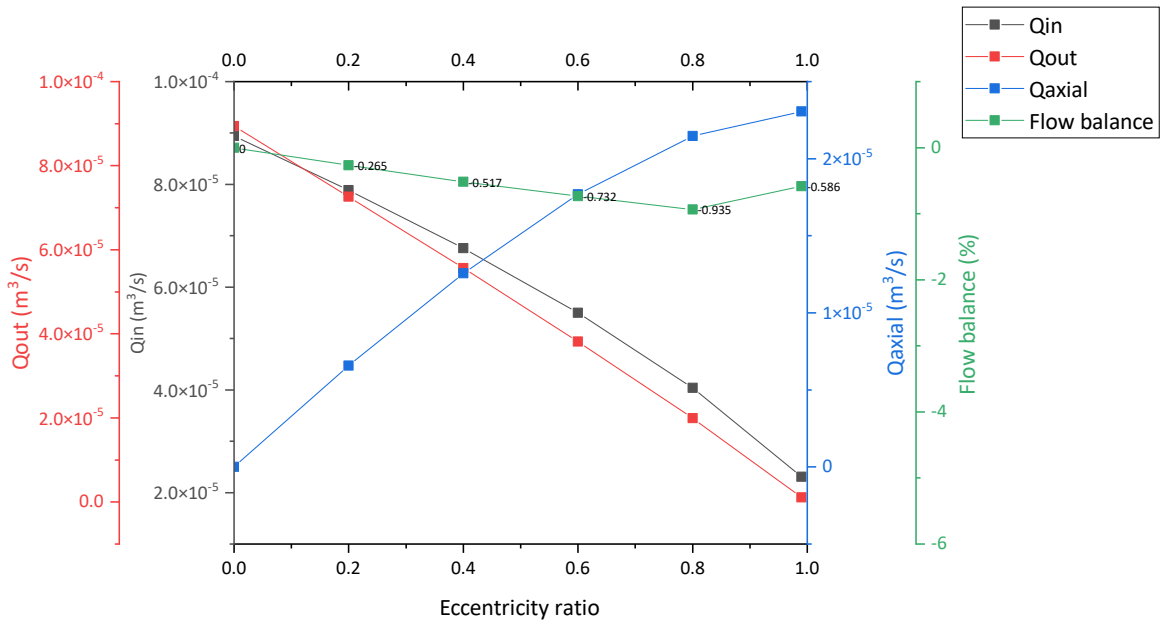


Figure 3.17. Volume flows and flow balance versus eccentricity.

3.4.2.2. Study of the imposed load, imposed position, and imposed eccentricity simulations

Another possible study to verify the code validity is to compare the results of a simulation with different sets of input. This study presents three types of simulation, named as: imposed load, imposed position, and imposed eccentricity:

- Imposed load W , find the bearing position, i.e., eccentricity and attitude angle
- Imposed eccentricity, find the bearing attitude angle and load capacity
- Imposed position, find load capacity W

The process of the comparison is described as the following steps:

- First, impose input values for the program to calculate the desired outputs
- Then, use the outputs obtained from the previous step as input values for the program to recalculate the imposed inputs.
- Compare the imposed inputs with the calculated to evaluate the code behaviors.

Simulations in isothermal models for a preload bearing are performed in two cases: a non- scratch bearing and a two-scratch bearing at axial positions $L/3$ and $2L/3$, scratch depth equal to radius clearance C .

Fig. 3.18 and Fig. 3.19. show the fluid film thickness and film pressure profiles, respectively, for the non- scratch bearing case. The imposed load is 6000 N, and the journal speed is 3500 rpm. Fig. 3.20 and Fig. 3.21 show the same parameters for the two-scratch bearing case.

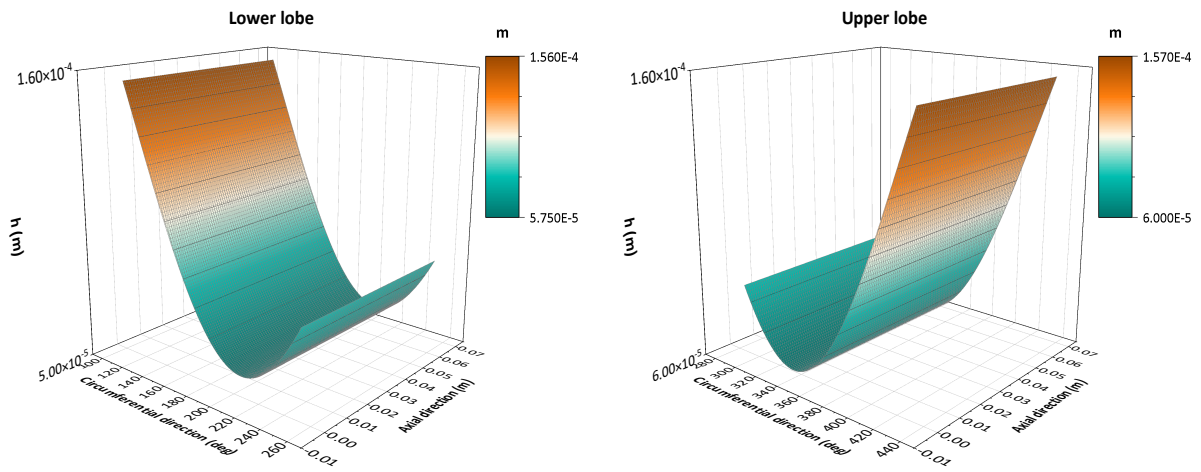


Figure 3.18. Lubricant film profile of a non-scratched bearing.

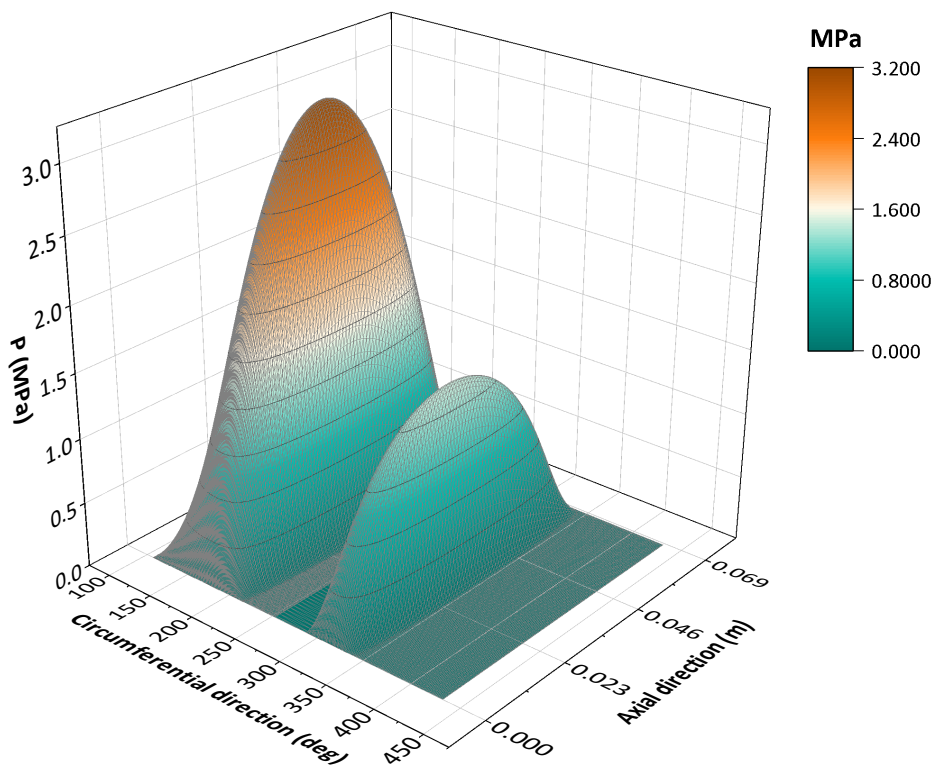


Figure 3.19. Pressure profile of a non-scratched bearing.

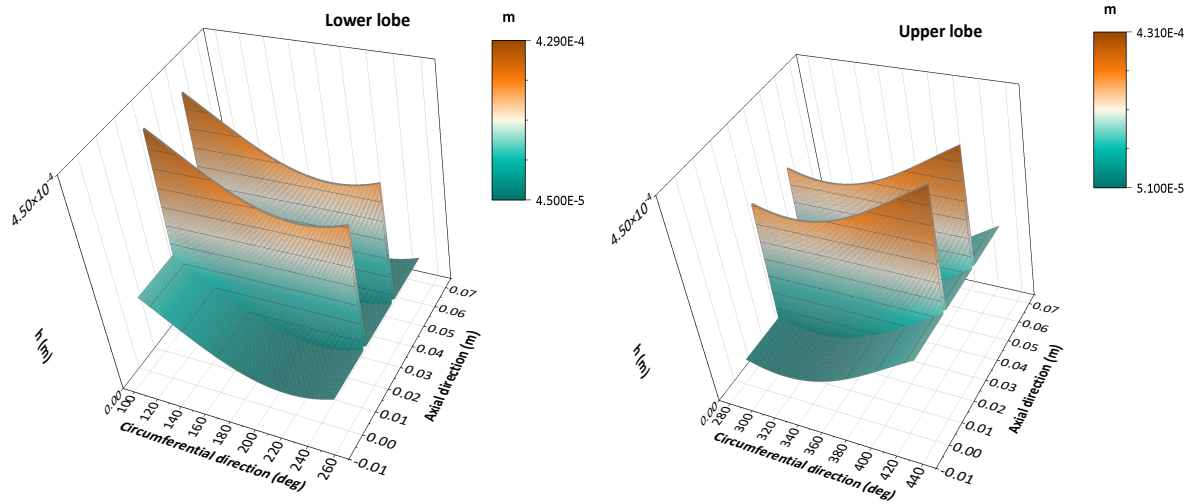


Figure 3.20. Lubricant film profile of a two-scratch bearing.

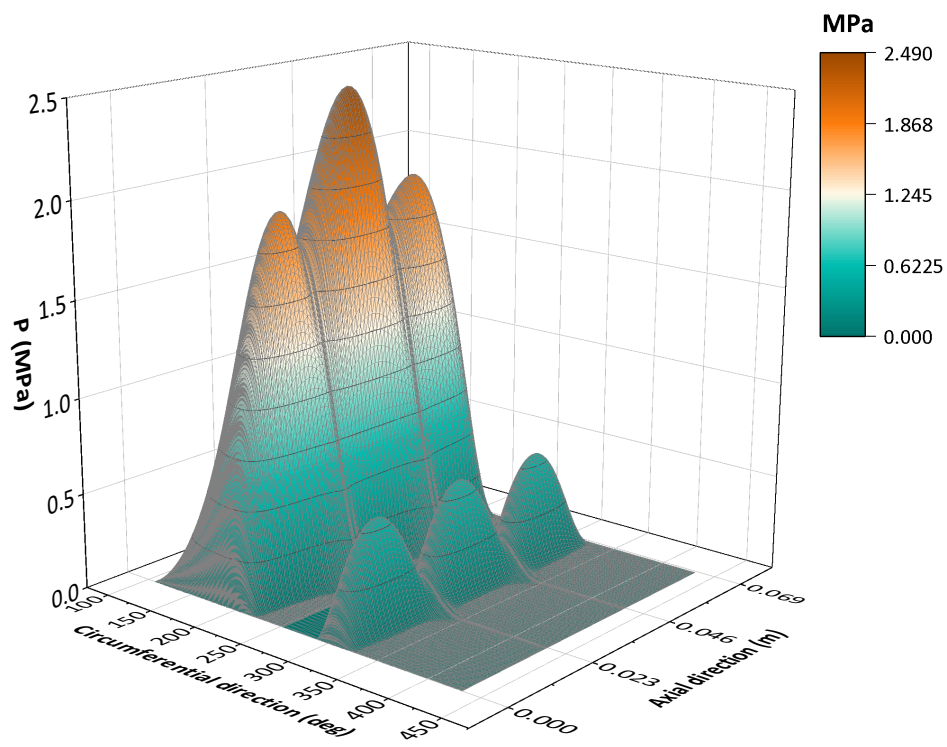


Figure 3.21. Pressure profile of a two-scratch bearing.

Table 3.6 shows results obtained when comparing and evaluating the imposed values and calculated values. It shows an expected outcome as the deviations between them are almost nil; it means that the program can simulate both non-scratch and scratch bearings correctly. However, it is noted that the accuracy of solutions has not been mentioned and validated with experimental data yet. It will be described in later chapters.

Table 3.6. Simulations with imposed applied load, imposed eccentricity, imposed position for non-scratch and scratch bearing.

Imposed Inputs			Calculated variables			Deviation	
			W (N)	e (μm)	ϕ_0 (o)	ΔW (%)	$\Delta\phi_0$ (%)
Non-scratch bearing							
W	6000	-	-	37.6621	87.942404	-	-
e	37.6621	-	5999.9403	-	87.942447	0.001%	0.000049%
ϕ_0, e	37.6621	87.9424	5999.9403	-	-	0.001%	-
Scratch bearing							
W	6000	-	-	46.3800	89.3474	-	-
e	4.64E-05	-	6001.7578	-	89.3475	0.029%	0.000162%
ϕ_0, e	4.64E-05	89.3474	5999.9989	-	-	0.000%	-

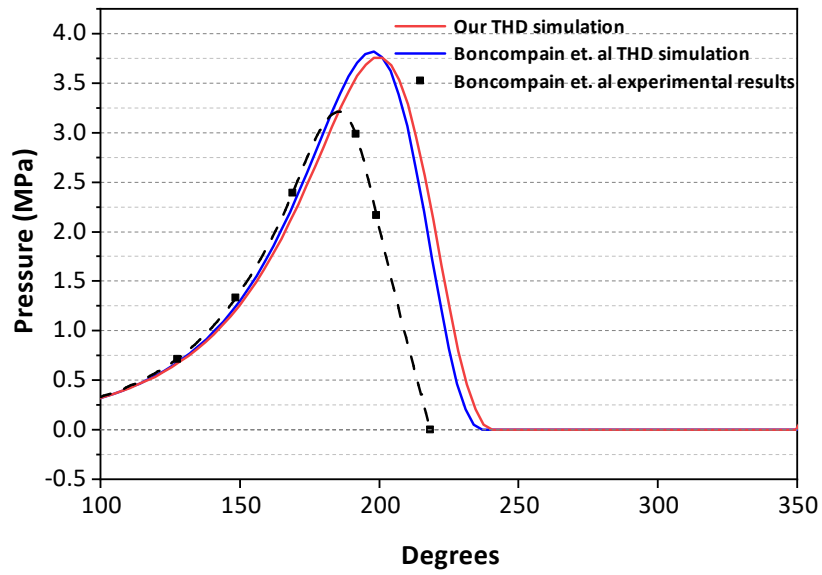
3.4.2.3. Comparison with literature results

A. Comparison with the results of R. Boncompain et al. (1986)

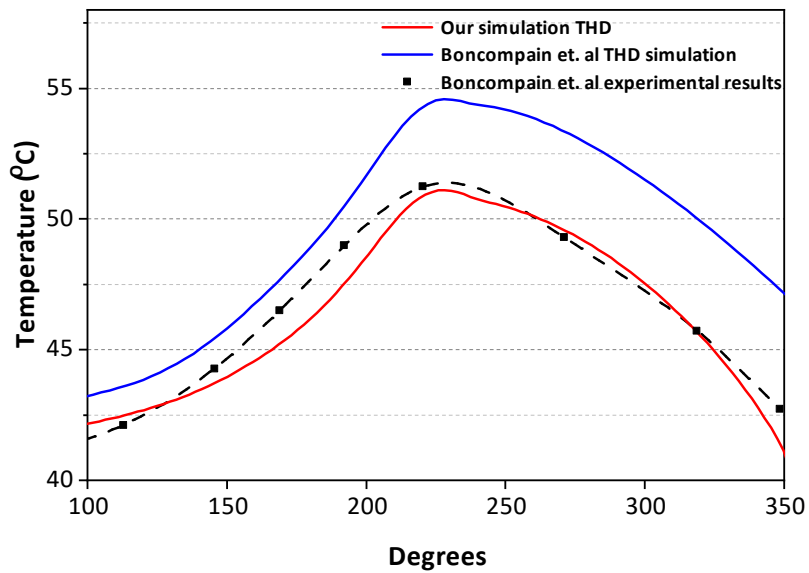
In this section, a verification with results obtained from the study of Boncompain et al. [67] is presented. A journal bearing with operating conditions listed in Table 3.7 is examined, simulations are in a thermohydrodynamic model.

Table 3.7. Simulation data for a plain journal bearing, no preload, and no scratch.

PARAMETERS		unit
Bearing dimensions		
Journal radius	50	mm
Radius bearing clearance	145	um
External bearing radius	100	mm
Bearing length	80	mm
Angular lobe length	342	deg
Lubricants		
Lubricant viscosity at 40 °C	0.028	Pa·s
Lubricant viscosity at 100 °C	0.0045	Pa·s
Lubricant density at 40 °C	860	kg/m ³
Lubricant specific heat	2000	J/kg·°C
Lubricant thermal conductivity	0.13	W/m·°C
Air thermal conductivity	0.025	W/m·°C
Solids		
Bush thermal conductivity	250	W/m·°C
Shaft thermal conductivity	50	W/m·°C
Convection heat transfer coefficient of the bush	50	W/m ² ·°C
Convection heat transfer coefficient of the groove	500	W/m ² ·°C
Convection heat transfer coefficient of the shaft	100	W/m ² ·°C
Operating conditions		
Feeding pressure	0.07	MPa
Supply lubricant temperature	40	°C
Ambient temperature	45	°C
Applied Load	10000	N
Shaft speed	2000	rpm



(a)



(b)

Figure 3.22. Verification for pressure and temperature profile in mid-plane with Boncompain et al. results.

Figure 3.22 shows comparisons of the fluid pressure and temperature in the mid-plane of inner bush surface with the results obtained by Boncompain et al. (both their THD simulation and the experimental results). The results show a good agreement between the two THD simulations for pressure (Fig.3.22a). The discrepancy in pressure gradient is minor, maximum

pressures are almost the same, only a minor difference in the locations of maximum pressures can be observed. For the temperature profiles, the discrepancies are higher, the difference in the full oil film being about 2 K and about 5 K in the cavitation zone (Fig.3.22b). Our simulation results are lower than Boncompain et al., who explained the minor discrepancy in the ruptured film zone by the fact that the deformations were not taken into account. It is noticed that our simulation is much closer to the experiments in the rupture zone, and that the differences in the active zone are less than 1 K. Overall, the results obtained are satisfying in terms of tendency and accuracy for both pressure and temperature.

B. Comparison with the results of J.W. Lund et al. (1984)

In this section, another verification with results obtained from the study of J.W. Lund et al. [68] is presented. A journal bearing with operating conditions listed in Table 3.8 is examined, simulations are in a thermal-hydrodynamic model.

Figure 3.23 shows comparisons of the fluid pressures in the mid-plane of internal bush surface with the results obtained by Lund et al. (both their THD simulation and the experimental results) with an applied load of 8,600 N and a rotational speed of 3,500 rpm. The results show a very good agreement among the THD simulations. The simulation results show minor discrepancies when compared to experimental data, again certainly because the thermal deformations of solid surrounding parts were not considered in these models.

Figure 3.24 compares the temperature profiles at film/bush interface in the bearing mid-plane. The results show a good agreement as well among the simulation in the full-film zone, but larger discrepancies in the film rupture zone. When compared to experimental data, large discrepancies were observed in the cavitation zone for all the simulations. Our simulation results in the film rupture zone fall between Lund et al. simulation results and experimental data, with a little closer to the experimental results compared to Lund et al. results.

In general, our simulation results are in good agreement with Lund et al. simulations and experimental data.

Table 3.8. Simulation data for a two-lobe journal bearing, no preload, and no scratch.

PARAMETERS		unit
Bearing dimensions		
Journal radius	50	mm
Radius bearing clearance	68.6	um
External bearing radius	100	mm
Bearing length	55	mm
Angular lobe length	160	deg
Lubricants		
Lubricant viscosity at 50 °C	0.018275	Pa·s
Lubricant viscosity at 90 °C	0.00561	Pa·s
Lubricant density at 40 °C	860	kg/m ³
Lubricant specific heat	2,000	J/kg ^o ·C
Lubricant thermal conductivity	0.15	W/m ^o ·C
Air thermal conductivity	0.025	W/m ^o ·C
Solids		
Bush thermal conductivity	50	W/m ^o ·C
Shaft thermal conductivity	50	W/m ^o ·C
Convection heat transfer coefficient of the bush	50	W/m ² ·C
Convection heat transfer coefficient of the groove	100	W/m ² ·C
Convection heat transfer coefficient of the shaft	50	W/m ² ·C
Operating conditions		
Feeding pressure	0.12-0.15	MPa
Supply lubricant temperature	50	°C
Ambient temperature	20	°C
Applied Load	5,600; 8,600	N
Shaft speed	3,500	rpm

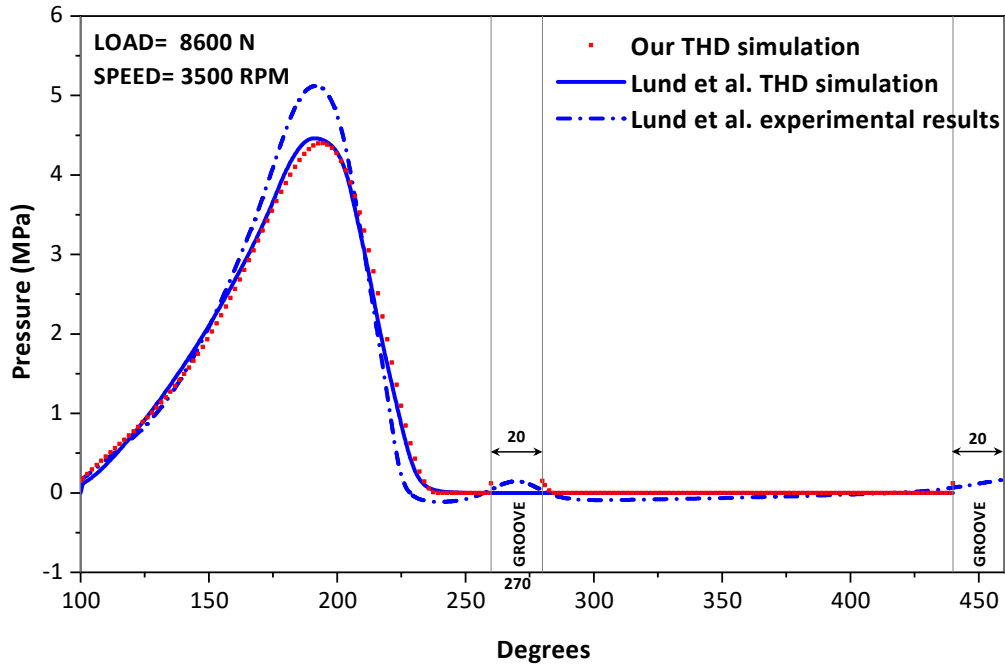


Figure 3.23. Verification for pressure profile at mid-plane with Lund et al. results.

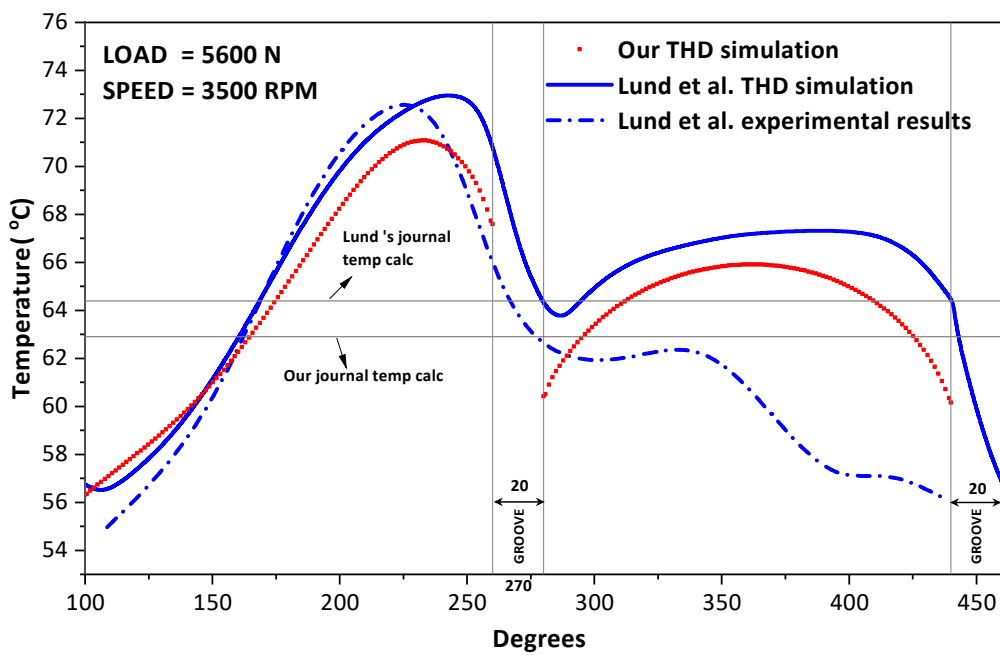


Figure 3.24. Verification for temperature profile at mid-plane with Lund et al. results.

3.5. Conclusions

This chapter described the discretization of the partial differential equations presented in chapter 2 by using the finite volume method, and the Stone's vectorized strongly implicit procedure to solve systems of equations. It also studied the geometry of a two-lobe journal bearing with scratches machined on the surface of the journal and meshing techniques for the fluid film. A Fortran program has been developed and verified by comparing with studies from the literature, to find a full thermal-hydrodynamic solution for multi-lobe journal bearings lubricated with an incompressible fluid. Next chapter will show several numerical results and discussions for the scratched journal bearings.

Chapter 4. Validation

In this chapter, validations of numerical results are performed by comparing with experimental data. Validation is performed for a variety of bearing operating conditions, i.e. the rotational speed and applied load. The results will be presented for bearing configurations with either one or two scratches. The depth of scratches is varied as a function of the bearing clearance C ; the width is kept constant at 2 mm. The bearing geometry and lubricant characteristics were presented in chapter 3.

4.1. Presentation of experiment-setup and validation data

In this study, for the validation we used experimental data collected by Yann Alexandre [55]. The experiments were carried out using the journal bearing test rig at the Pprime Institute. This test rig has been used successfully for numerous experiments for journal bearings over the past forty years. Figure 4.1 shows a schematic view of the test-rig, and Figure 4.2 presents locations of probes at the inner surface of the bush and positions of the circumferential scratches in the axial direction.

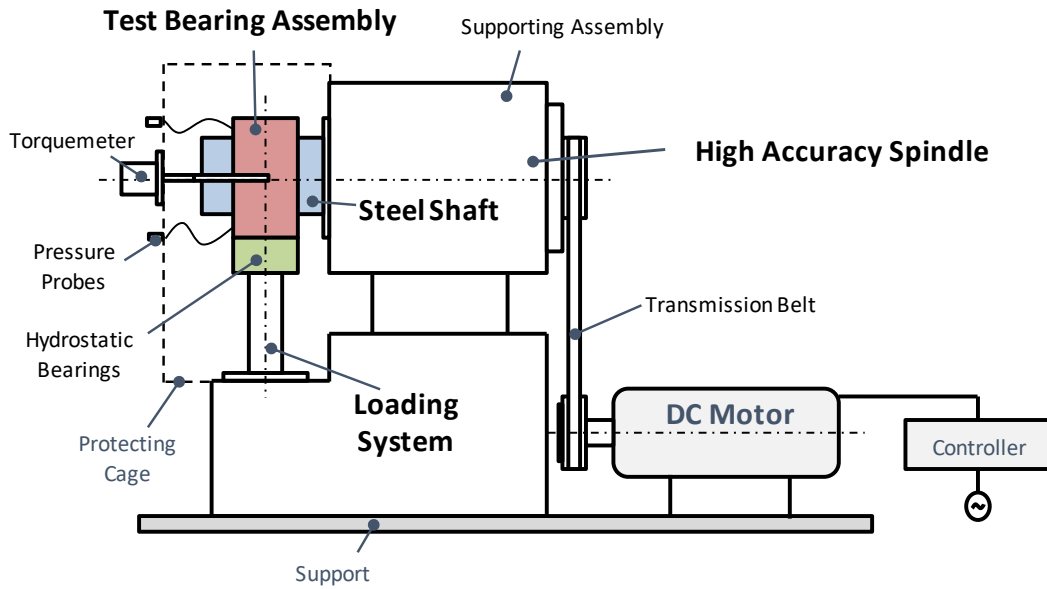


Figure 4.1. Schematic view of the test rig [69].

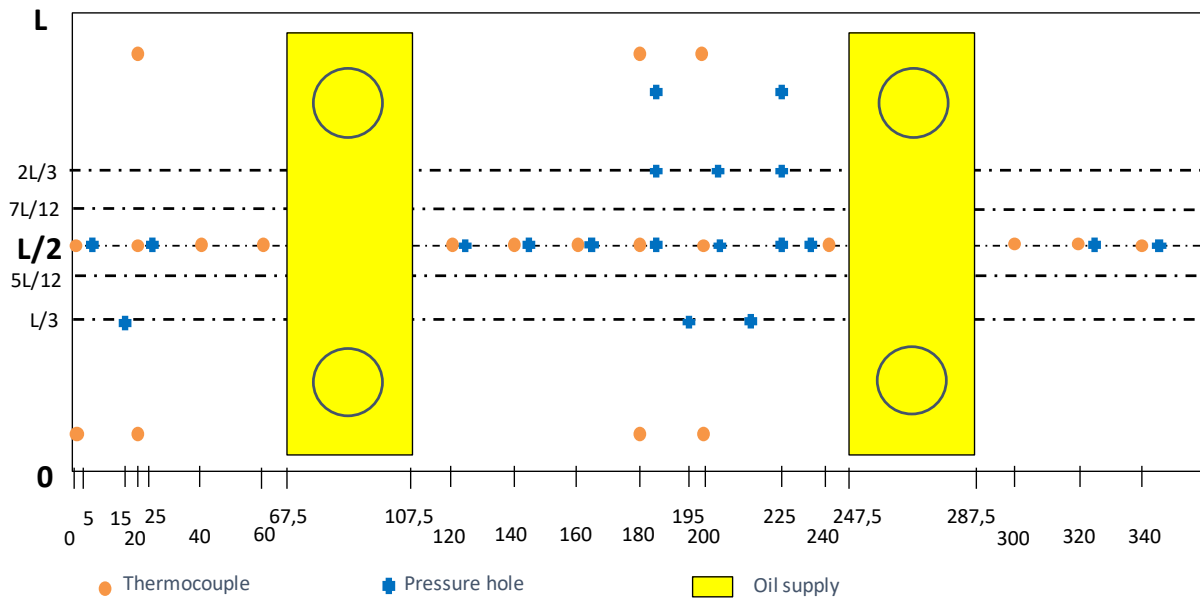


Figure 4.2. Locations of probes at inner surface of the bush and positions of scratches [69].

Table 4.1. Cases of validation.

No. of scratch		Case	Depth (μm)	Relative position	Load (N)	Speed (rpm)
1	1	Multiple depths	0, 90, 135, 214, 260	L/2	6,000	3,500
	2	Multiple loads	90	L/2	6,000; 7,000; 8,000; 9,000; 10,000	3,500
	3	Multiple speeds	90	L/2	6,000	2,000; 2,750; 3,500
2	1	Average scratch	116	L/3, 2L/3	6,000	3,500
	2	Deep scratch	255	5L/12, 7L/12	6,000	3,500

Table 4.1 shows validation cases for the studied journal bearing, with either one or two scratches. For the one-scratch bearing configuration, several numerical simulations have been performed by varying successively the scratch depth, the applied load and the rotational speed. For the two-scratches configuration, the rotational speed and the applied load remain constant and two values of the scratch depth and of the relative scratch location are analysed. This wide range of simulations allows not only to validate the model but also to evaluate the possibility of any limitations of the studied model.

4.2. Validation for bearings with one scratch

4.2.1. Validation cases with different scratch depths

In this section, several cases of validation with different scratch depths are presented. For all the validation cases in this subsection, the scratch is at L/2 and has a width of 2 mm; the

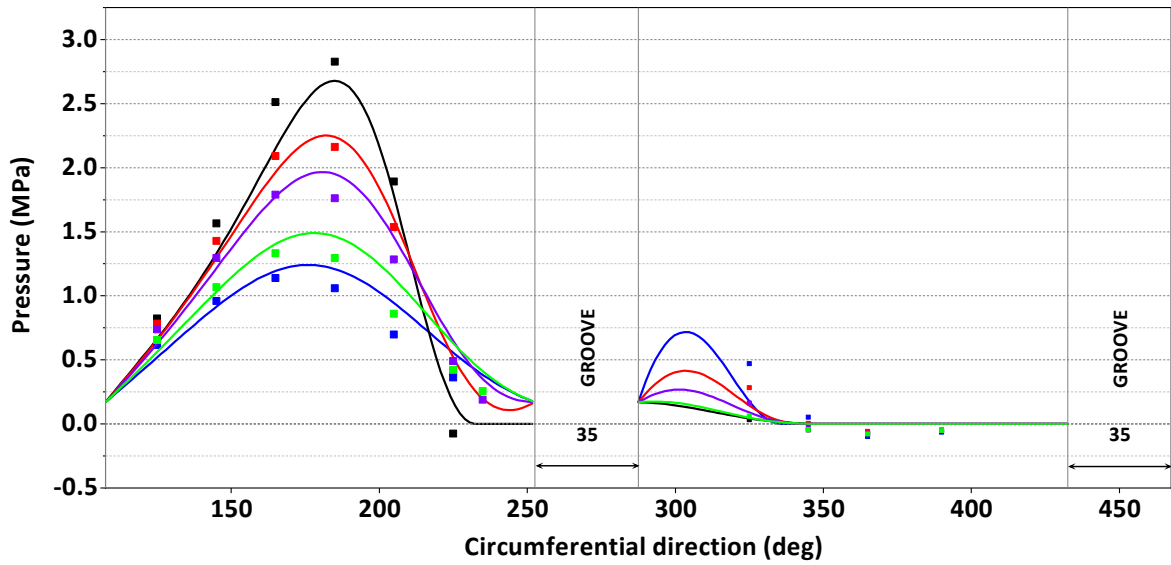
bearing operating conditions are kept unchanged with an applied load of 6,000 N and a rotational speed of 3,500 rpm. The depth of the scratch is varied with five values at 0 μm (no scratch), 90, 135, 241, and 260 μm . Validation results are presented in Figure 4.3 and Figure 4.4 for pressure and temperature profiles, respectively.

Figure 4.3 shows comparisons between simulation and experimental results for the pressure profiles in the bearing mid-plane (Fig. 4.3a) and in axial direction (Fig. 4.3b). It can be seen in Fig. 4.3a that the agreement in circumferential pressures in the bearing mid-plane is very good in terms of shape and value with the differences are about from 3 to 7%. The differences between calculated and measured values seem not to depend on the depth of the scratch as the differences are consistent for every value of the scratch depth. Besides this, the maximum pressures are at the same location, and the location of ruptured film positions are almost the same as well. The axial pressure profiles at two angular positions at 185° and 225° also shows very good agreements in both distribution shapes and values (Fig. 4.3b). The differences in values are in the same order with the circumferential pressures at from 3 to 7%. It can be observed that pressure distributions in both circumferential and axial directions are changed by the presence of the scratch, and more significantly in the scratch regions. The maximum pressure in the bearing mid-plane dropped about 25% (from 2.7 to 2 MPa) with the scratch depth 135 μm (about 0.9C), and more than 50% (from 2.7 to 1.25 MPa) with the scratch depth of 260 μm (about 1.8C). In the axial direction, the pressure profiles are modified lightly with the depth smaller than 1C, but more significantly when the depth is larger than 1C.

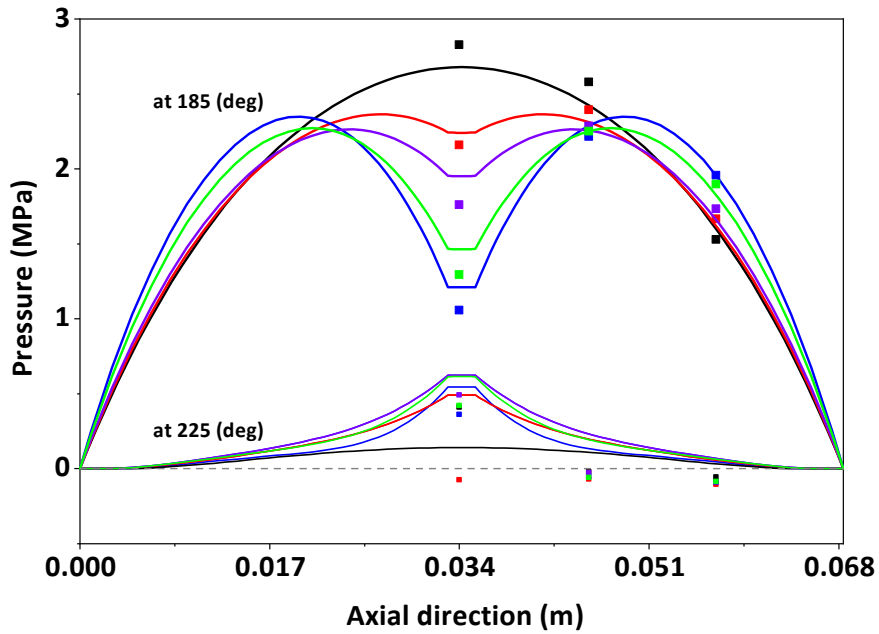
1 scratch: [2 mm, L/2]

SPEED=3,500 RPM; LOAD 6,000 N

- Experiment, no scratch — THD simulation, no scratch
- Experiment, Depth 90 μm — THD simulation, Depth 90 μm
- Experiment, Depth 135 μm — THD simulation, Depth 135 μm
- Experiment, Depth 214 μm — THD simulation, Depth 214 μm
- Experiment, Depth 260 μm — THD simulation, Depth 260 μm



(a)

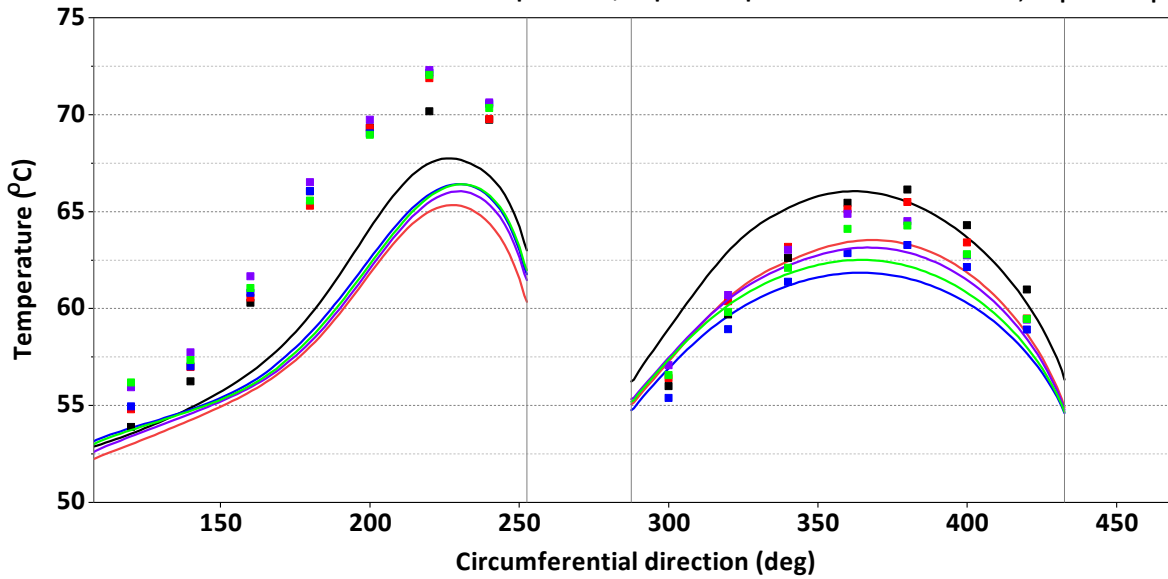


(b)

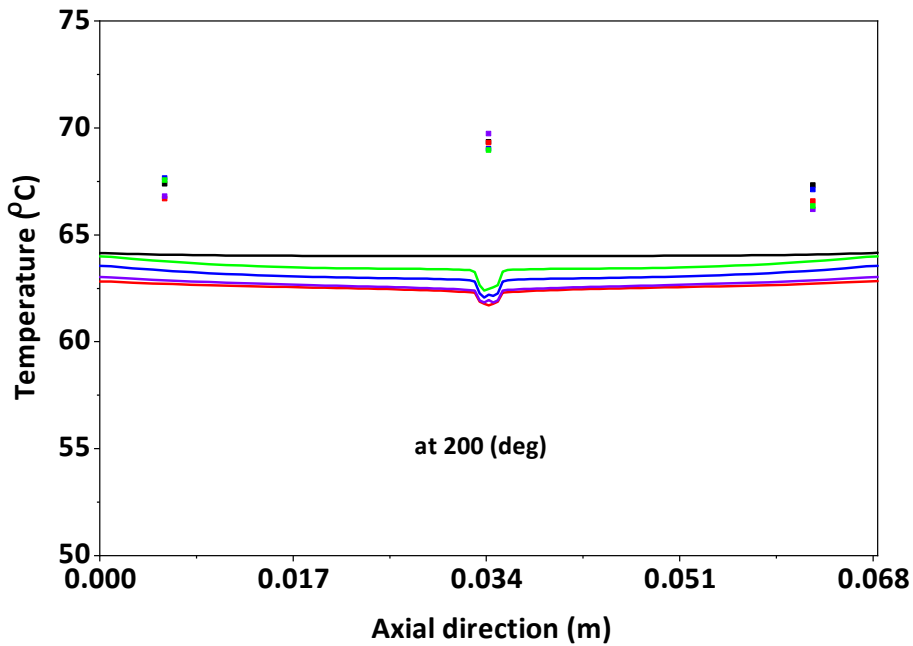
Figure 4.3. Comparison of pressure profiles for different scratch depths: (a) Circumferential direction, in bearing mid-plane, (b) Axial direction at angles 185° and 225°. Depth: 0, 90, 135, 214, 260 μm.

1 scratch: [2 mm, L/2]
 SPEED=3,500 RPM; LOAD 6,000 N
 Scratch depth: 0, 90, 135, 214, 260 μm

■ Experiment, no scratch	— THD simulation, no scratch
■ Experiment, Depth 90 μm	— THD simulation, Depth 90 μm
■ Experiment, Depth 135 μm	— THD simulation, Depth 135 μm
■ Experiment, Depth 214 μm	— THD simulation, Depth 214 μm
■ Experiment, Depth 260 μm	— THD simulation, Depth 260 μm



(a)



(b)

Figure 4.4. Comparison of temperature profiles for multiple cases with different scratch depths: (a) Circumferential direction, in bearing mid-plane, (b) Axial direction at angles 200°. Depth: 0, 90, 135, 214, 260 μm .

Figure 4.4 compares the temperature profiles at the film/bush interface, in the bearing mid-plane. Good agreements are found the low loaded lobe for every validation case when the calculated temperature curves show good matches to the measured data (Fig. 4.4a), the differences are about 1-3 K. However, small discrepancies are found in the high loaded lobe, with the differences of about 2-7 K (Fig. 4.4a) in both circumferential direction and in the axial direction at an angular angle of 200° (Fig. 4.4b).

There are several possible explanations for these results. One possible is that the model does not take into account the mechanical and thermal deformations, which have a strong influence in the bearing performance and the deformations produce more intensive effects on the high loaded lobe than on the unloaded load [70–72]. Another possible reason is the boundary condition at the outer surface of the lobes. The entire outer surface of the low loaded lobe has no direct contact with other surfaces and the thermal boundary in this zone is a heat convection to the ambient medium. On the other hand, the high loaded lobe has a direct contact with the housing support in a portion (about 40%, for an angular coordinate between 150° and 210°) of the outer surface of this lobe; in this region, the outer surface of the bearing support is one of the components of the hydrostatic bearing employed for applying the external radial load to the bearing. The heat exchange in this zone should thus be treated differently, as shown by Kucinski et al. in [73]. However, it is difficult to model completely the heat exchange between the bearing and the supporting system. It is unfortunately not yet included in our current model. It is also noted the temperature agreement in the case of no scratch is better compared to cases with scratch, with the differences in the high loaded lobe is about 1-4 K (versus 2-7 K). It is possible that the presence of the scratch may have led to changes in fluid velocity profiles which corresponding to changes in thermal effects. This problem will be studied in more details in the next chapter.

Although the agreement is not ideal in point-to-point basic, the distribution shape and tendency are satisfactory. It can be seen from Fig. 4.4 that increasing the scratch depth only changes slightly the temperature profiles, temperatures increased 1-2 K in the high loaded lobe but decreased 1-2 K in the low loaded lobe. The trends are in agreements with the experimental data.

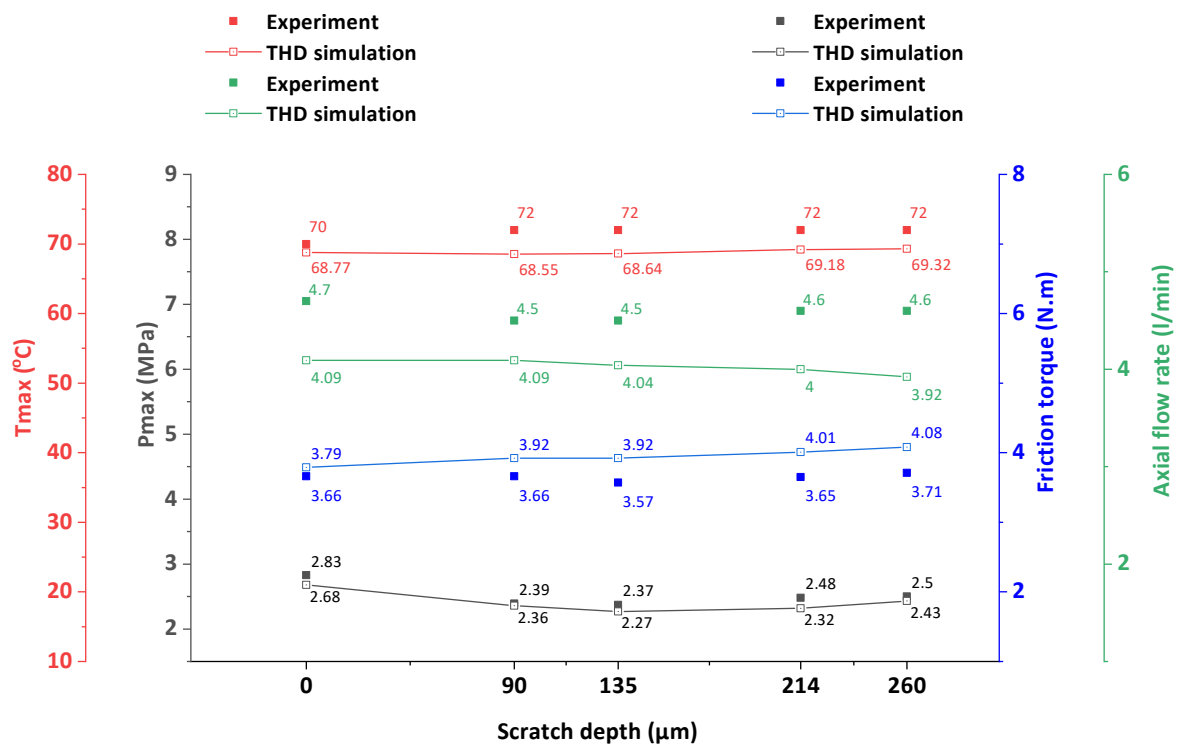


Figure 4.5. Comparison of bearing global performance parameters: maximum pressure, maximum temperature, friction torque, and axial flow rate for different scratch depths.

Figure 4.5 compares simulation and measured data for four crucial performance parameters of the bearing, including the maximum pressure, maximum temperature, friction torque, and axial flow rate for all the validation cases with different depths. Overall, good agreements are observed for all the parameters. Differences in maximum pressures are about 0.067 to 0.148 MPa (1-7%), in maximum temperatures are about 1.4-3.7 K (2-5%), and larger in the friction torques and axial flow rates, at about 0.132-0.368 N·m (4-9 %) and 0.57-0.63

l/min (10-15%), respectively. Calculated axial flow rates are lower than the measured values, it can be explained by the fact that the axial leakage flow rates in the groove regions were neglected in the model. The differences seem not to depend on the depth of scratch. Although the presence of the scratch significantly modified the pressure profile, maximum pressures are not changed significantly. However, it is noted that applied load in the case is not high, it can be different for cases of higher loads.

In summary, this sub-section has validated the current THD model for a journal bearing with three different cases of scratch depth (non-scratch, shallow, average, and deep). The bearing is operated at a high speed of 3,500 rpm (to observe high thermal effects), an average applied load of 6,000 N. Other parameters were kept unchanged for the simulations. The comparison results obtained shows:

- Very good agreement in pressure distribution in both of tendency and values.
- Very good agreement in temperature distribution for the low loaded lobe in both of tendency and values.
- Fair agreement in temperature distribution for the high loaded lobe: good agreement in tendency and lower temperature in term point-to point basic.
- Good agreements in global parameters of bearing performance.
- The existence of scratch changes both pressure and temperature distributions. The influence of the scratch is more significant on pressures but slighter in temperatures.
- Comparison results obtained are very consistent and do not depend on the depth of the scratch. Next sub-sections will validate the model with other configurations of bearing operating conditions.

4.2.2. Validation cases with different applied loads

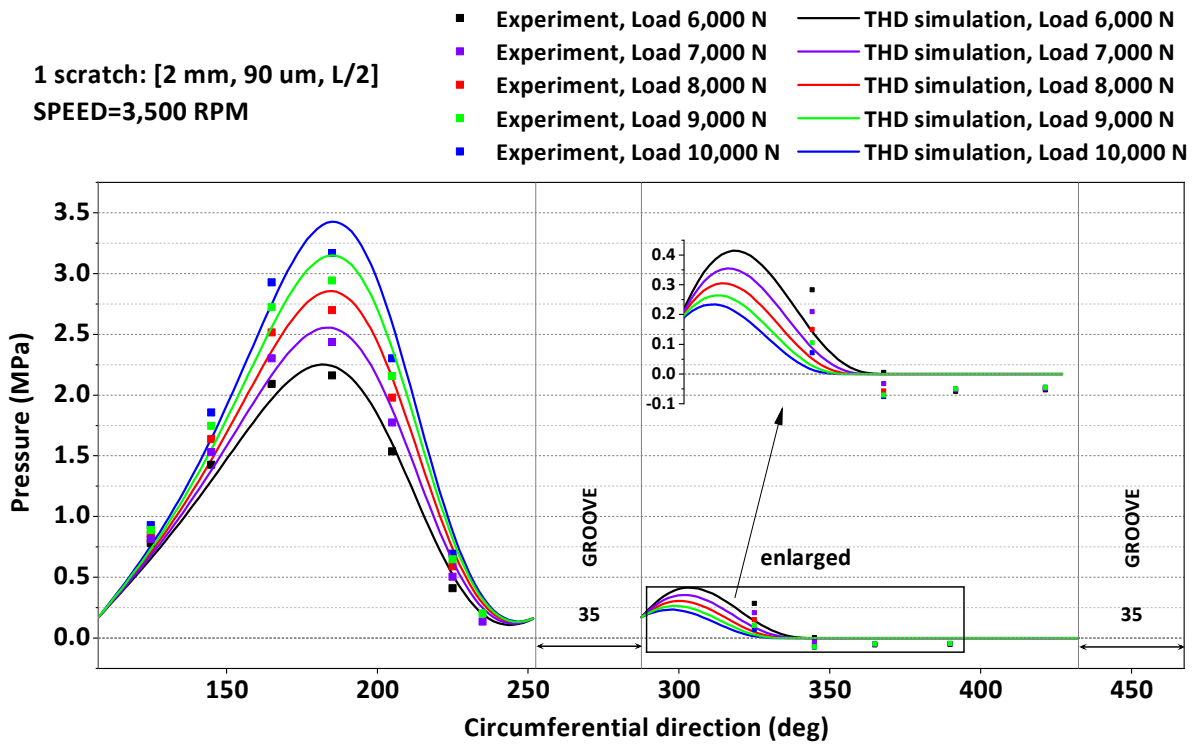
In this section, several cases of validation are presented, in which the applied load is varied from average to high values. For all the validation cases in this subsection, the scratch is at $L/2$ and has a width of 2 mm; a depth of 90 μm ; the rotational speed is 3,500 rpm. The applied load is varied, with five values at 6,000; 7,000; 8,000; 9,000; and 10,000 N. Validation results are presented in Figure 4.6 and 4.7 for pressure and temperature profiles, respectively.

Figure 4.6 shows comparisons between simulation and experimental results for the pressure profiles in the bearing mid-plane (Fig. 4.6a) and in axial direction (Fig. 4.6b). From Fig. 4.6a we can see that the agreements in circumferential pressures in the bearing mid-plane are very good in terms of shape and value with the maximum differences are about 3-5% and the differences are almost the same for all the cases with different loads. Similar tendencies are observed for the axial pressure profiles at two angles 185° and 225° (Fig. 4.6b). These results indicate that the model is able to simulate pressure distribution with a high consistency for various applied loads.

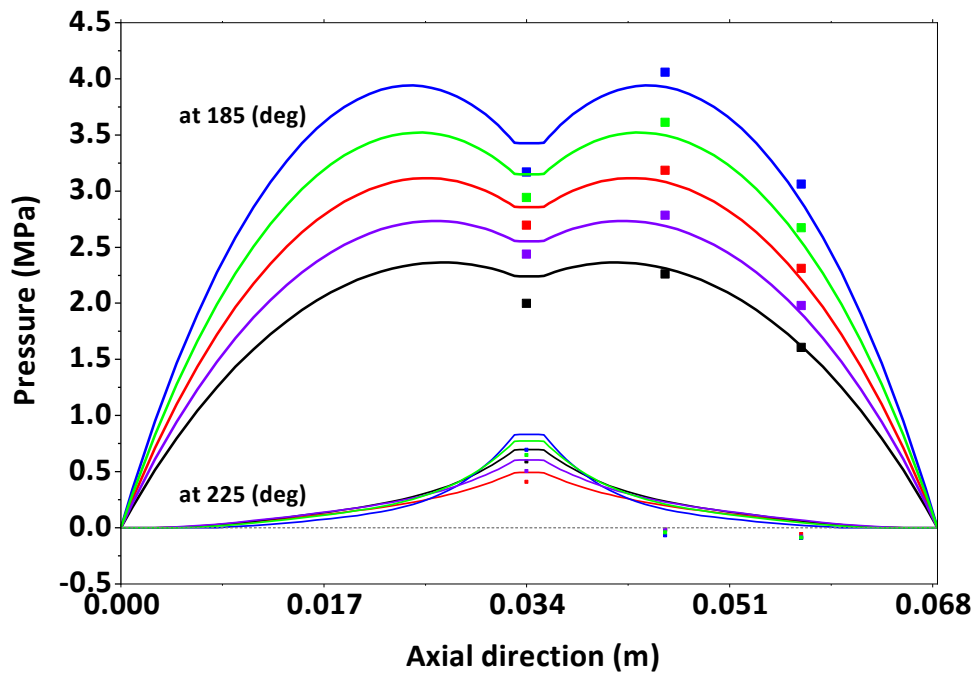
It can be seen on Fig. 4.6a that the pressures in the bearing mid-plane increased with the increases of the applied, but it is difficult to observe the influence of the scratch on the change of loads in this figure. It is however more visibly observed from Fig. 4.6b. For the case of a lower load at 6,000 N, the axial pressure is changed slightly only. The magnitude of the modification is increasing with the increases of the applied load and we can see the modification with the case of 10,000 N is more significant. These results indicate that the influence of the scratch on the pressure is different with different applied loads. The influence is more significant for higher applied loads.

Figure 4.7 compares the temperature profiles at the film/bush interface, in the bearing mid-plane and axial direction. Good agreements again are found the low loaded lobe for all the validation case when the calculated temperature curves matched to the measured data (Fig. 4.7a), the differences range from 1 to 3 K. However, minor discrepancies are found in the loaded lobe, with larger differences of about 2-7 K (Fig. 4.7a) in both circumferential direction and in the axial direction at an angular angle of 200° (Fig. 4.7b). The temperature increased slightly with the increases of the applied load and this tendency is observed with measured data.

To sum up, the validations show a high consistency of simulation results for a variety of different applied loads.



(a)



(b)

Figure 4.6. Comparison of pressure profiles for different applied loads: (a) Circumferential direction, in bearing mid-plane, (b) Axial direction at angles 185° and 225°. Load: 6,000; 7,000; 8,000; 9,000; 10,000 N.

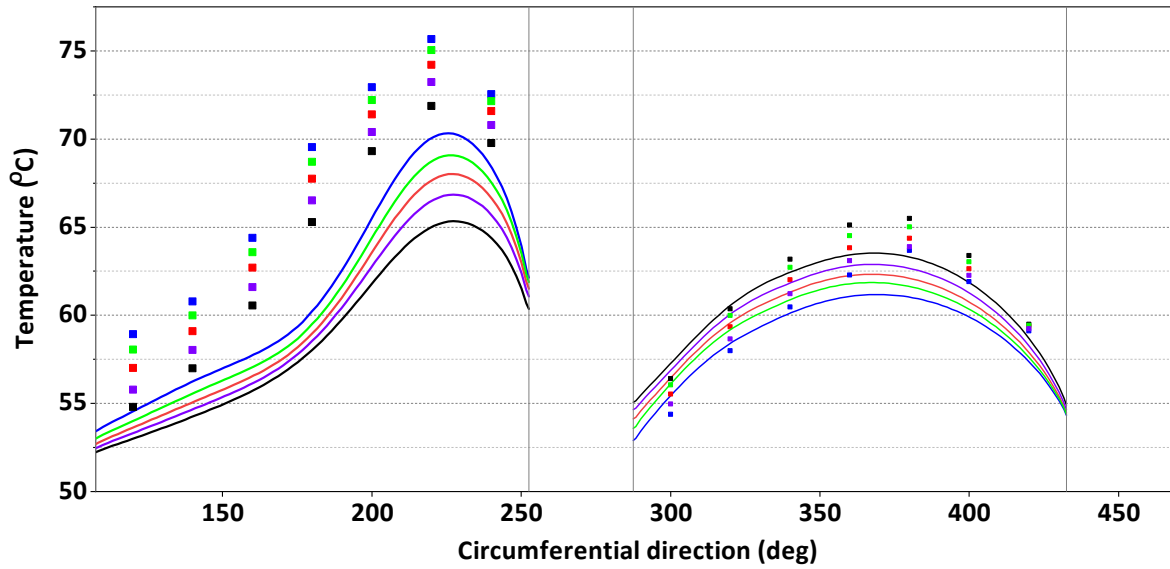
1 scratch: [2 mm, 90 μ m, L/2]

SPEED=3,500 RPM

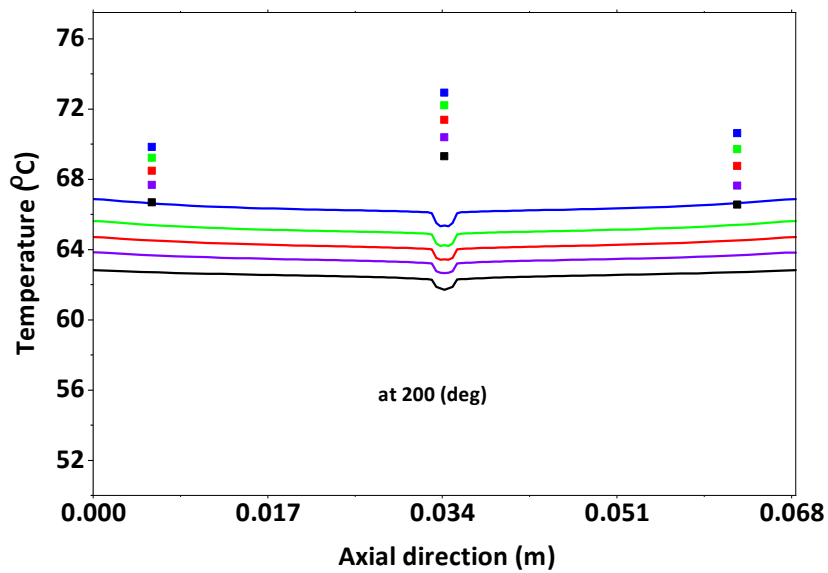
LOAD:

6,000; 7,000; 8,000; 9,000; 10,000 N

- Experiment, Load 6,000 N
- Experiment, Load 7,000 N
- Experiment, Load 8,000 N
- Experiment, Load 9,000 N
- Experiment, Load 10,000 N
- THD simulation, Load 6,000 N
- THD simulation, Load 7,000 N
- THD simulation, Load 8,000 N
- THD simulation, Load 9,000 N
- THD simulation, Load 10,000 N



(a)



(b)

Figure 4.7. Comparison of temperature profiles for different applied loads: (a) Circumferential direction, in bearing mid-plane, (b) Axial direction at angles 200°. Load: 6,000; 7,000; 8,000; 9,000; 10,000 N.

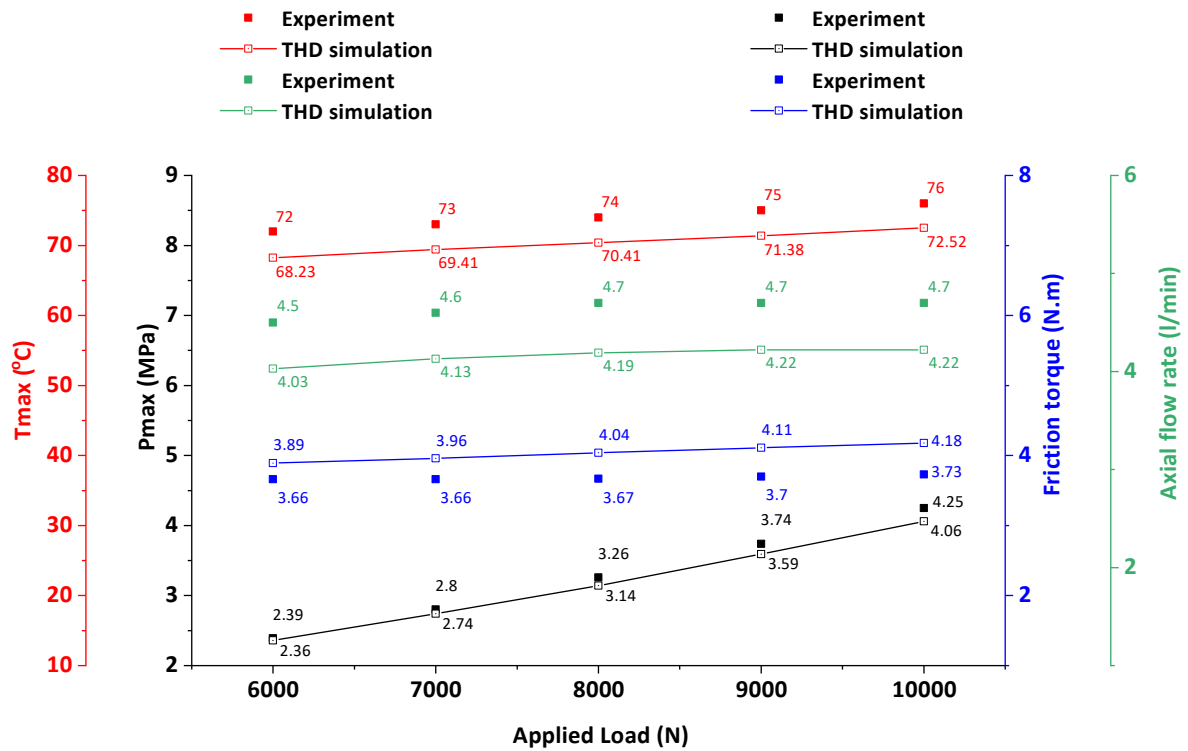


Figure 4.8. Comparison of bearing global performance parameters: maximum pressure, maximum temperature, friction torque, and axial flow rate for different loads.

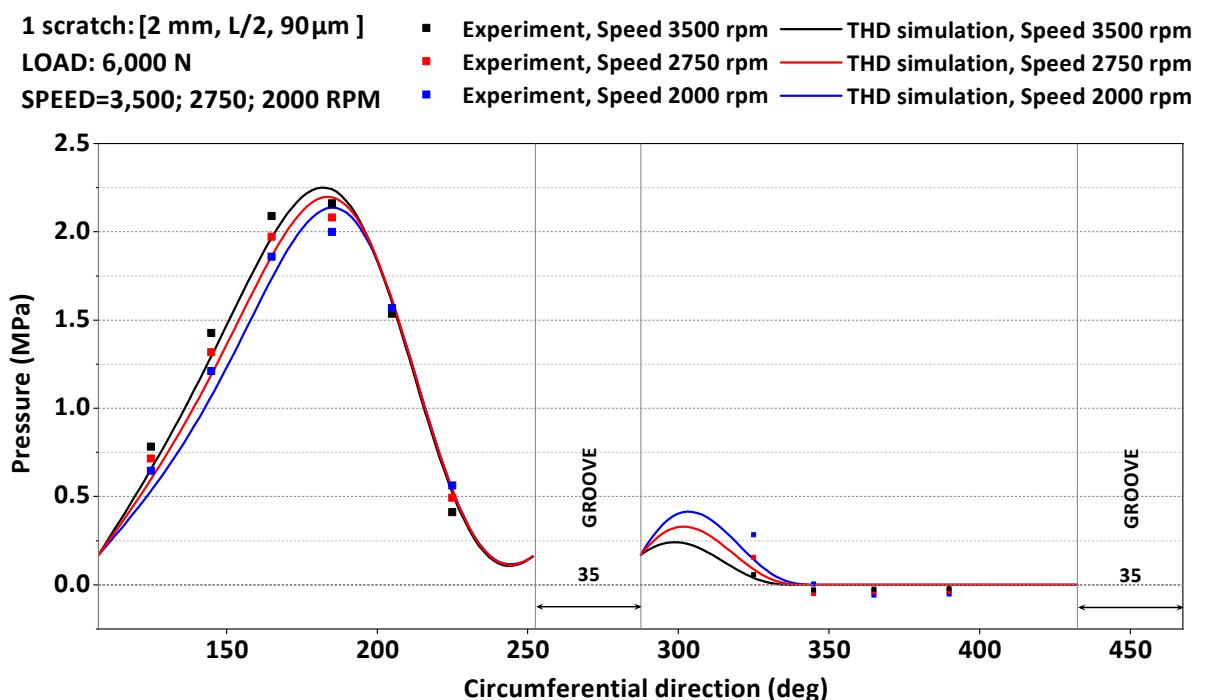
Figure 4.8 compares simulation and measured data for the global performance parameters of the bearing for the validation cases. These results show good agreements for all the parameters in both tendencies and values. The difference in maximum pressures, on average, is about 3%, in the maximum temperatures is 5%, in friction torques and axial flow rates are 9% and 11%, respectively. Increasing the applied load (from 6,000 to 10,000 N) does not change the differences in maximum temperatures and axial flow rates; however, it increased slightly the differences in maximum pressures and friction torques from 1 to 5% and 6 to 12%, respectively.

4.2.3. Validation cases with different different rotational speeds

This section presents several cases of validation, in which the rotational speed is varied. For all the validation cases in this subsection, the scratch is at $L/2$ and has a width of 2 mm; a depth of $90\ \mu\text{m}$; the applied load is 6,000 N. The speed is varied with three values at 2,000; 2,750; and 3,500 rpm. Validation results are presented in Figure 4.9 and 4.10 for pressure and temperature profiles, respectively.

Figure 4.9 compares simulation and experimental results for the pressure profiles in the bearing mid-plane (Fig. 4.9a) and in axial direction (Fig. 4.9b). It shows very good agreements in both circumferential and axial pressure profiles, as it was observed in the previous validation cases with different scratch depths or loads. These results prove that the model is able to simulate pressure distributions with a high consistency for a variety of speeds.

As shown in Figure 4.9 that the pressure distribution only modified slightly with different speeds. The influence of the scratch on the pressure distribution barely depends on the speed.



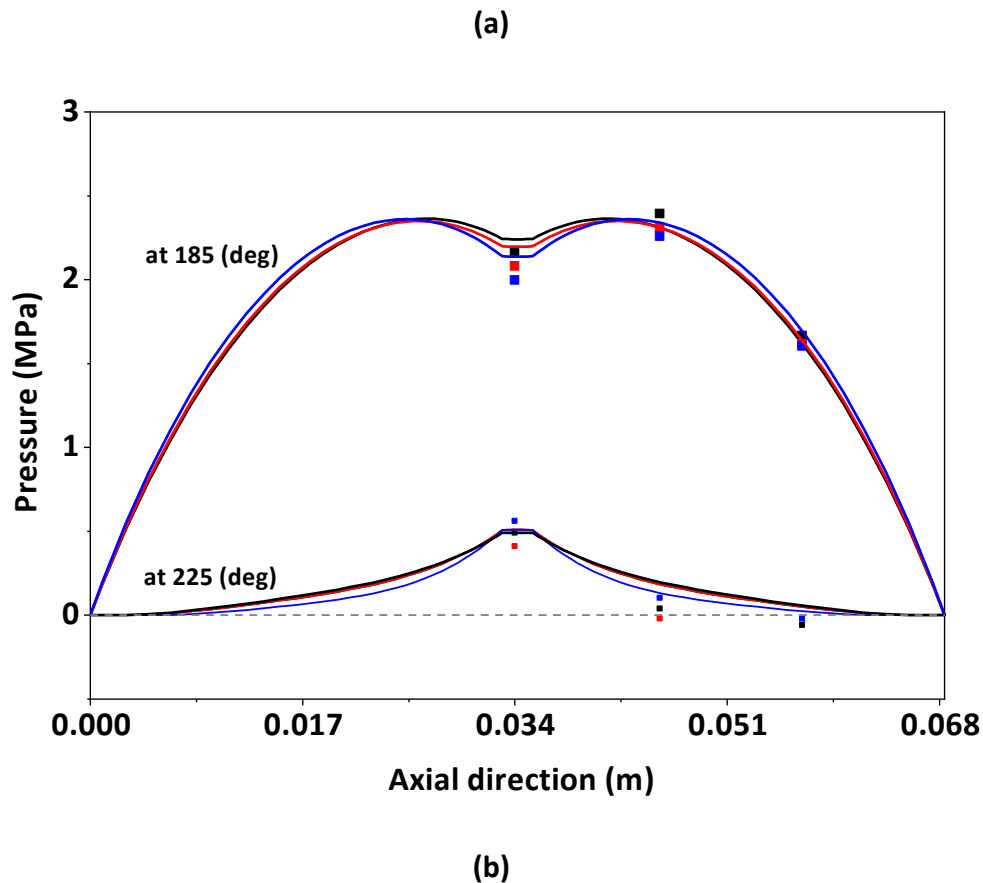


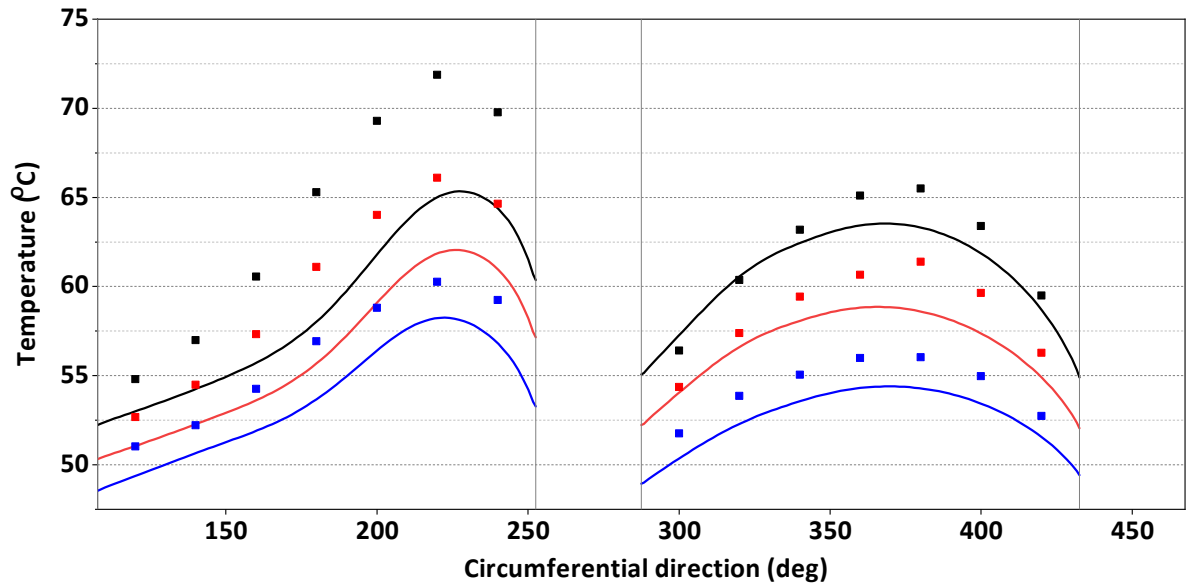
Figure 4.9. Comparison of pressure profiles for different rotational speeds: (a) Circumferential direction, in bearing mid-plane, (b) Axial direction at angles 185° and 225°. Speed: 2,000; 2750, 3500 rpm.

Regarding temperature comparisons shown in Figure 4.10, good agreements again are found the low loaded lobe for all the validation cases (Fig. 4.10a), the differences range from 1 to 3 K. However, it is found that in the high loaded lobe the temperature differences seem to vary corresponding to the speed. The discrepancies are larger with higher speeds. For example, with the case of low speed at 2,000 rpm, the maximum temperature difference is about 4 K, while they are about 5 K and 7 K for the cases of speeds at 2,750 and 3,500 rpm, respectively. The same trend can also be observed clearly in the axial temperatures at the angle of 200° (Fig.4.10b). It seems that the model predicts more precise the temperature distribution for cases of lower speeds and less precise for the higher speed cases, which usually

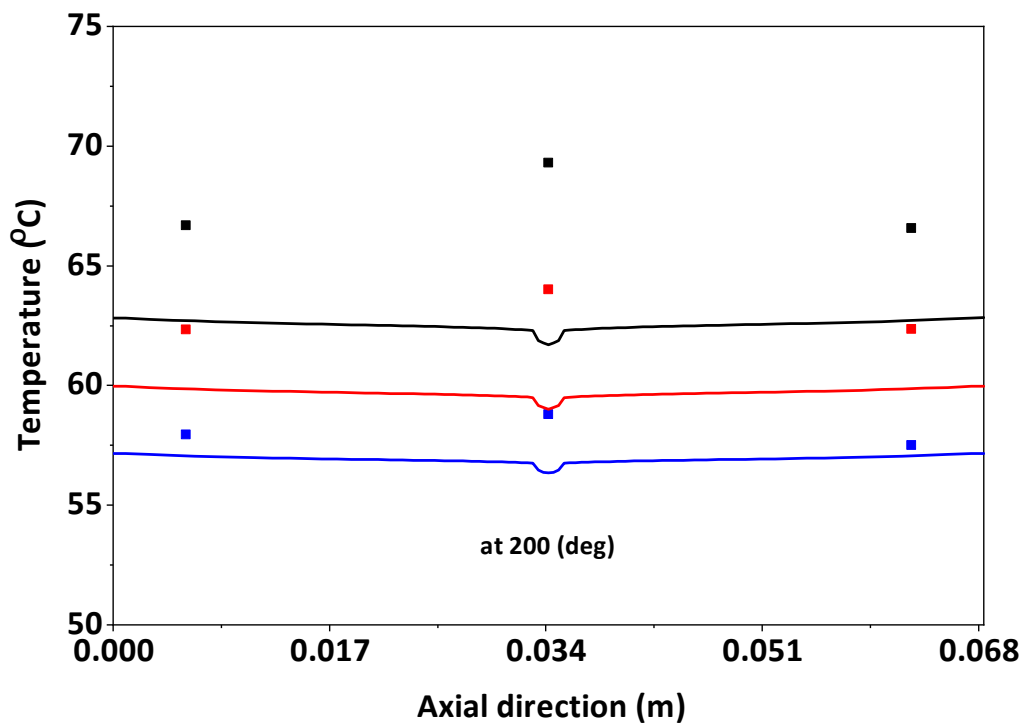
related to higher thermal effects. These results are not expected and the reasons for them are not yet entirely understood. It is probable that the presence of the scratch changes the velocity profiles, which may lead to changes in certain parameters, but the current model does not yet take them into account. More details on this problem will be studied and discussed in the next chapter where velocities in the scratch region are analyzed in more details.

To sum up, these validations show that the current model is able to simulate the pressure and temperature for the scratched bearing with a variety of speeds. The agreements in pressure are very good; the agreements in temperatures are fair, and by some means depend on the speeds. The agreements seem to be better for lower-speed cases.

1 scratch: [2 mm, L/2, 90 μ m] ■ Experiment, Speed 3500 rpm — THD simulation, Speed 3500 rpm
 LOAD: 6,000 N ■ Experiment, Speed 2750 rpm — THD simulation, Speed 2750 rpm
 SPEED=3,500; 2750; 2000 RPM ■ Experiment, Speed 2000 rpm — THD simulation, Speed 2000 rpm



(a)



(b)

Figure 4.10. Comparison of temperature profiles for different rotational speeds: (a) Circumferential direction, in bearing mid-plane, (b) Axial direction at angles 200°. Speed: 2,000; 2750, 3500 rpm.

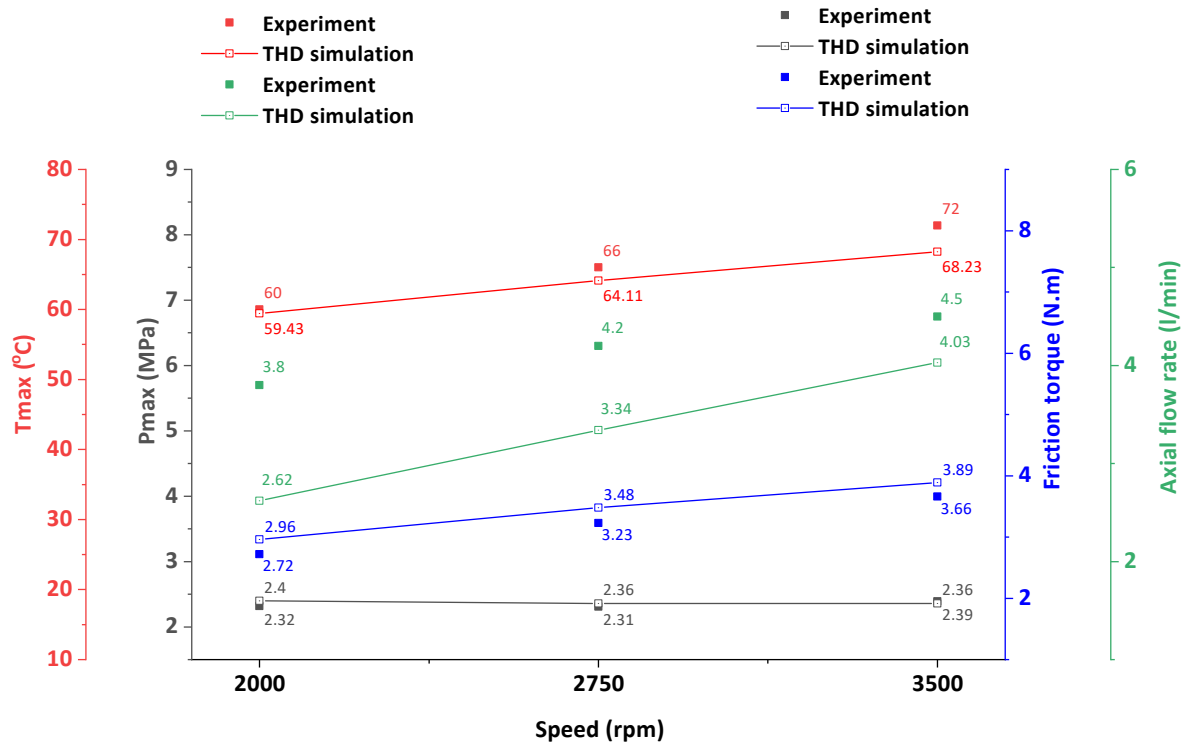


Figure 4.11. Comparison of bearing global performance parameters: maximum pressure, maximum temperature, friction torque, and axial flow rate for different rotational speeds.

Figure 4.11 compares simulation and measured data for the global performance parameters of the bearing. These results show good agreements for maximum pressures, maximum temperatures and friction torques, but large discrepancies for axial flow rates. The difference, on average, in maximum pressures is about 2%, in the maximum temperatures is 3%, in friction torques and axial flow rates are 7% and 24%, respectively. Increasing the speed (from 2,000 to 3,500 rpm) does not change the differences in maximum pressures, friction torques; however, it increased the difference in maximum temperatures slightly from 1 to 3% and decreased the difference in flow rates from 37 to 11%. The presentation of the flow rates in these comparisons is only to show the tendencies, not for comparing point-to-point values since the model does not take into account the axial leakage flows in the groove regions; therefore, the differences between calculated and measured values could be large.

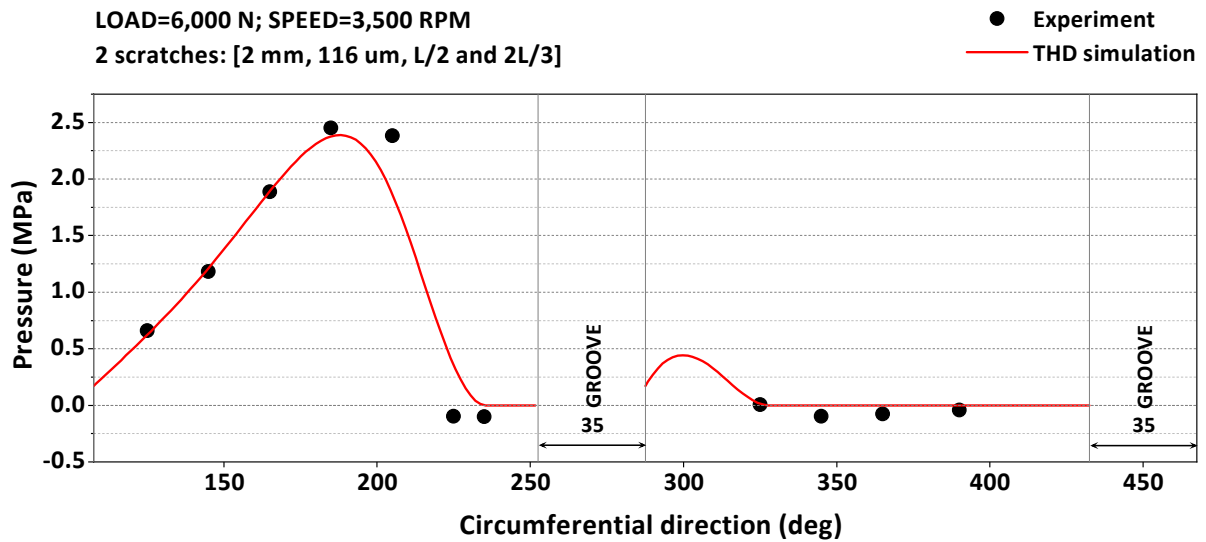
4.3. Validation for bearings with two scratches

In this section, two cases of validation are presented for a journal bearing with two scratches: one with average depths and the other with deep scratches. For all the validation cases in this subsection, the scratch has a width of 2 mm; the bearing operating condition is kept unchanged with an applied load of 6,000 N and a rotational speed of 3,500 rpm. The depth of the scratch and the scratch position are different for the two cases: one with two scratches with a depth of 116 μm , at $L/3$ and $2L/3$ and the other case with a depth of 255 μm , at $5L/12$ and $7L/12$.

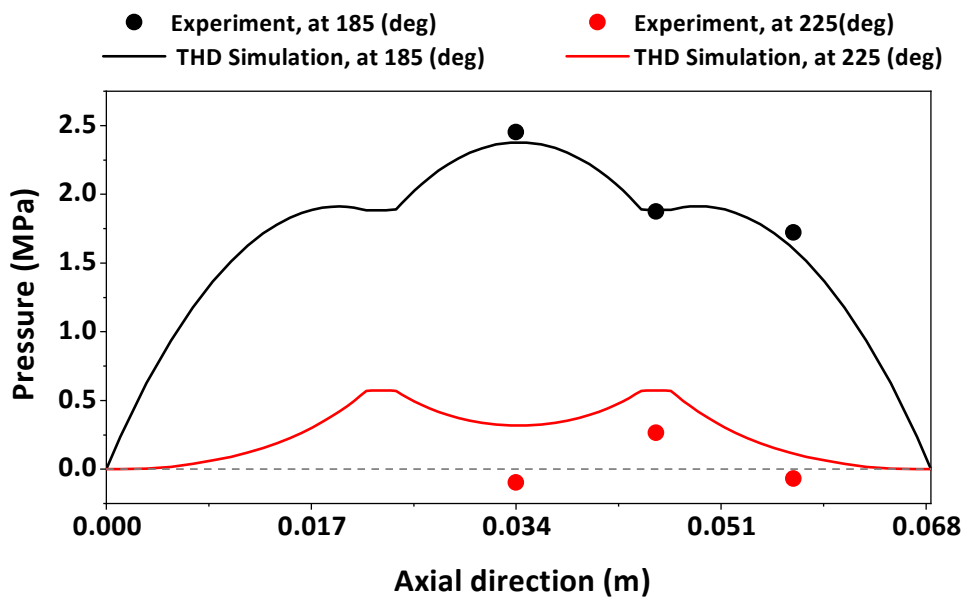
4.3.1. Case of depth of 116 μm , at $L/3$ and $2L/3$

Figure 4.12 compares simulation and experimental results for the pressure profiles in the bearing mid-plane (Fig. 4.12a) and in axial direction (Fig. 4.12b). From Fig. 4.12a we can see that the agreement in circumferential pressures in the bearing mid-plan is very good in terms of shape and value with the maximum differences are about 3-5 %. Similar tendency is found for the axial pressure profiles at two angles 185° and 225° (Fig. 4.12b) with the perfect agreement in the trend and values as well. These results indicate that the model is successful to simulate pressure distribution for two-scratch bearings.

Figure 4.13 presents temperature comparisons in circumferential direction in the bearing mid-plane and axial direction at two angles 180° and 200°. Good agreements again are found the low loaded lobe (Fig. 4.13a) with the differences range from 1 to 2.5 K, while the discrepancy in the high loaded lobe is higher with differences range from 3 to 7 K. These results are similar to the results obtained in the cases of one-scratch bearing.

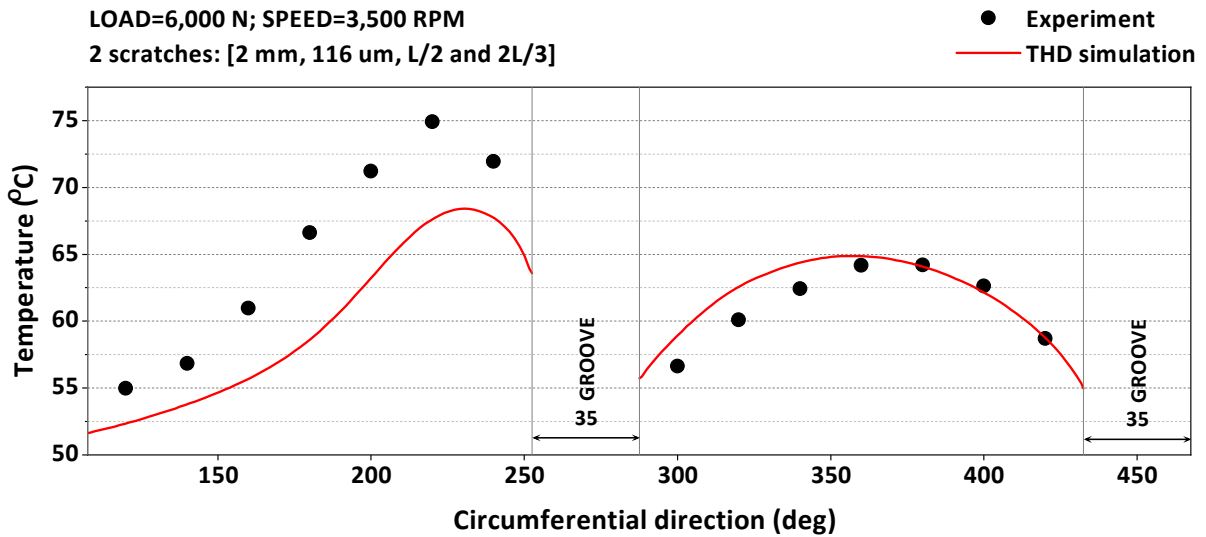


(a)

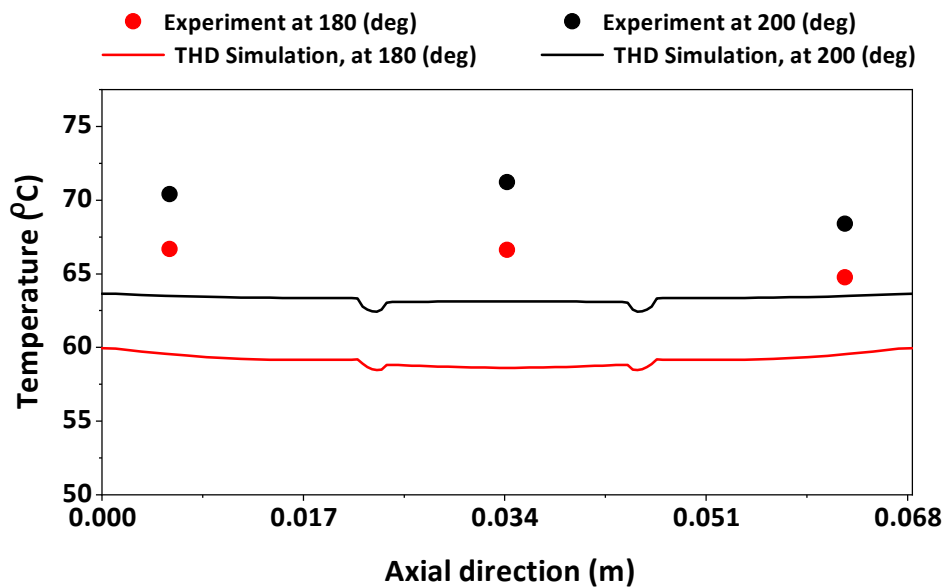


(b)

Figure 4.12. Comparison of pressure profiles for a two-scratch bearing:(a) Circumferential direction, in bearing mid-plane, (b) Axial direction at angles 185° and 225°. Scratch depth of 116 μ m, at L/3 and 2L/3.



(a)



(b)

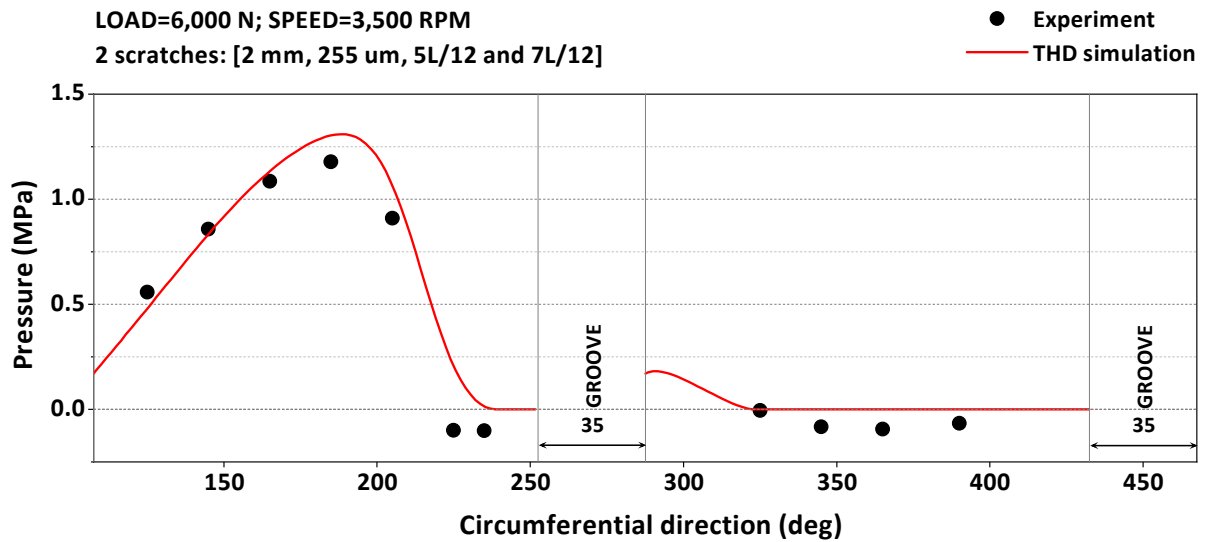
Figure 4.13. Comparison of temperature profiles for a two-scratch bearing:(a) Circumferential direction, in bearing mid-plane, (b) Axial direction at angles 180° and 200°. Scratch depth of 116 μm , at L/3 and 2L/3.

4.3.2. Case of depth of 255 μm , at 5L/12 and 7L/12

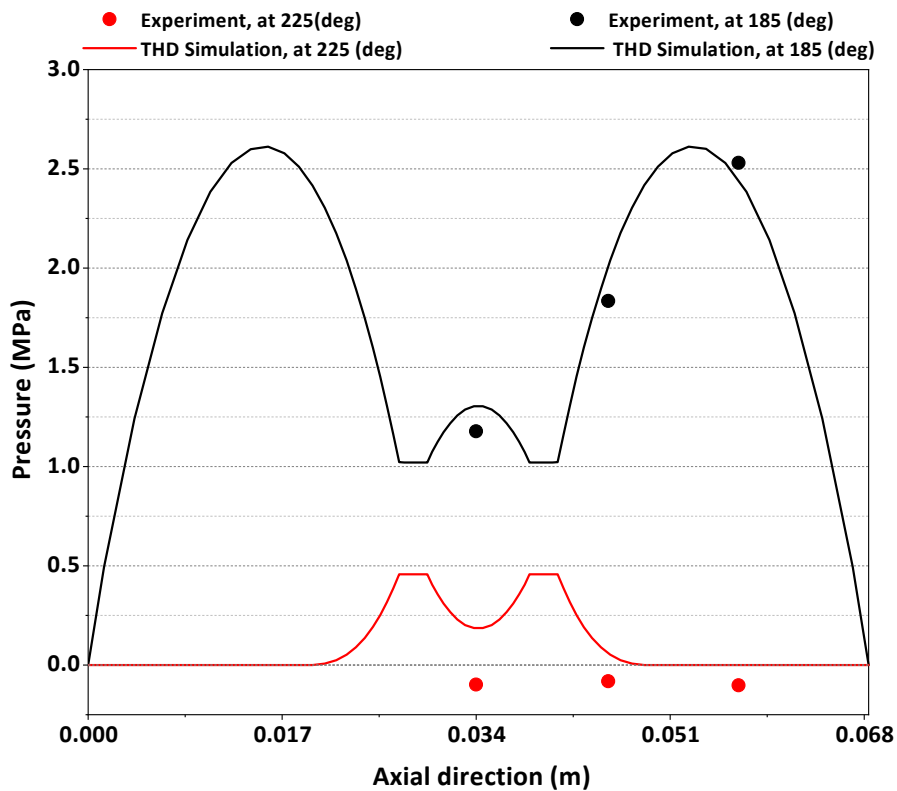
Another validation for a two-scratch configuration was performed with deeper scratches at different positions. The scratches have a depth of 255 μm and locate at 5L/12 and 7L/12. Other parameters are kept unchanged from the previous validation.

Validation results are presented in Figure 4.14 for pressure profiles and in Figure 4.15 for temperature profiles. As we can see from Fig. 4.14, although the pressure distribution is modified significantly especially in the axial direction, the model is able to identify and correctly calculate the pressures with the same order of accuracy as obtained with the case with average depth.

Temperature comparison (Fig. 4.15) shows the same tendency as it was obtained from the previous validation with a good agreement for the low loaded load the differences from 1 to 3 K and a fair agreement in the high loaded lobe, the differences from 3 to 7 K.

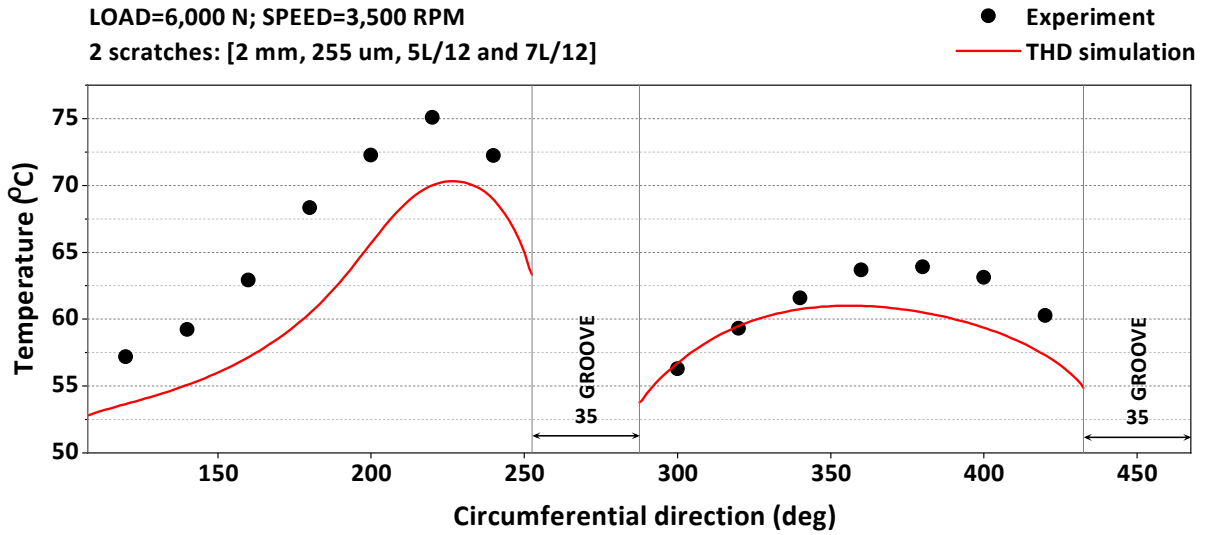


(a)

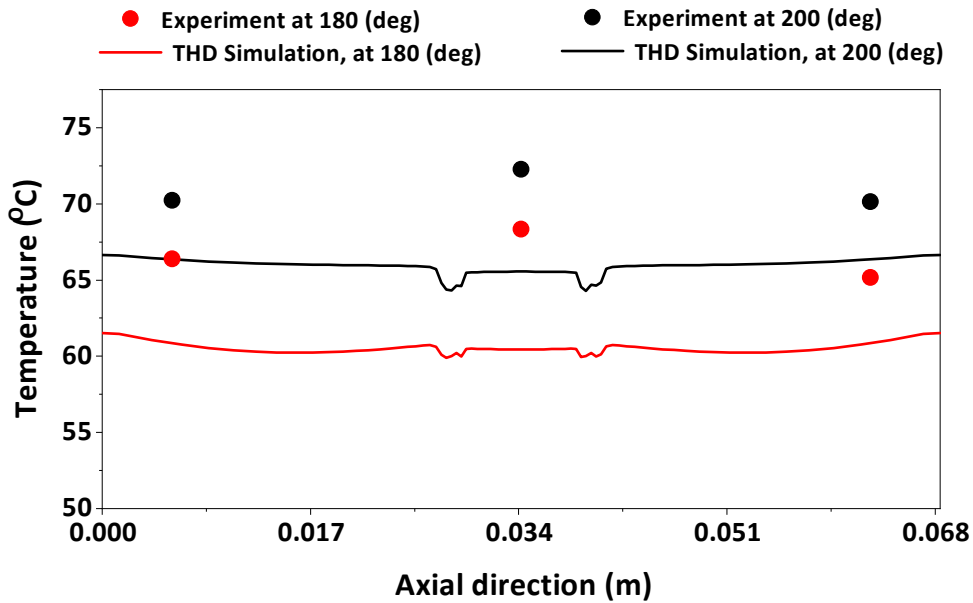


(b)

Figure 4.14. Comparison of pressure profiles for a two-scratch bearing: (a) Circumferential direction, in bearing mid-plane, (b) Axial direction at angles 185° and 225° . Scratch depth of $255 \mu\text{m}$, at $L/3$ and $2L/3$.



(a)



(b)

Figure 4.15. Comparison of temperature profiles for a two-scratch bearing: (a) Circumferential direction, in bearing mid-plane, (b) Axial direction at angles 180° and 200°; scratch depth of 255 μm , at 5L/12 and 5L/12.

To sum up, these two validations show that the current model is able to simulate the bearings with two scratches with a high consistency and same accuracy level as they were obtained for the cases of bearings with one scratch. It suggests that the number and position of the scratch do not have significant influences on the obtained solutions.

4.4. Conclusions

This chapter presented a wide range of validation cases with a variety of different scratch geometric parameters, i.e. scratch depth and position, and bearing operating conditions, i.e. applied load and rotational speed. Comparisons of pressure, temperature distributions, and crucial global parameters of bearing performance were performed. We have obtained satisfactory and comprehensive results showing that the current THD model is able to simulate scratched journal bearings with a high consistent and satisfactory accuracy. We believe this model could be applied to study scratched journal bearings. The next chapter presents several numerical studies with this THD model.

Chapter 5. Numerical studies

5.1. Aim of the study

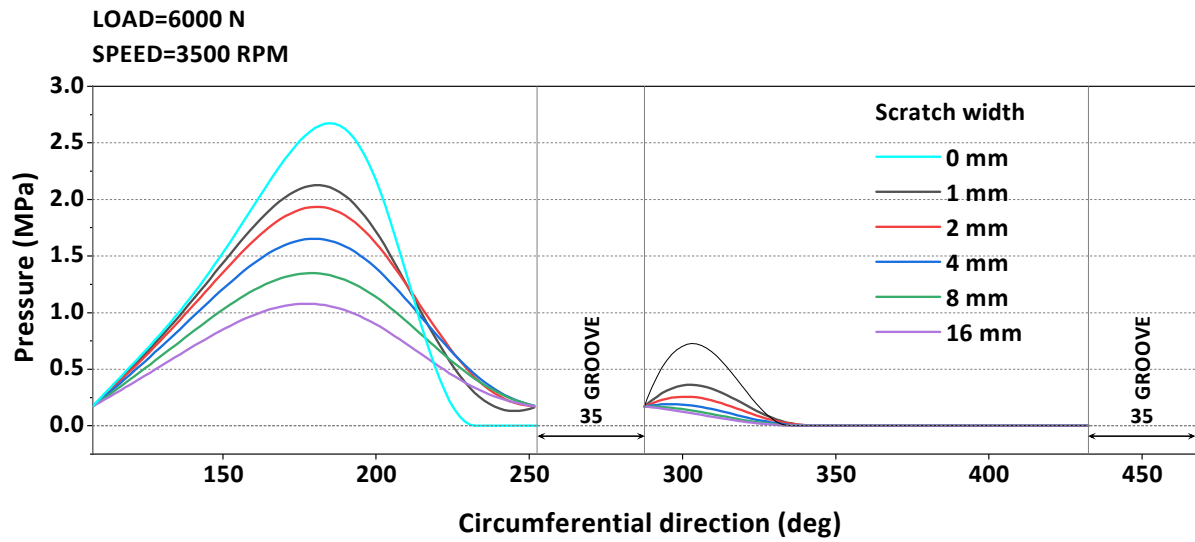
In this chapter, we present numerical studies of the two-lobe scratched journal bearing used for validation in the previous chapter. This work studies the effects of the scratch width, the scratches position, and the number of scratches on the performance of the bearing. The pressure, velocity, temperature profiles, and several global parameters such as eccentricity, attitude angle, minimum film thickness, maximum temperature, friction torques, and other parameters, are studied. In addition, a case study on a real multiple scratched bearing is also presented.

5.2. Effect of scratch width

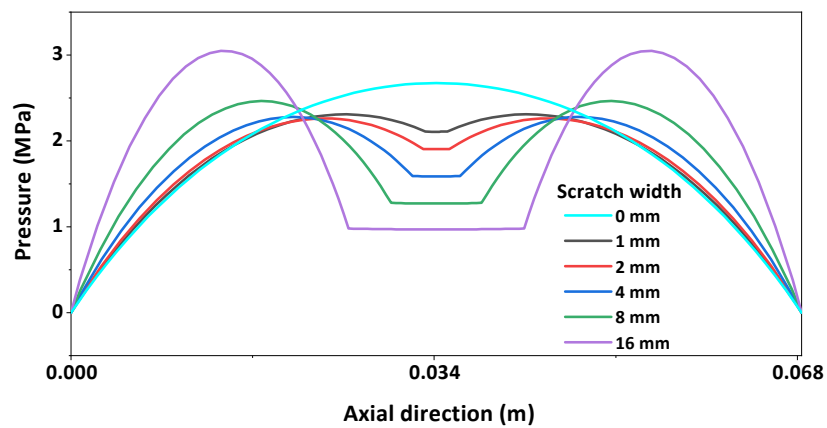
In this section, several cases of simulations are presented, in which the scratch width is varied. For all the simulations in this subsection, the scratch is at $L/2$ and a depth of $140\ \mu\text{m}$ (1C); the rotational speed is 3,500 rpm and the applied load is 6,000 N. The scratch width is varied from 1 mm up to 16 mm. Simulation results are presented in Figure 5.1 and Figure 5.2 for pressure and temperature profiles, respectively.

Figure 5.1 shows the pressure profiles in the bearing mid-plane (Fig. 4.3a) and in the axial direction at the maximum pressure location (Fig. 4.3b) for cases with different widths. It can be seen in Fig. 5.1a that increasing the scratch width decreases pressures in the bearing

mid-plane. The pressure dropped by more than 50% with the scratch depth of 16 mm compared to the 1 mm scratch width case. In Fig. 5.1b, we also observed the strong modification in the axial pressures. For narrow scratch e.g. 1 to 2 mm the modifications were not significant, however for the wider scratch cases the pressure profiles were modified strongly and the maximum pressure increased. For the 16 mm width case, the maximum pressure increased almost 40% compared to the 1 mm width case. It can be explained that increasing the width of the scratch increases the scratch area that corresponds to the pressure drop. When the scratch width is too wide, the loss of pressures in this region is larger and it needs to be compensated for the bearing to support the same applied load and therefore the pressures in non-scratch regions need to be increased and it leads to an increase in the maximum pressure and pressure gradients in the axial direction.



(a)



(b)

Figure 5.1. Comparison of simulation pressure profiles for different scratch widths: (a) Circumferential direction, in bearing mid-plane, (b) Axial direction, in Pmax plane. Scratch width: 1, 2, 4, 8, 16 mm.

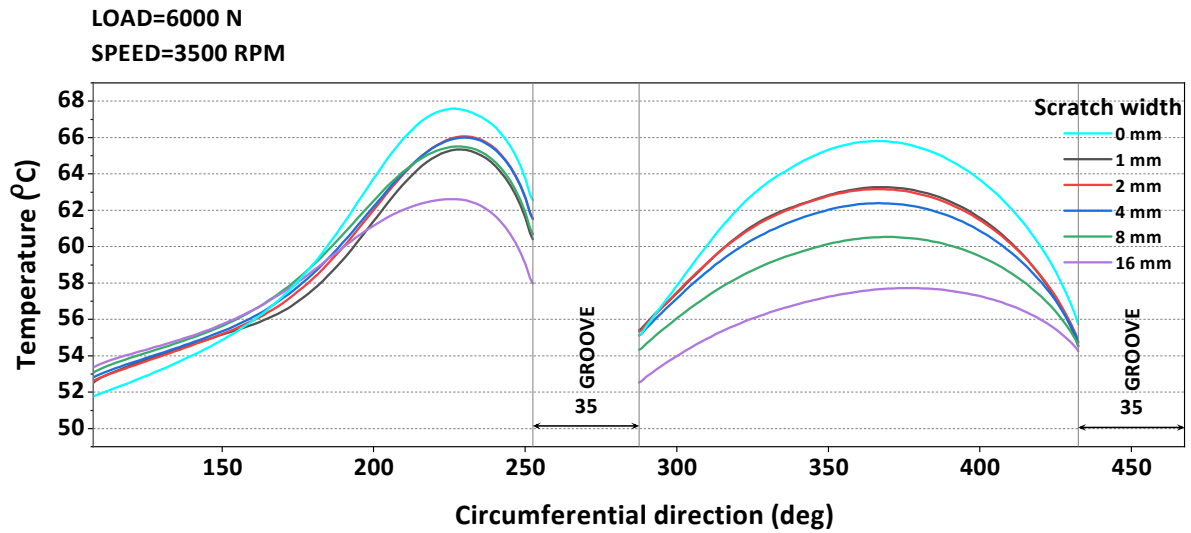


Figure 5.2. Comparison of simulation circumferential temperature profiles in bearing mid-plane for different scratch widths. Scratch width: 1, 2, 4, 8, 16 mm.

Table 5.1. Global parameters versus scratch width.

Width	Hmin	change	Pmax	change	Tmax	change	ε	change	ϕ_0	change
1 mm	42.67	0%	2.31	0%	68.03	0	0.89	0%	85.10	0%
2 mm	40.80	-4%	2.26	-2%	68.66	3%	0.91	2%	83.79	-2%
4 mm	36.83	-14%	2.28	-1%	69.66	7%	0.96	7%	81.57	-4%
8 mm	31.20	-27%	2.47	7%	71.30	13%	1.01	13%	77.66	-9%
16 mm	23.56	-45%	3.05	32%	73.13	20%	1.05	18%	70.56	-17%

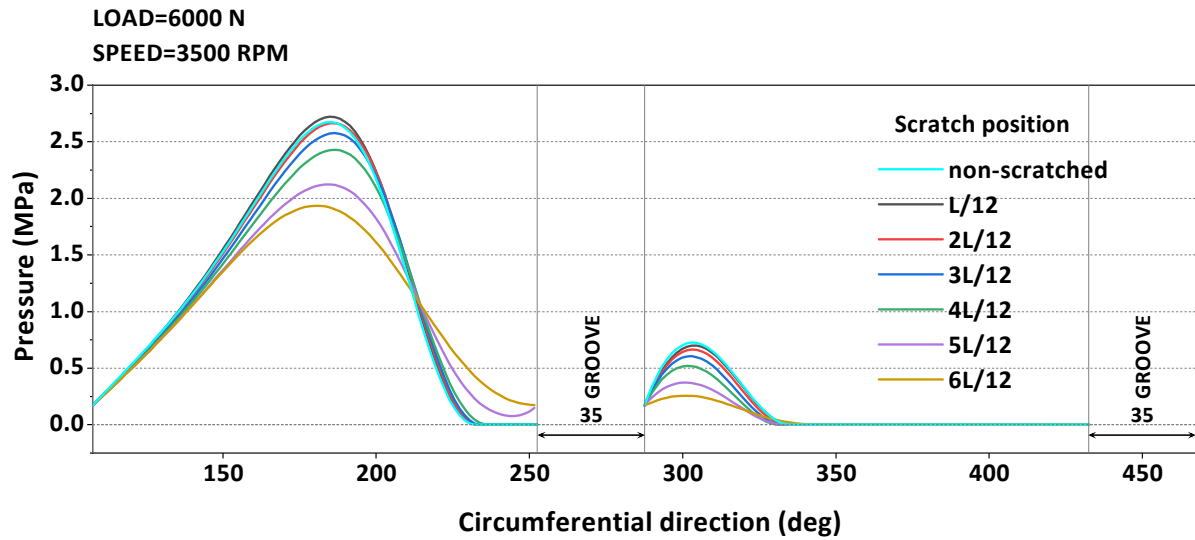
Figure 5.2 compares the temperature profiles at the film/bush interface, in the bearing mid-plane. The temperatures in the high loaded lobe did not change significantly for all the widths from 1 to 8 mm, however it dropped about 4 K for the 16 mm width case. For the low loaded lobe, temperatures tend to decrease when increasing the scratch width. Nevertheless, with two cases of narrow scratch i.e. 1 and 2 mm, the temperature profiles were almost unchanged in the bearing mid-plane.

Table 5.1 presents variations in global parameters including the minimum film thickness, maximum pressure, maximum temperature, relative eccentricity, and attitude angle when increasing the scratch width. The fact that as the scratch width increases (from 1 to 16 mm), the pressure in the scratch decreases and the active zone of the bearing decreases significantly for mainly two reasons: in axial direction, because the pressure in the scratch is less and less contributing the load carrying capacity and so, its behavior is becoming similar to a twin bearings of narrow width; in the circumferential direction, as the scratch width increases, the journal eccentricity increases (from 2 to 18%) and the attitude angle decreases (2 to 17%) leading the significant reduction of the angular amplitude of the active zone (high pressure zone). The minimum film thickness decreased 45% in the case 16 mm width. The differences between maximum temperature and supply temperature also increase from 3 to 20% although the temperature in the scratch region decreased as shown in Fig. 5.2.

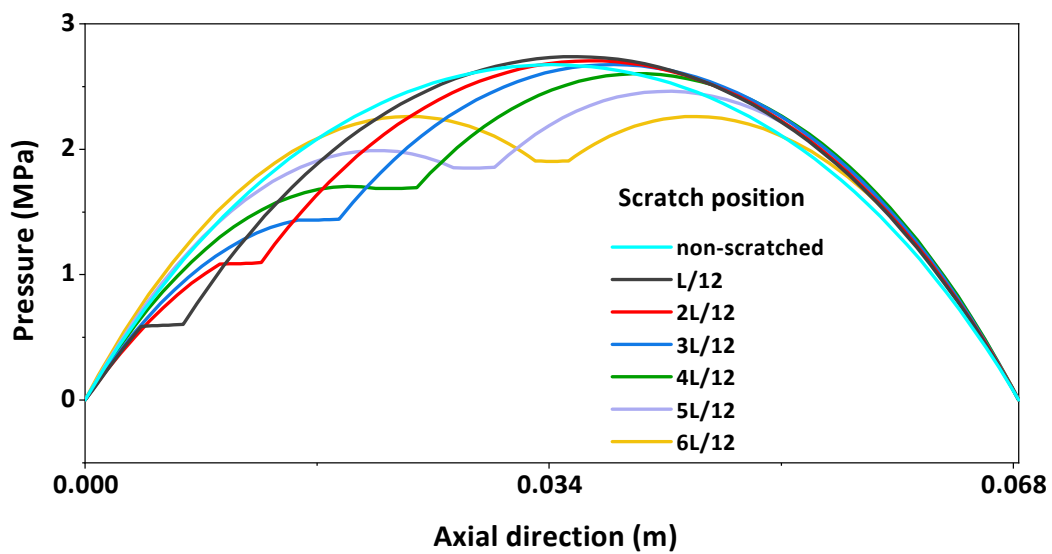
5.3. Effect of scratch position

In this section, several cases of simulations are presented, in which the scratch position is varied from the side to mid-plane of the bearing. For all the simulations cases in this subsection, the scratch has a depth of 140 μm (1C) and a width of 2mm; the applied load is 6,000 N and rotational speed is 3,500 rpm. The relative position of the scratch varies from $L/12$ to $L/2$, with a step of $L/12$, where L is the bearing length. Simulation results are presented in Figure 5.3 and 5.4 for pressure and temperature profiles, respectively.

The pressure in the bearing mid-plane changed with different positions of the scratch (Fig. 5.3a). It decreased when the scratch was moved from $L/12$ to the bearing mid-plane. It can be seen in Fig. 5.3b that the axial pressure profiles were changed but not significantly. Temperature profiles were almost unchanged with different scratch positions (Fig.5.4).



(a) In the bearing mid-plane



(b) At the maximum pressure location

Figure 5.3. Comparison of pressure profiles for different scratch positions: a) Circumferential direction, in bearing mid-plane, (b) Axial direction, in Pmax plane.

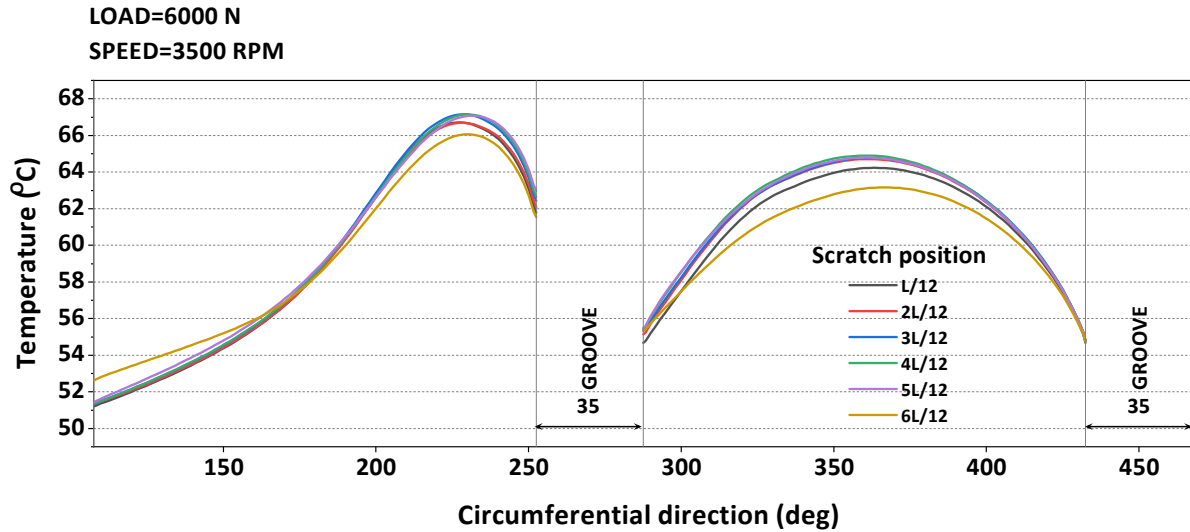


Figure 5.4. Comparison of simulation temperature profiles for different scratch positions.

Table 5.2. Global parameters versus scratch relative position.

Position	Hmin	change	Pmax	change	Tmax	change	ε	change	ϕ_0	change
L/12	44.29	0%	2.74	0%	67.91	0.0%	0.84	0%	84.47	0%
2L/12	43.71	-1%	2.71	-1%	68.01	0.4%	0.86	2%	84.63	0.2%
3L/12	42.65	-4%	2.68	-2%	68.35	1.8%	0.88	4%	84.41	-0.1%
4L/12	41.67	-6%	2.60	-5%	68.48	2.3%	0.90	6%	84.11	-0.4%
5L/12	41	-7%	2.46	-10%	68.60	2.8%	0.91	7%	83.86	-0.7%
6L/12	40.80	-8%	2.26	-17%	68.66	3.0%	0.91	8%	83.79	-0.8%

Table 5.2 presents variations in global parameters including the minimum film thickness, maximum pressure, maximum temperature, relative eccentricity, and attitude angle when changing the relative position of the scratch. As can be seen that the position of the scratch has less significant influence on the global parameters. The differences between maximum temperature and supply temperature only increase about 0.4 to 3%, the attitude angle is almost unchanged. However, the eccentricity slightly increases leading the minimum thickness decreases when the scratch is moved close to the bearing mid-plane. It can be because the influence is stronger when the scratch is situated in a zone of higher hydrodynamic pressure.

5.4. Finding critical value of scratch depth for the scratched bearing

It was observed in the previous sections that the scratch significantly modifies the pressure profile and the temperature field. The presence of scratches can therefore induce a substantial loss in the load capacity of the bearing. For this reason, and for a given operating condition of the bearing, it is helpful to find a rough estimate of the maximum value of the scratch depth for which the bearing can create sufficient hydrodynamic pressure, using Reynolds' solution, to support the applied load and rotational speed. It is observed in our simulations that, under certain operating conditions of the bearing, the THD model cannot converge to a final solution if the scratch depth is greater than a limiting value.

To estimate this value, several simulations were performed in which the scratch located at $L/2$, with a width of 2mm and the depth was varied from 0 to the maximum admissible value of the scratch depth for which a convergence could be reached. The applied load and rotational speed are 6,000 N and 3,500 rpm, respectively.

Figure 5.5 shows an overview of the influence of increasing the scratch depth on the bearing global performance parameters. The maximum pressure (olive curve) increases for the depths larger than $1C$, maximum temperature (violet curve) and friction torque (cyan curve) increase only slightly. Increasing the scratch depth increases the eccentricity (dark yellow curve) and decreases the minimum film thickness (black curve).

Because the pressure drops in the scratch zone, it leads to a loss in load capacity. Therefore, in order to support the same applied load, the bearing must operate under a higher eccentricity, corresponding to a lower minimum film thickness. For the scratch depth values larger than $396 \mu\text{m}$, the model could not converge to a solution. The reason is that the eccentricity reached to its limit value at the current decreasing attitude angle, resulting the

minimum film thickness decreases closely to nil. With these configurations, the local pressure and velocity gradients are very large and lead to large local gradients temperatures. When these temperatures exceed the limit temperature range in the viscosity–temperature relationship model (McCoull and Walther equation in current model), the energy equation also failed to be converged. It is therefore considered that the value of 396 μm is the estimated limit value of the scratch depth for the simulated scratched bearing using the current model. The value of 396 μm is not a critical scratch depth value of the bearing but the limit scratch depth value of the current model at which the model cannot automatically update to a solution. In fact, for this preload bearing, when then scratch is higher than 396 μm , the eccentricity is expected to decrease while the attitude angle and the minimum film thickness is decreasing. It is contrasted to the case of a non-preloaded bearing in which the eccentricity only increases when the scratch depth is increased. For cases which scratch depth higher than 396 μm , a manual procedure can be applied by extrapolation method to estimate the eccentricity and the attitude angle and find the solution with imposed position simulation and the critical value of the scratch depth is expected to be higher than 396 μm .

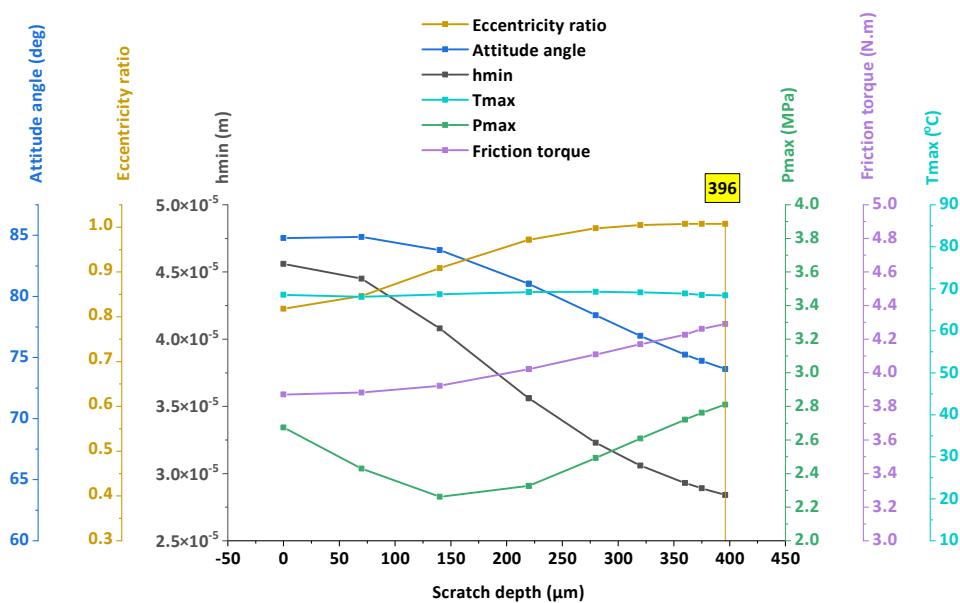


Figure 5.5. Comparison of simulation bearing global parameters for different scratch depths.

5.5. Finding critical value of applied load for the scratched bearing

It is observed in both theory and experiments that the load capacity of the bearing is reduced by the presence of the scratch. The load capacity of the scratched bearing is lower compared to non-scratched bearing under the same operating conditions. It is therefore helpful to estimate the maximum value of the load capacity with a Reynolds' solution for a given scratch characteristics and bearing operating conditions.

To estimate the limit value for the applied load, several simulations were performed in which the applied load was varied from 2,000 N to maximum admissible value. The rotational speed is 3,500 rpm, the scratch depth is 140 μm , its width 2 mm and its location is $L/2$. The results are shown in Fig. 5.6 for the limiting value of load capacity and global parameters of bearing performance.

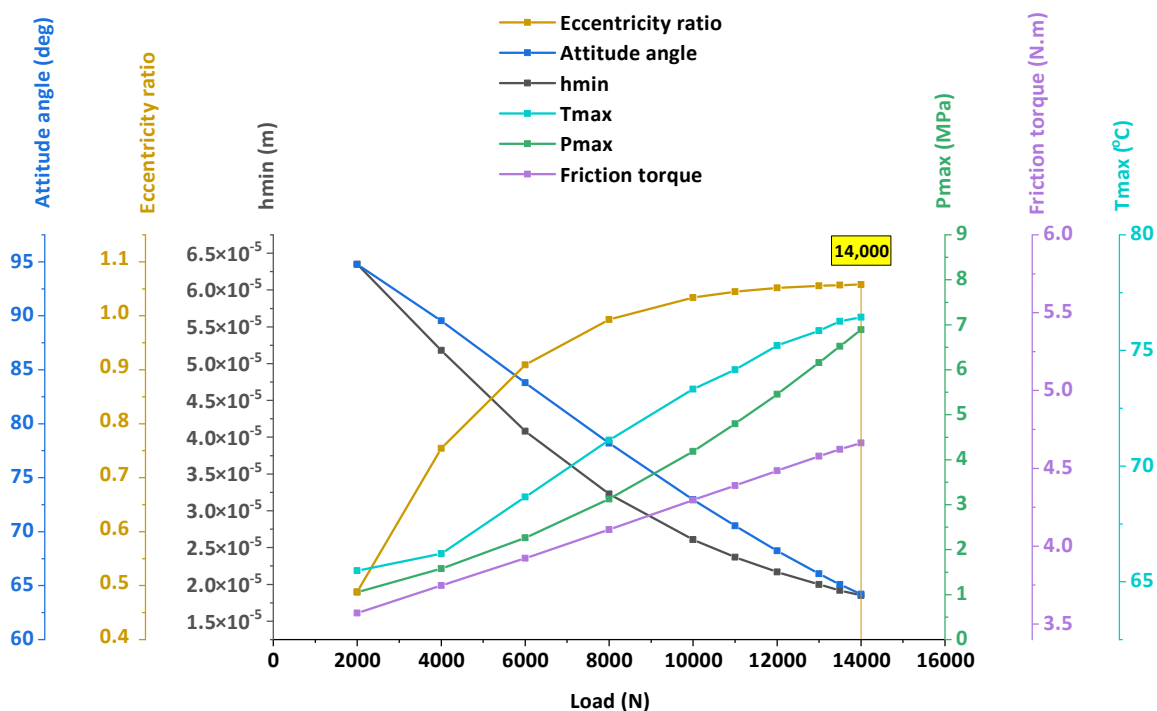


Figure 5.6. Comparison of simulation bearing global parameters for different applied loads.

It can be seen that the maximum pressure, temperature, and friction torque increase as the applied load is being increased. These tendencies are appropriate with Reynolds's solutions. Increasing the applied load increases the eccentricity and decreases the minimum film thickness and with the applied load values larger than 14,000 N, the model could not converge to final solutions. The explanation for this is similar to the previous simulations of different scratch depths when the minimum film thickness is converged to very small values and the energy equation is failed to be converged. It is therefore considered that the value of 14,000 N is the estimated limit or critical value of the applied load for the simulated scratched bearing by using the current model.

5.6. Negative velocity in the scratch regions

In this section, velocity component u in the circumferential direction is presented to understand how the modifications of pressure profiles in the scratch regions change fluid flows. The rotational speed is 3,500 rpm, the scratch depth is 140 μm , its width 2 mm and its location is $L/2$.

5.6.1. Velocity u for different scratch depths

Figure 5.7 presents sliding velocity profiles u at the mid-plane of the scratch at the inlet section of the bearing of the high loaded lobe. These results are taken from the simulations in section 5.4 with different scratch depths. The horizontal axis presents the sliding velocities, and the vertical axis presents the dimensionless film thickness.

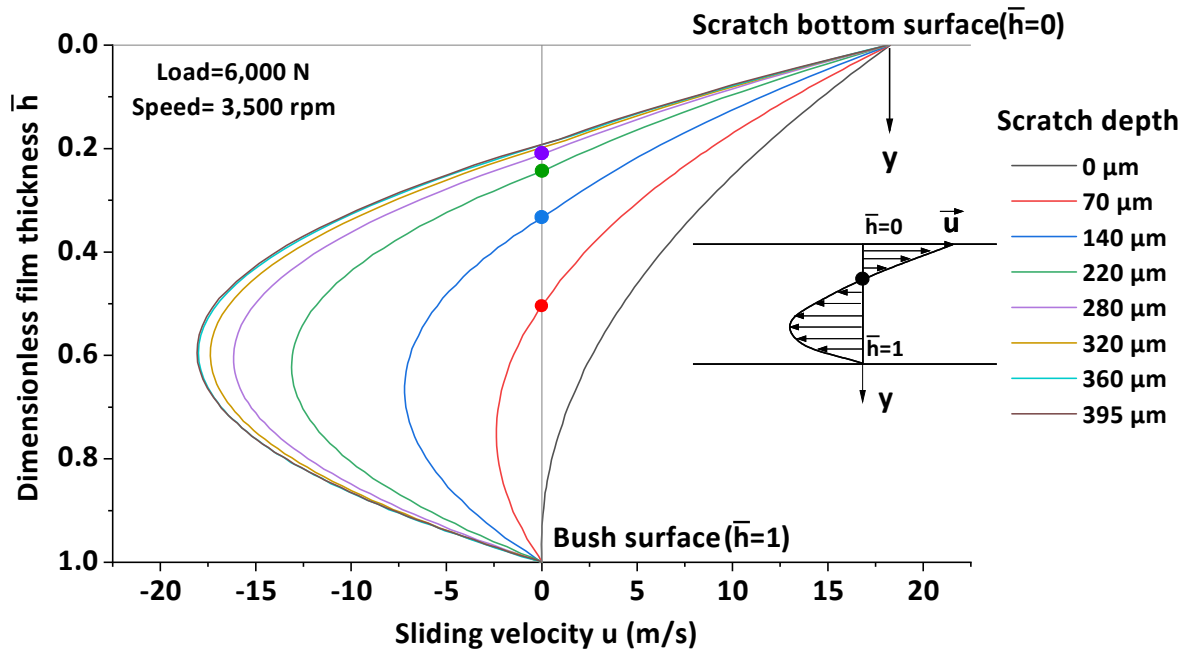


Figure 5.7. Sliding velocity u component across the film thickness in mid-scratch at the inlet of high loaded lobe, with different scratch depths.

As we can see, the velocity profiles differ from different scratch depths. It is observed that there are negative velocities which correspond to reverse flows at the inlet of the lobe. There is no negative velocity with the non-scratched bearing. In addition, the portion and maximum values of the negative velocities are proportional to the scratch depth. The existence of these negative velocities (corresponding to negative flows) can be explained: in the scratch region, the pressure gradients in the axial direction are larger when compared to pressure gradients in the non-scratched case, and thus axial pressure gradients force the fluid entering inside the scratch from the sides of the scratch (recall Figure 4.3). Because the fluid is uncompressed, it should move in the scratch channel both downstream and upstream in the circumferential direction. The fluid flow is driven by two components i.e. pressure-driven flow and velocity-driven flow. At the inlet of the lobe, the velocity-driven flow dominates the pressure-driven flow because the pressure and pressure gradients are low. If the circumferential pressure and velocity gradients at the inlet are large enough and dominate the axial

pressure gradients, then the reverse flows cannot exist, and the fluid should go in the positive direction only. However, because both the pressure and velocity gradients in the circumferential direction are low in the scratch region, and lower at the regions which are close to inner bush surface, the axial pressure gradients therefore can dominate the circumferential pressure and velocity gradients, and force the fluid go downstream back to the groove. It is also understandable why the portion and maximum negative velocities increase with the increases of the scratch depth, which responding to lower pressure and lower circumferential pressure gradients in the scratch region.

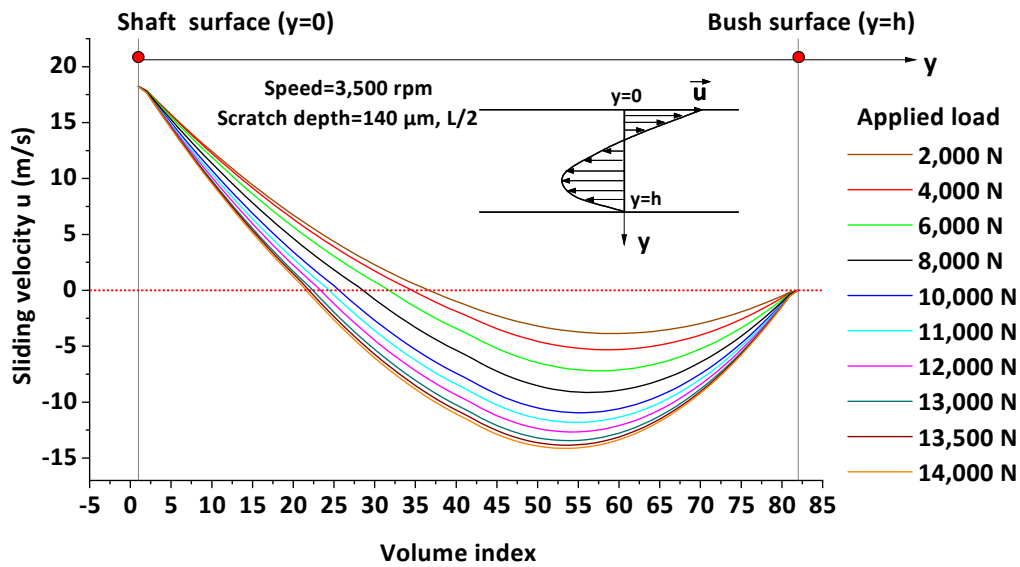
The reverse flows can influence the heat balance in the groove regions and should be considered when modeling the energy balance at the groove, to determine the inlet temperature more accurately. In our model, this phenomenon was already taken into account (Appendix A).

5.6.2. Velocity u for different applied loads and rotational speeds

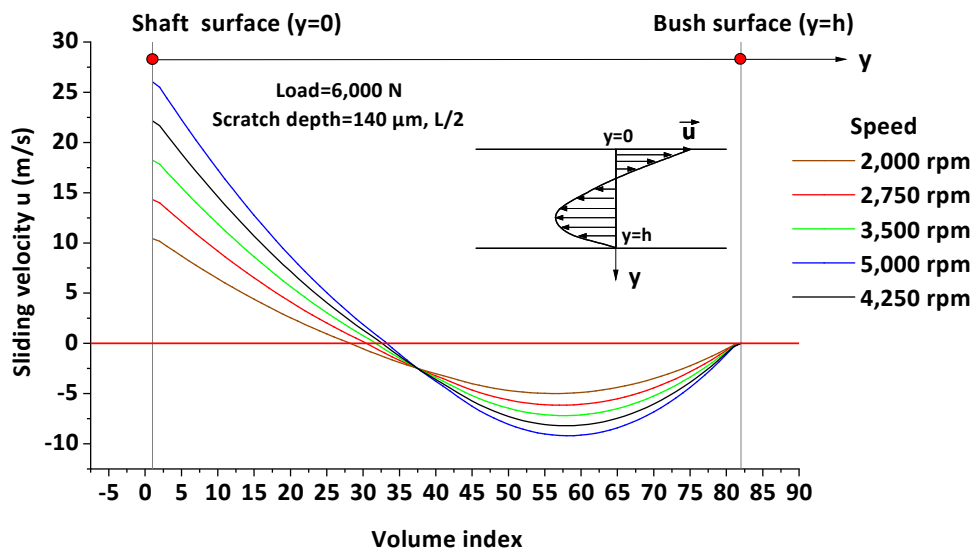
To further understand the negative velocities in the scratch region, the velocities for several cases with different bearing operation conditions were analyzed. The results are shown in Figure 5.8 for the velocities with different loads (Fig. 5.8a) and for the velocities with different rotational speeds (Fig. 5.8b). The scratch has a depth of $140\ \mu\text{m}$ (1C) at $L/2$; the rotational speed is 3,500 rpm for simulations with different loads; the applied load is 6,000 N for simulations with different rotational speeds.

It can be seen that the negative velocity increases when the applied load increases (Fig. 5.8a). This result supports the explanation for the negative velocity from the previous

section, which indicates that the axial pressure gradients are the major reasons for the negative velocity. The axial pressure gradients increase with increases of the applied load and lead to larger negative velocities.



(a)



(b)

Figure 5.8. Sliding velocity u component across the film thickness in mid-scratch at the inlet of high loaded lobe: (a) with different loads, (b) with different speeds.

In Fig. 5.8b, we can see that the rotational speed also has an influence on the negative velocities; however, the influence is not significant. It can be explained by the fact that the rotational speed has a less significant influence (compared to the applied load) on the pressure gradients.

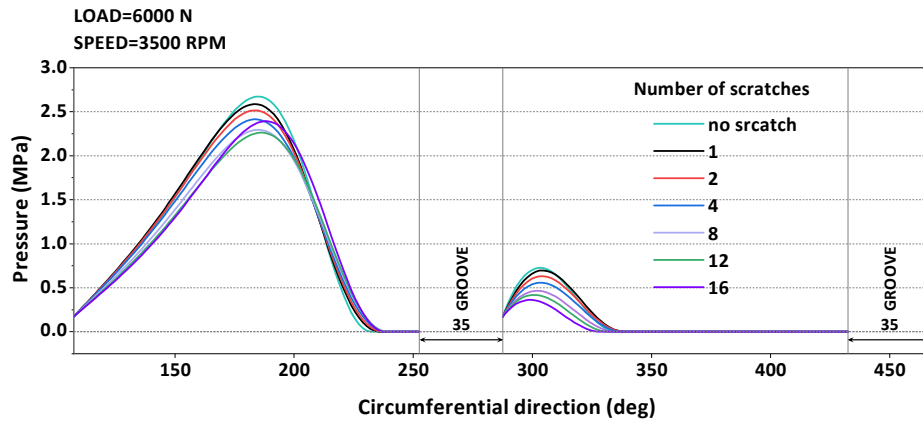
5.7. Study on multiple scratched bearings

Until now, all the simulation and experimental data were performed for either one scratch or two scratches. In this section, simulations for a multiple-scratched journal bearing are presented.

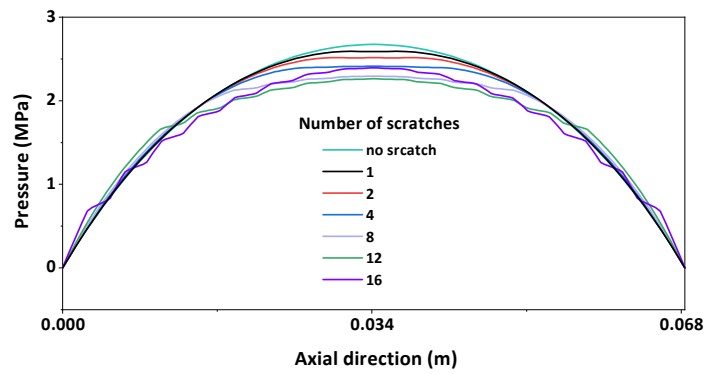
5.7.1. Effect of the number of scratches

This section simulates scratched bearing, in which the number of the scratch varied from 0 to 16 scratches. For all the validation cases in this subsection, all the scratches have a uniform depth of $30\ \mu\text{m}$ ($\sim C/4$) and a uniform width of 2 mm; the rotational speed is 3,500 rpm and applied load is 6,000 N. Simulation results are presented in Fig. 5.9a and Fig. 5.9b for pressure profiles in the circumferential and axial directions, respectively.

It can be seen in Fig. 5.9a and Fig. 5.9b that the pressure profiles are only slightly modified in both the circumferential and axial directions. Although increasing the number of scratches increases the surface area of the scratch region several times, the influence in the pressure profiles only changed slightly, with a maximum difference is about 14% (2.25 MPa in the one-scratch case versus 2.6 MPa in the sixteen scratches case).



(a)



(b)

Figure 5.9. Comparison of pressure profiles for different number of scratches: (a) in mid-plane, (b) at maximum pressure location.

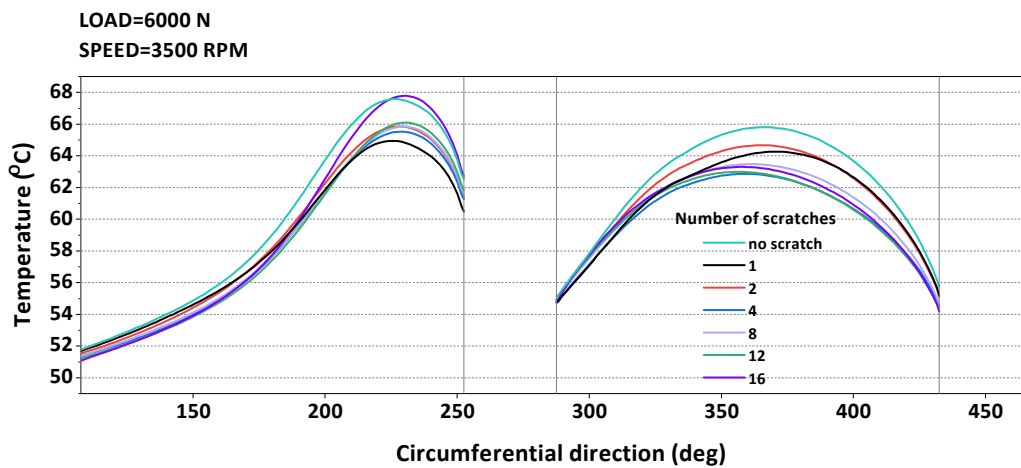


Figure 5.10. Comparison of simulation temperature profiles for different number of scratches.

Figure 5.10 compares simulation temperature profiles in the circumferential direction at the film/bush interface, in bearing mid-plane. It can be seen that the temperatures do not change significantly as well. The maximum temperature for the case of one scratch is about 65 °C, versus 67.5 °C for the case of sixteen scratches. Increasing the scratch area sixteen times only increases the maximum temperature about 2.5 K.

In summary, the number of scratches seems not induce a strong influence in both pressure and temperature profiles for these shallow scratch cases.

5.7.2. Comparisons between hydrodynamic and THD simulations

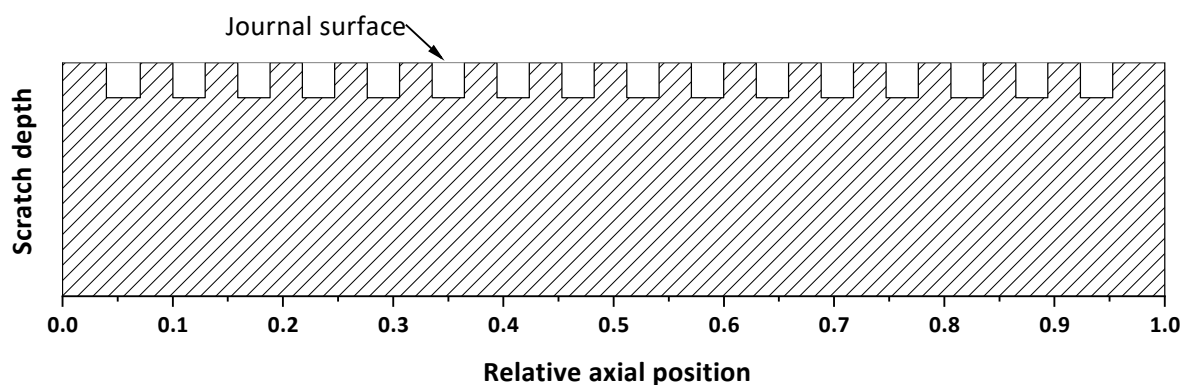


Figure 5.11. Scratch geometry of a sixteen-scratch bearing.

As we observed in the previous sections that with current model, there is a critical value of the scratch depth where the model cannot result in final solutions if the scratch depth is larger than that value. To understand deeper in this phenomenon, this section compares simulation results with different models i.e. hydrodynamic models with global temperatures at 45 °C and 65 °C, and the current studied THD model for a sixteen-scratch journal bearing with the geometry shown in Fig. 5.11. All sixteen scratches have a uniform width at 2 mm and the distance between two successive scratches is $L/17$. Several bearing global parameters e.g.

the minimum film thickness, attitude angle, relative eccentricity, and maximum pressure are compared and the results are presented in Fig. 5.12.

The hydrodynamic model with global temperature at 45 °C results in higher solutions in the minimum film thickness (Fig. 5.12a), higher attitude angle (Fig. 5.12b) and lower eccentricity (Fig. 5.12c), compared to the solutions obtained with the THD model and the 65 °C hydrodynamic model for the same configuration with the scratch depths less than 40 μm . It is reasonable because the viscosity is lower with the lower temperature resulting higher hydrodynamic pressure and therefore the eccentricity is lower.

The 45 °C hydrodynamic model can result in final solutions if the scratch depth is less than the critical value at 149 μm . With the scratch depth of 149 μm and larger, the solutions could not be obtained, since the minimum film thickness converged close to nil and the maximum pressure converged to an extreme value at 513 MPa. The critical value of the scratch depth for the 65 °C hydrodynamic model is lower, at 90 μm , and for the case of THD the critical value is much lower, at 40 μm . The THD model could not result in a solution with the scratch depths which are higher than 40 μm because the energy equation was failed to be converged. It can be understandable that under the same operating conditions, the bearing must work under more severe condition i.e. lower eccentricity and higher minimum film thickness with higher temperature. Therefore, the model with lower temperature can result in a wider range of solutions for the scratch depth with the same operating conditions inputted.

It is interesting to observe that increasing a little the depth around the critical configuration can create a sudden drop in the film thickness to nil and leads to an extremely high value in the maximum pressure. For example, in the case of the 45 °C hydrodynamic model, with the depth of 148 μm , the minimum film thickness is about 5 μm , but with the depth of

149 μm , the minimum film thickness is almost nil (Fig.5,12a) and the maximum pressure increases to 513 MPa (Fig. 5.12d). Depending on the model chosen, the critical value of the scratch depth can be different, and the model cannot result in final solutions if the depth is larger than the critical value.

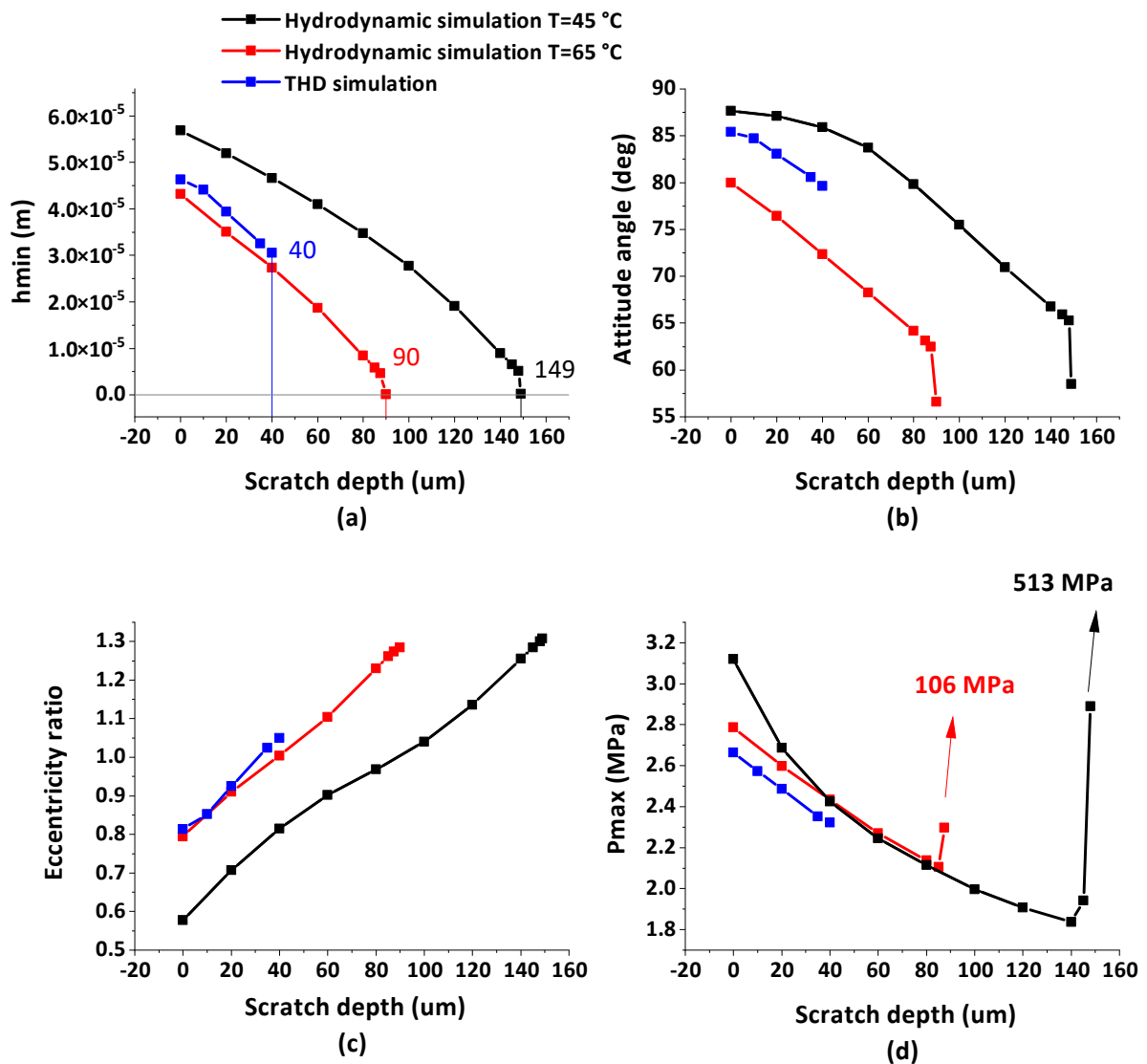


Figure 5.12. Comparisons of bearing global parameters with different simulation models: hydrodynamic simulation T=45 °C, hydrodynamic simulation T=65 °C, and THD simulation: (a) for minimum film thickness, (b) for attitude angle, (c) for eccentricity ratio, (d) for maximum pressure.

5.7.3. A case study for multiple scratches with real geometry

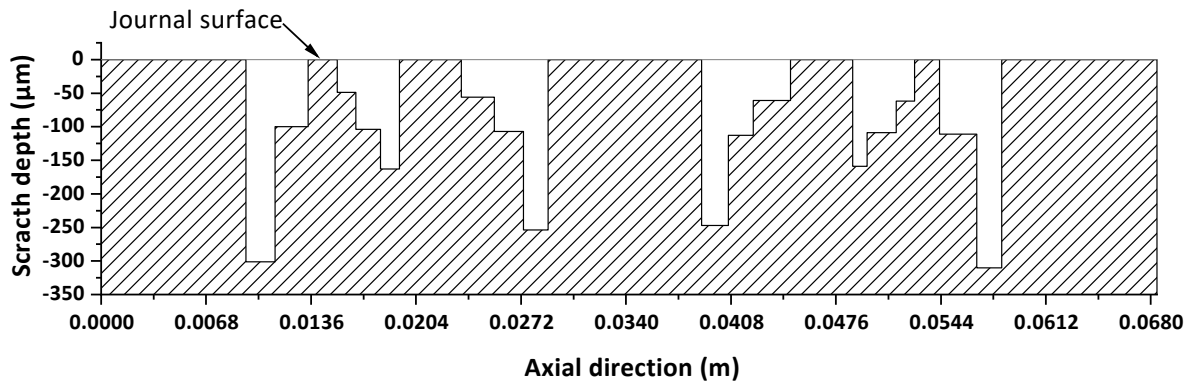


Figure 5.13. Scratch profile.

This section presents a real case of a bearing with multiple scratches with different depths and widths. The scratch profile can be seen in Fig. 5.13. The rotational speed is 3,500 rpm and applied load is 4,000 N. With these configurations, the THD simulation could not converge to solutions because the depths of the scratches with the maximum scratch depth in this case is larger than 300 µm, seem larger than the critical scratch depth values. Therefore, an isothermal model with different global temperature values from 45 to 65 °C is used to study this case.

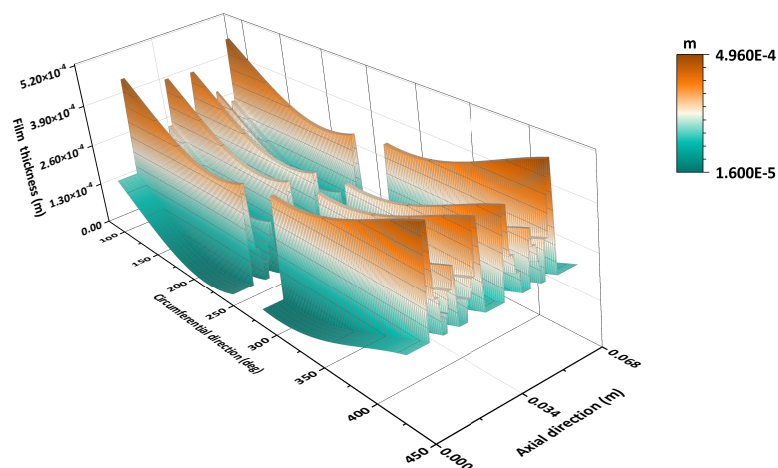


Figure 5.14. 3D view of the fluid film profile.

The results are presented in Fig.5.14 for the 3D fluid film profile with the model with $T=45\text{ }^{\circ}\text{C}$ (it will be denoted as model T45 to avoid repeating). Fig. 5.15 shows simulated 3D profiles of the pressure distribution for three models T45, T50, T55, T60, and T65. Fig. 5.16 presents a THD simulation 3D profile of the pressure of the same bearing without scratch and with the same operating conditions to observe the difference between the non-scratched and scratched cases.

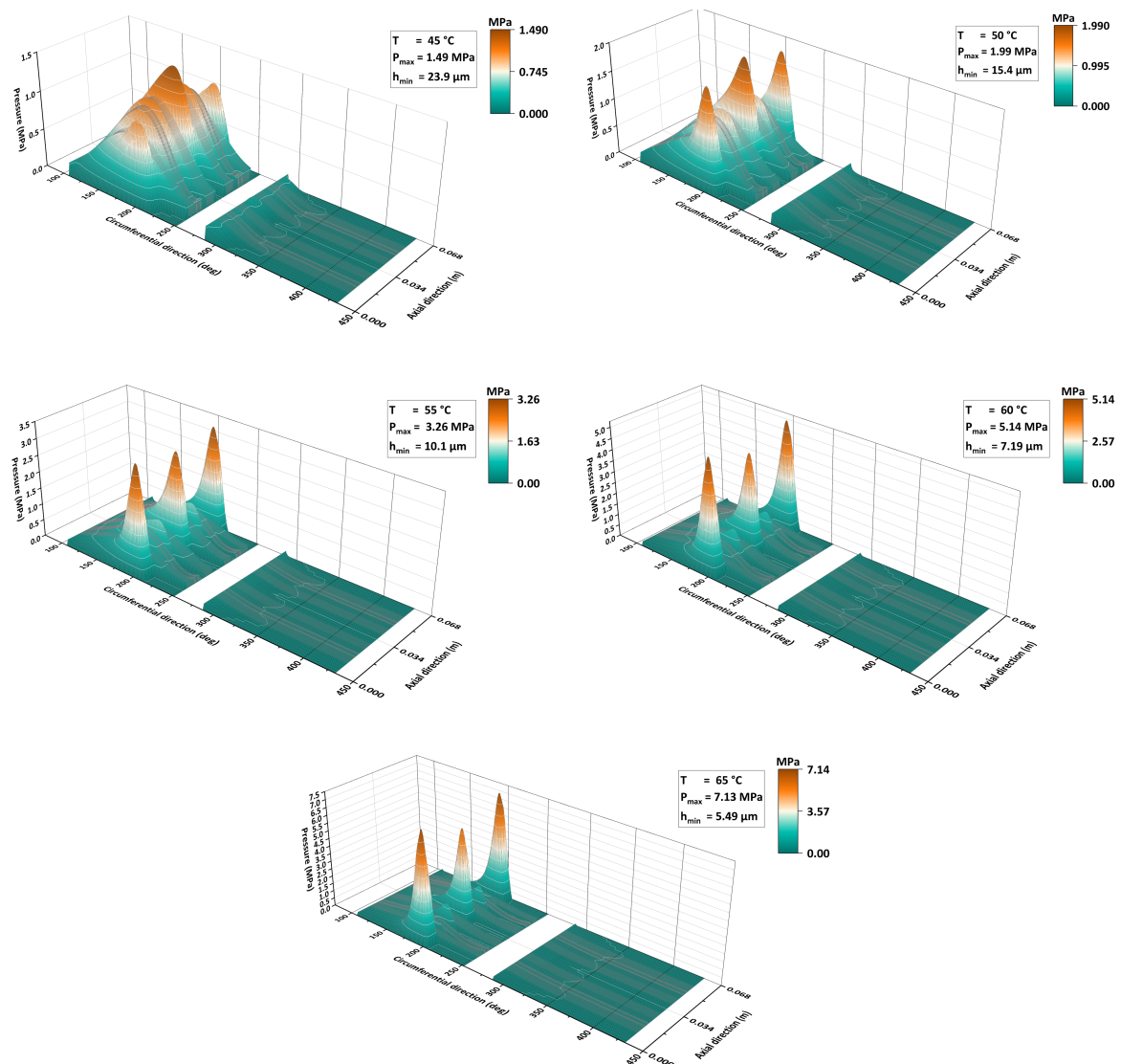


Figure 5.15. 3D profiles of pressure for different global temperatures: $T= 45$ to $65\text{ }^{\circ}\text{C}$.

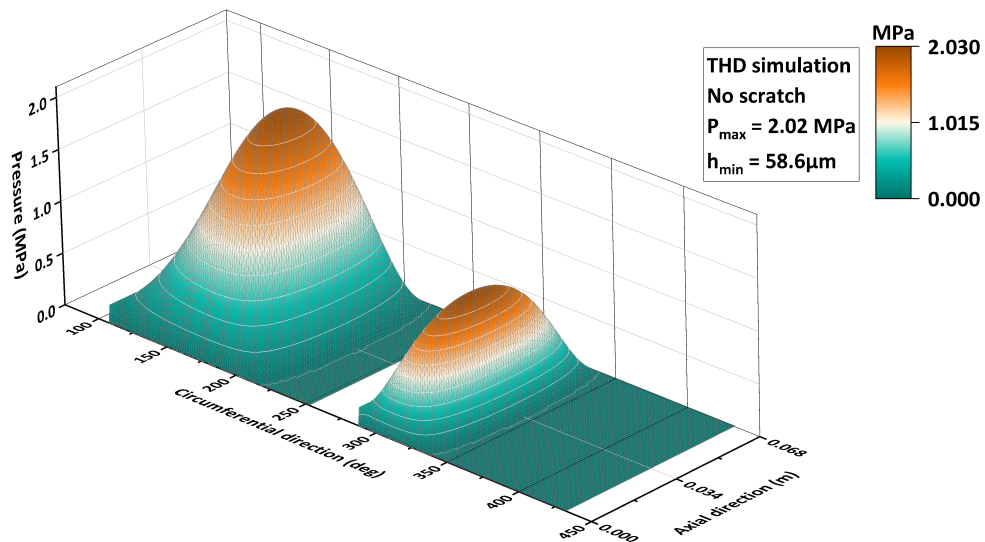
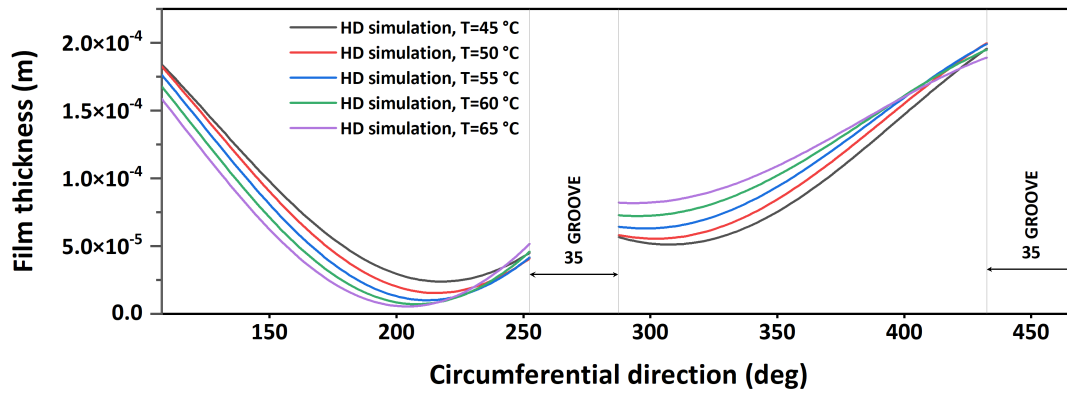
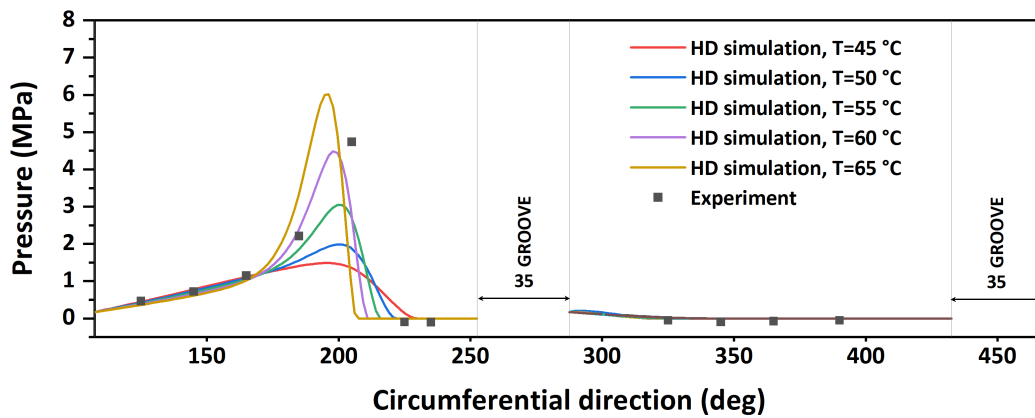


Figure 5.16. 3D profile of THD simulation pressure of a non-scratched bearing with same operating conditions.

It can be seen that the pressure distribution is significantly modified in the scratched bearing. For example, by comparing the results between model T45 and T65, we can see that the minimum film thickness decreases almost by 77% in model T65 (5.49 versus 23.9 μm in model T45) and the maximum pressure increases almost by 379% in model T65 (7.13 versus 1.49 MPa in model T45). Compared to the THD simulation results for non-scratched bearing, the minimum film thickness decreases significantly by 90.63% (58.6 versus 5.49 μm), and it leads to the maximum pressure increase by 253%. It is also noted that with the global thermal effect in model T65, the calculated minimum film thickness is small at 5.49 μm and therefore, it is predicted that a full THD simulation (if converged) highly possibly result in a lower than 5.49 μm in the minimum film thickness because higher thermal effects. It indicates that the scratched bearing should operate in very severe condition with very low minimum film thickness. It is also a possible reason we cannot obtain a full THD simulation solution in this critically damaged bearing.



(a)



(b)

Figure 5.17. Comparisons of film thickness, pressure profiles for results obtained from the models: (a) film thickness in mid-plane, (b) circumferential pressure in mid-plane.

Comparisons of the results obtained from different models and measured data are presented in Figure. 5.17 for the oil film profiles (Fig. 5.17a), and pressure profiles in the mid-plane (Fig. 5.17b). It is clear in Fig. 5.17a that the minimum film thickness obtained from the model T65 is small because of the higher temperature resulting lower viscosity and higher eccentricity. The simulation results of the mid-plane pressures from the models T45, T50, and T55 show large discrepancies compared to measured values (Fig. 5.17b), although the trend is still in a good shape. However, the results from models T60 and T65 are closer to the experimental data and the tendencies are good. It is also noted that without considering the thermal effects and so, the eccentricity is underestimated, and therefore some discrepancies

are observed between the measured and the calculated pressures. It is also possible that the real scratched bearing seems to operate under severe conditions, and it can introduce several other unknowns which the current model has not taken them into account. Although the hydrodynamic model with Reynolds's solutions cannot predict accurately the real pressure distribution, it can simulate the pressure distribution shape and tendencies.

5.8. Conclusions

This chapter presented several numerical studies on the influence of scratch geometry on the performance of scratched journal bearings, velocity profiles, and the limitations of the model. A real case study was also presented with multiple scratches and different scratch depths and widths. Several important results are obtained:

- The scratch width has an influence on both the pressure and temperature distribution, but only significant when the scratch is wide.
- The scratch position has a less significant influence on both the pressure and temperature distribution. The influence decreases when the scratch moved far from the mid-plane of the bearing.
- The number of scratches has a less significant influence on both the pressure and temperature distribution for cases with shallow scratches.
- Importantly, there is a limit or critical value in scratch depth and applied load with the current model for scratched bearings under certain operating conditions. Increasing the scratch depth or the applied load only a little can result in a sudden drop in the calculated minimum film thickness (close to nil), and it leads to an extremely high value on calculated pressures in hydrodynamic calculations or cannot converge in THD calculations.

- Negative velocity, which corresponds to reverse flow, are observed in the scratch regions at the inlets of the bearing.
- In some circumstances, where the THD model cannot converge to solutions because the bearing configurations are not admissible, the hydrodynamic models can be used to study in scratched bearing in terms of the pressure distribution or tendencies.

Conclusions

In this thesis, I have developed and validated a thermohydrodynamic (THD) model that allows to simulate behaviors of scratched journal bearings. The model takes the full known geometry of scratch profiles and thermal effects into account. The model was validated with a variety of data both from scientific literature and experiments conducted at the Pprime Institute. The numerical analysis of the performance of scratched journal bearings are also provided with a variety of configurations of the scratch geometry and operating conditions.

First, we presented brief overviews on hydrodynamic journal bearings with its development history, damage types in hydrodynamic bearings, the current state of studies on the behaviors of scratched journal bearings. Then, theoretical analyses were presented with all necessary equations to determine a full thermohydrodynamic solution for multi-lobe journal bearings lubricated with an incompressible fluid including the generalized Reynolds equation for pressure fields in the film, the energy equation for the temperature of the fluid, the Laplace heat conduction equation for the surrounding solids, boundary conditions. The discretization of the partial differential equations was performed using the finite volume method and then the systems of equations were solved by using the Stone's vectorized strongly implicit procedure. Different meshing techniques for the fluid film were described, especially focused on the discontinuity of the film domain in the axial direction where the scratches located. A Fortran program has been developed and verified by comparing with studies from scientific literature.

To validate the THD model, comparisons between simulation and experimental data were performed for a journal bearing with three cases of different scratch depth (non-scratch, shallow, average, and deep) with a wide of operating conditions, i.e. applied load and rotational speed. The validated model then was applied to study numerically the performance of journal scratched bearings with a wide range of configurations in scratch geometry and bearing operating conditions.

The main results obtained can be described as follows:

- A successful validated thermohydrodynamic model to simulate scratched journal bearings.
- The verifications for non-scratch journal bearings with scientific literature showed very good results for pressure and temperature distribution, and global parameters of the bearings. The validation with experimental data showed: 1) very good agreement in pressure distribution in both of tendency and values; 2) very good agreement in temperature distribution for the low loaded lobe in both of tendency and values and a fair agreement in temperature distribution for the high loaded lobe; 3) good agreements in global parameters of bearing performance.
- It is confirmed that the existence of scratch modified both pressure and temperature distributions. The influence of the scratch is more significant on pressures but less significant in temperatures (observed in experiments and confirmed with the studied THD model).
- On the influence of scratch geometry on the performance of scratched journal bearing: 1) The depth of the scratch is a crucial parameter that strongly influences the journal scratched bearing performance; 2) the scratch width has an influence of the bearing but only significant when the scratch is wide; 3) the scratch position has a less

significant influence on both the pressure and temperature distribution and the influence decreases when the scratch is moving far from the mid-plane of the bearing zone because it is situated in zones of lower hydrodynamic pressure; 4) the number of scratches has a less significant influence on both the pressure and temperature distribution for cases with shallow scratches.

- Negative velocity, which corresponds to reverse flow, are observed in the scratch regions at the inlets of the bearing. The negative flows should be taken into account to calculate more precisely the temperature at the inlets of the bearings.
- It was found that there is a limit or critical value in the scratch depth and applied load for scratched bearings under certain operating conditions. Increasing the scratch depth or the applied load only a little can result in a sudden drop in the calculated minimum film thickness (close to nil), and it leads to very high values on calculated pressure and the model failed to be converged.
- In some circumstances, the THD model cannot converge to solutions because the bearing configurations are not admissible, but solutions can be obtained by using hydrodynamic models. However, the isothermal results obtained in the studied case showed some discrepancies in the pressure distribution compared to experimental data. Therefore, if the isothermal results are to be used in the field to observe the tendency or accurate values, special attention must be paid.

From the results obtained in this these, we believe that the THD model is able to simulate the influence of scratches on the performance of the scratched journal bearings: the film thickness, flow rates, temperature distribution, eccentricity ratio, the attitude angle, and other relevant parameters. In addition, it is able to determine possible critical limits on operation conditions of scratched journal bearings and that of the geometry of scratches. We hope

that the model can be used as a useful tool to enhance our understanding of the behavior of scratched journal bearings and useful for bearing users in order to avoid any serious damage in rotating machinery.

Perspectives

Prospective research could consider the following lines:

- The mechanical and thermal deformations of the shaft, bush, and heat exchange between the bush and bearing supporting system should be taken into account in the model. It may improve the accuracy of the calculated temperature in the high loaded lobe where the current model presented some discrepancies between simulation and experimental data.
- The current model with generalized Reynolds's solutions still has limits, it may be invalid for critical-damaged bearings. In these bearing configurations, when the scratched bearing is operating under severe conditions, it can introduce several unknown parameters which can make the generalized Reynolds's equation invalid. Therefore, deeper analysis and studies on this problem should be considered.
- The application of the current model can be extended to study scratched journal bearings with different scratch cross-section shapes, it also can be applied to study worn journal bearing when considering wear is multiple scratches distributed in a whole area in the bearing; or to study textured journal bearings.

Bibliography

1. Allaire, P.E. || Flack Design of Journal Bearings For Rotating Machinery. **1981**, doi:10.21423/R1FH40.
2. Raimondi, A.A.; Boyd, J. A Solution for the Finite Journal Bearing and Its Application to Analysis and Design: I. ASLE Transactions **1958**, *1*, 159–174, doi:10.1080/05698195808972328.
3. Tanuma, T. Advances in Steam Turbines for Modern Power Plants; Woodhead Publishing **2016**; ISBN 978-0-08-100314-5.
4. Khonsari, M.M.; Booser, E.R. Applied Tribology: Bearing Design and Lubrication; Third edition.; John Wiley & Sons Inc: Hoboken, NJ, **2017**; ISBN 978-1-118-63724-1.
5. Tower, B. First Report on Friction Experiments. Proceedings of the Institution of Mechanical Engineers **1883**, *34*, 632–659, doi:10.1243/PIME_PROC_1883_034_028_02.
6. Dowson, D. History of Tribology; 2.ed.; Professional Engineering Publish: London, **1998**; ISBN 978-1-86058-070-3.
7. Tower, B. Research Committee on Friction: Second Report on Friction Experiments. Proceedings of the Institution of Mechanical Engineers **1885**, *36*, 58–70, doi:10.1243/PIME_PROC_1885_036_011_02.
8. Reynolds, O. IV. On the Theory of Lubrication and Its Application to Mr. Beauchamp Tower's Experiments, Including an Experimental Determination of the Viscosity of Olive Oil. Phil. Trans. R. Soc. **1886**, *177*, 157–234, doi:10.1098/rstl.1886.0005.
9. Kingsbury, A. Experiments with an Air-Lubricated Journal. Journal of the American Society for Naval Engineers **2009**, *9*, 267–292, doi:10.1111/j.1559-3584.1897.tb05692.x.
10. Sommerfeld, A. Zur Hydrodynamischer Theorie Derschiermittelreibung, Zeitschrift Mathematik Physik. **1904**, *50*, 97–155.
11. Gümbel, L. Das Problem Der Lagerreibung. Monatsblätter, Berliner Bezirks Verein Deutscher Ingenieure, VDI **1914**, 87–104 and 109–120.
12. Swift, H.W. The Stability of Lubricating Films In Journal Bearings. (Includes Appendix). Minutes of the Proceedings of the Institution of Civil Engineers **1932**, *233*, 267–288, doi:10.1680/imotp.1932.13239.
13. Stieber, Wilhelm. Das Schwimmlager: Hydrodynamische Theorie des Gleitlagers; VDI-Verlag GmbH: Berlin, **1933**;

14. Dowson, D. Investigation of Cavitation in Lubricating Oil Films Supporting Small Loads. Proc. Instn. Mech. Engrs, Conf. Lubric. & Wear **1957**, 49.
15. Dowson, D. Fundamental Aspects of Cavitation in Bearing. chez 1st Leeds-Lyon conference on cavitation **1974**.
16. Dowson, D.; Taylor, C.M. Cavitation in Bearings. Annu. Rev. Fluid Mech. **1979**, 11, 35–65, doi:10.1146/annurev.fl.11.010179.000343.
17. Braun, M.J.; Hendricks, R.C. An Experimental Investigation of the Vaporous/Gaseous Cavity Characteristics of an Eccentric Journal Bearing. Tribology Transactions **1984**, 27, 1–14, doi:10.1080/05698198408981539.
18. Cristea, A.-F.; Bouyer, J.; Fillon, M.; Pascovici, M.D. Pressure and Temperature Field Measurements of a Lightly Loaded Circumferential Groove Journal Bearing. Tribology Transactions **2011**, 54, 806–823, doi:10.1080/10402004.2011.604758.
19. Braun, M.J.; Hannon, W.M. Cavitation Formation and Modelling for Fluid Film Bearings: A Review. Proceedings of the Institution of Mechanical Engineers, Part J: Journal of Engineering Tribology **2010**, 224, 839–863, doi:10.1243/13506501JET772.
20. Hirn, G. Sur Les Principaux Phenomenes Qui Presentent Les Frottements Medias. Bull. Soc. Ind. Mulhouse **1854**, 26, 188–277.
21. Kingsbury, A. Heat Effects in Lubricating Films. **1933**, 55, 685–688.
22. Clayton, D.; Wilkie, M. Temperature Distribution in the Bush of a Journal Bearing. **1948**, 166, 46–55.
23. Dowson, D. A Generalized Reynolds Equation for Fluid-Film Lubrication. International Journal of Mechanical Sciences **1962**, 4, 159–170, doi:10.1016/S0020-7403(62)80038-1.
24. Tipei, N.; Nica, A.; Beiner, L. A Thermodynamic Analysis of Sliding Bearings. Rev. Roum. Sc. Tech. Mech. Appl. Tome **1970**, 15, 193–217.
25. Tipei, N.; Nica, A.I. On the Field of Temperatures in Lubricating Films. Journal of Lubrication Technology **1967**, 89, 483–491, doi:10.1115/1.3617038.
26. Pinkus, O.; Bupara, S.S. Adiabatic Solutions for Finite Journal Bearings. Journal of Lubrication Technology **1979**, 101, 492–496, doi:10.1115/1.3453400.
27. Hansen, P.K.; Lund, J.W. An Analytical Study of the Heat Balance for a Journal Bearing". CARD Conference Proceedings, AGARD-CP-323 **1982**, 25–1 to 25–9.
28. Lund, J.W.; Hansen, P.K. An Approximate Analysis of the Temperature Conditions in a Journal Bearing. Part I: Theory. Journal of Tribology **1984**, 106, 228–236, doi:10.1115/1.3260890.

29. Boncompain, R.; Frêne, J. Modification de La Portance Due à l' Effet Thermique Dans Les Paliers Lisses – Détermination Des Cartes de Températures. *Méc. Mat. Electr.*, **1978**, 465–474.
30. Boncompain, R.; Frêne, J. Thermohydrodynamic of a Finite Journal Bearing - Static and Dynamic Characteristics. *Proc. of the 6th Leeds-Lyon Symposium* **1980**, 33–41.
31. Mitsui, J.; Hori, Y.; Tanaka, M. Thermohydrodynamic Analysis of Cooling Effect of Supply Oil in Circular Journal Bearing. *Journal of Lubrication Technology* **1983**, 105, 414–420, doi:10.1115/1.3254629.
32. Ferron, J.; Frêne, J.; Boncompain, R. A Study of the Thermohydrodynamic Performance of a Plain Journal Bearing Comparison Between Theory and Experiments. *Journal of Lubrication Technology* **1983**, 105, 422–428, doi:10.1115/1.3254632.
33. Bou-Said, B. La Lubrification à Basse Pression Par La Méthode Des Éléments Finis. Application Aux Paliers, Thèse de Doctorat présentée à l'INSA de Lyon, **1985**.
34. Khonsari, M.M.; Wang, S.H. On the Fluid-Solid Interaction in Reference to Thermoelastohydrodynamic Analysis of Journal Bearings. *Journal of Tribology* **1991**, 113, 398–404, doi:10.1115/1.2920635.
35. Monmousseau, P.; Fillon, M. Transient Thermoelastohydrodynamic Analysis for Safe Operating Conditions of a Tilting-Pad Journal Bearing during Start-Up. *Tribology International* **2000**, 33, 225–231, doi:10.1016/S0301-679X(00)00035-9.
36. Monmousseau, P.; Fillon, M.; Frêne, J. Transient Thermoelastohydrodynamic Study of Tilting-Pad Journal Bearings—Application to Bearing Seizure. *Journal of Tribology* **1998**, 120, 319–324, doi:10.1115/1.2834429.
37. Bouyer, J.; Fillon, M. An Experimental Analysis of Misalignment Effects on Hydrodynamic Plain Journal Bearing Performances. *Journal of Tribology* **2002**, 124, 313–319, doi:10.1115/1.1402180.
38. Bouyer, J.; Fillon, M. Improvement of the THD Performance of a Misaligned Plain Journal Bearing. *Journal of Tribology* **2003**, 125, 334–342, doi:10.1115/1.1510883.
39. Fillon, M.; Bouyer, J. Thermohydrodynamic Analysis of a Worn Plain Journal Bearing. *Tribology International* **2004**, 37, 129–136, doi:10.1016/S0301-679X(03)00051-3.
40. Bouyer, J.; Fillon, M. On the Significance of Thermal and Deformation Effects on a Plain Journal Bearing Subjected to Severe Operating Conditions. *Journal of Tribology* **2004**, 126, 819–822, doi:10.1115/1.1792678.
41. Giraudeau, C. Influence des discontinuités géométriques sur les performances des paliers en régime thermoélastohydrodynamique (TEHD), Thèse de Doctorat présentée à l'Université de Poitiers, **2016**.

42. Bouyer, J.; Fillon, M.; Helene, M.; Beurain, J.; Giraudeau, C. Behavior of a Two-Lobe Journal Bearing with a Scratched Shaft: Comparison Between Theory and Experiment. *Journal of Tribology* **2018**, 141, doi:10.1115/1.4041363.
43. Blair, B.J.; Pethybridge, G. Hydrodynamic Bearing Damage and Remediation of Contributing Factors in Rotating Machinery. 9th EDF/Pprime (LMS) Poitiers Workshop **2010**.
44. Conway-Jones, J.M.; Leopard, A.J. Plain Bearing Damage. Proceedings of the Fourth Turbomachinery Symposium **1976**.
45. Zeidan, F.Y. ||Herbage Fluid Film Bearing Fundamentals And Failure Analysis. **1991**, doi:10.21423/R1D950.
46. Branagan, L. Survey of Damage Investigation of Babbitted Industrial Bearings. *Lubricants* **2015**, 3, 91–112, doi:10.3390/lubricants3020091.
47. Lynwander, P. Gear Drive Systems: Design and Application; Mechanical engineering; M. Dekker: New York, **1983**; ISBN 978-0-8247-1896-1.
48. Affonso, L.O.A. 11 - Hydrodynamic Bearings. In *Machinery Failure Analysis Handbook*; Affonso, L.O.A., Ed.; Gulf Publishing Company, **2006**; pp. 125–142 ISBN 978-1-933762-08-1.
49. Glacier Metal Co., Ltd. Bearing Damage; Glacier Metal Co., Ltd., **1985**.
50. Kingsbury, Inc. A Principles, Operation and Troubleshooting of Hydrodynamic Bearings **2015**.
51. MS Motorservice International GmbH. Damage to Engine Bearings, **2020**.
52. Dobrica, M.B.; Fillon, M. Performance Degradation in Scratched Journal Bearings. *Tribology International* **2012**, 51, 1–10, doi:10.1016/j.triboint.2012.02.003.
53. Giraudeau, C.; Bouyer, J.; Fillon, M.; Hélène, M.; Beurain, J. Experimental Study of the Influence of Scratches on the Performance of a Two-Lobe Journal Bearing. *Tribology Transactions* **2017**, 60, 942–955, doi:10.1080/10402004.2016.1238528.
54. Chatterton, S.; Pennacchi, P.; Vania, A.; Hassini, M.A.; Kuczkowiak, A. Effect of Scratches on a Tilting-Pad Journal Bearing. In Proceedings of the GT2020; Volume 10B: Structures and Dynamics **2020**.
55. Bouyer, J.; Alexandre, Y.; Fillon, M. Experimental Investigation on the Influence of a Multi-Scratched Shaft on Hydrodynamic Journal Bearing Performance. *Tribology International* **2021**, 153, 106543, doi:10.1016/j.triboint.2020.106543.
56. Chapman, S.J. Fortran for Scientists and Engineers; Fourth edition.; McGraw-Hill Education: New York, NY, **2018**; ISBN 978-0-07-338589-1.

57. Bonneau, D. Hydrodynamic Bearings; Numerical methods in engineering series; ISTE Ltd; John Wiley and Sons Inc: London, UK : Hoboken, NJ, **2014**; ISBN 978-1-84821-681-5.
58. Bonneau, D.; Fatu, A.; Souchet, D. Thermo-Hydrodynamic Lubrication in Hydrodynamic Bearings; Numerical methods in engineering series; ISTE; Wiley: London, UK: Hoboken, NJ, **2014**; ISBN 978-1-84821-683-9.
59. Versteeg, H.K.; Malalasekera, W. An Introduction to Computational Fluid Dynamics: The Finite Volume Method; 2nd ed.; Pearson Education Ltd: Harlow, England; New York, **2007**; ISBN 978-0-13-127498-3.
60. Patankar, S.V. Numerical Heat Transfer and Fluid Flow; Series in computational methods in mechanics and thermal sciences; Hemisphere Publ. Co: New York, **1980**; ISBN 978-0-89116-522-4.
61. Ferziger, J.H.; Peric, M. Computational Methods for Fluid Dynamics; 3rd, rev. ed ed.; Springer: Berlin; New York, **2002**; ISBN 978-3-540-42074-3.
62. Stone, H.L. Iterative Solution of Implicit Approximations of Multidimensional Partial Differential Equations. *SIAM J. Numer. Anal.* **1968**, 5, 530–558, doi:10.1137/0705044.
63. Mazumder, S. Numerical Methods for Partial Differential Equations: Finite Difference and Finite Volume Methods; Academic Press: Amsterdam, **2016**; ISBN 978-0-12-849894-1.
64. Stone, Harold.J. An Efficient Parallel Algorithm for the Solution of a Tridiagonal Linear System of Equations. *Journal of the association for computing machinery* **1973**, 20, 27–38.
65. A Guidebook to Fortran on Supercomputers; Elsevier, **1989**; ISBN 978-0-12-444760-8.
66. Leister, H. –J.; Peric, M. Vectorized Strongly Implicit Solving Procedure for a Seven-diagonal Coefficient Matrix. *Int Jnl of Num Meth for HFF* **1994**, 4, 159–172, doi:10.1108/EUM0000000004106.
67. Boncompain, R.; Fillon, M.; Frêne, J. Analysis of Thermal Effects in Hydrodynamic Bearings. *Journal of Tribology* **1986**, 108, 219–224, doi:10.1115/1.3261166.
68. Lund, J.W.; Tonnesen, J. An Approximate Analysis of the Temperature Conditions in a Journal Bearing. Part II: Application. *Journal of Tribology* **1984**, 106, 237–244, doi:10.1115/1.3260891.
69. Bouyer, J. Experimental Study of the Influence of the Position, Shape and Number of Journal Scratches on the Performance of a Two-Lobe Journal Bearing, *STLE* **2018**.
70. Bouyer, J.; Fillon, M. On the Significance of Thermal and Deformation Effects on a Plain Journal Bearing Subjected to Severe Operating Conditions. *Journal of Tribology* **2004**, 126, 819–822, doi:10.1115/1.1792678.

71. Chatterton, S.; Dang, P.V.; Pennacchi, P.; De Luca, A.; Flumian, F. Experimental Evidence of a Two-Axial Groove Hydrodynamic Journal Bearing under Severe Operation Conditions. *Tribology International* **2017**, *109*, 416–427, doi:10.1016/j.triboint.2017.01.014.
72. Dang, P.V.; Chatterton, S.; Pennacchi, P.; Vania, A. Effect of the Load Direction on Non-Nominal Five-Pad Tilting-Pad Journal Bearings. *Tribology International* **2016**, *98*, 197–211, doi:10.1016/j.triboint.2016.02.028.
73. Kucinski, B.-R.; Fillon, M.; Frêne, J.; Pascovici, M.D. A Transient Thermoelastohydrodynamic Study of Steadily Loaded Plain Journal Bearings Using Finite Element Method Analysis. *Journal of Tribology* **1999**, *122*, 219–226, doi:10.1115/1.555346.

List of figures

FIGURE 1.1. TYPES OF BEARING.....	7
FIGURE 1.2. PLAIN JOURNAL BEARING.....	8
FIGURE 1.3. THREE MAIN CATEGORIES OF JOURNAL BEARING (THREE TYPICAL EXAMPLES).....	12
FIGURE 1.4. EXAMPLES OF SCORING [43].....	17
FIGURE 1.5. EXAMPLES OF WIRE WOOLING ON THE JOURNAL AND A THRUST PAD [43].....	18
FIGURE 1.6. EXAMPLES OF MECHANICAL FATIGUE [50].....	20
FIGURE 1.7. AN EXAMPLE OF BABBITT MATERIAL CREEP IN A CYLINDRICAL BEARING [46].....	21
FIGURE 1.8. EXAMPLES SCRATCHES ON HYDRODYNAMIC JOURNAL BEARINGS.....	22
FIGURE 2.1. GEOMETRICAL CHARACTERISTICS OF A THREE-LOBE JOURNAL BEARING.....	28
FIGURE 2.2. GEOMETRY OF A LOBE BEARING, IN SECTION $Z=0$	30
FIGURE 2.3. LUBRICANT FILM UNWRAPPED FOR A TWO-LOBE JOURNAL BEARING WITHOUT GEOMETRICAL PRELOAD.....	31
FIGURE 2.4. AXIS SYSTEM AND NOTATIONS.....	34
FIGURE 2.5. AXIS SYSTEM AND NOTATIONS FOR A DEVELOPED JOURNAL BEARING.....	36
FIGURE 2.6. CAVITATION REPRESENTATION IN THE FILM.....	38
FIGURE 2.7. THERMAL BOUNDARY CONDITIONS OF A FIXED GEOMETRY TWO-LOBE JOURNAL BEARING.....	43
FIGURE 2.8. HYDRODYNAMIC FORCES AND APPLIED BEARING LOAD.....	47
FIGURE 2.9. HEAT BALANCE MODEL IN THE GROOVE REGION OF THE BEARING.....	157
FIGURE 3.1. FINITE VOLUME MESH.....	53
FIGURE 3.2. TYPICAL CONTROL VOLUME.....	54
FIGURE 3.3. STONE'S SEVEN-BAND ITERATION MATRIX $[M]$	59
FIGURE 3.4. $[L]$ AND $[U]$ MATRIX DECOMPOSED FORM MATRIX $[M]$	59
FIGURE 3.5. A 3-D TYPICAL CONTROL VOLUME.....	61
FIGURE 3.6. A 3-D SIP ITERATION MATRIX $[M]$	61
FIGURE 3.7. STRUCTURE OF $[L]$, $[U]$ FOR 3-D SOLUTION.....	62
FIGURE 3.8. A 2-D RESTRUCTURED SCHEME.....	64
FIGURE 3.9. A 3-D RESTRUCTURED SCHEME.....	64
FIGURE 3.10. COMPUTER TIME FOR NON-VECTORIZED SIP VERSUS VECTORIZED SIP.....	65
FIGURE 3.11. A TWO-LOBE JOURNAL BEARING.....	66
FIGURE 3.12. THREE MAIN PARAMETERS OF A SCRATCH ON THE JOURNAL.....	67
FIGURE 3.13. LUBRICANT FILM MESH.....	68

FIGURE 3.14. THREE MESHING METHODS: A) UNIFORM MESH; B) ADAPTIVE MESH REDISTRIBUTION; C) ADAPTIVE MESH REDISTRIBUTION WITH UNIFORM SUBSECTIONS.	69
FIGURE 3.15. FLOW CHART OF THE NUMERICAL PROGRAM.	74
FIGURE 3.16. HMIN ,P _{MAX} , AND POWER LOSS VERSUS ECCENTRICITY.	76
FIGURE 3.17. VOLUME FLOWS AND FLOW BALANCE VERSUS ECCENTRICITY.	76
FIGURE 3.18. LUBRICANT FILM PROFILE OF A NON-SCRATCHED BEARING.	78
FIGURE 3.19. PRESSURE PROFILE OF A NON-SCRATCHED BEARING.	78
FIGURE 3.20. LUBRICANT FILM PROFILE OF A TWO-SCRATCH BEARING.....	79
FIGURE 3.21. PRESSURE PROFILE OF A TWO-SCRATCH BEARING.	79
FIGURE 3.22. VERIFICATION FOR PRESSURE AND TEMPERATURE PROFILE IN MID-PLANE WITH BONCOMPAIN ET AL. RESULTS.....	82
FIGURE 3.23. VERIFICATION FOR PRESSURE PROFILE AT MID-PLANE WITH LUND ET AL. RESULTS.	85
FIGURE 3.24. VERIFICATION FOR TEMPERATURE PROFILE AT MID-PLANE WITH LUND ET AL. RESULTS.	85
FIGURE 4.1. SCHEMATIC VIEW OF THE TEST RIG [70].	88
FIGURE 4.2. LOCATIONS OF PROBES AT INNER SURFACE OF THE BUSH AND POSITIONS OF SCRATCHES [70].	88
FIGURE 4.3. COMPARISON OF PRESSURE PROFILES FOR DIFFERENT SCRATCH DEPTHS: (A) CIRCUMFERENTIAL DIRECTION, IN BEARING MID-PLANE, (B) AXIAL DIRECTION AT ANGLES 185° AND 225°.DEPTH: 0, 90, 135, 214, 260 μM.	91
FIGURE 4.4. COMPARISON OF TEMPERATURE PROFILES FOR MULTIPLE CASES WITH DIFFERENT SCRATCH DEPTHS: (A) CIRCUMFERENTIAL DIRECTION, IN BEARING MID-PLANE, (B) AXIAL DIRECTION AT ANGLES 200°. DEPTH: 0, 90, 135, 214, 260 μM.	92
FIGURE 4.5. COMPARISON OF BEARING GLOBAL PERFORMANCE PARAMETERS: MAXIMUM PRESSURE, MAXIMUM TEMPERATURE, FRICTION TORQUE, AND AXIAL FLOW RATE FOR DIFFERENT SCRATCH DEPTHS.	94
FIGURE 4.6. COMPARISON OF PRESSURE PROFILES FOR DIFFERENT APPLIED LOADS: (A) CIRCUMFERENTIAL DIRECTION, IN BEARING MID-PLANE, (B) AXIAL DIRECTION AT ANGLES 185° AND 225°. LOAD: 6,000; 7,000; 8,000; 9,000; 10,000 N.	98
FIGURE 4.7. COMPARISON OF TEMPERATURE PROFILES FOR DIFFERENT APPLIED LOADS: (A) CIRCUMFERENTIAL DIRECTION, IN BEARING MID-PLANE, (B) AXIAL DIRECTION AT ANGLES 200°. LOAD: 6,000; 7,000; 8,000; 9,000; 10,000 N.....	99
FIGURE 4.8. COMPARISON OF BEARING GLOBAL PERFORMANCE PARAMETERS: MAXIMUM PRESSURE, MAXIMUM TEMPERATURE, FRICTION TORQUE, AND AXIAL FLOW RATE FOR DIFFERENT LOADS.	100
FIGURE 4.9. COMPARISON OF PRESSURE PROFILES FOR DIFFERENT ROTATIONAL SPEEDS: (A) CIRCUMFERENTIAL DIRECTION, IN BEARING MID-PLANE, (B) AXIAL DIRECTION AT ANGLES 185° AND 225°. SPEED: 2,000; 2750, 3500 RPM.....	102
FIGURE 4.10. COMPARISON OF TEMPERATURE PROFILES FOR DIFFERENT ROTATIONAL SPEEDS: (A) CIRCUMFERENTIAL DIRECTION, IN BEARING MID-PLANE, (B) AXIAL DIRECTION AT ANGLES 200°. SPEED: 2,000; 2750, 3500 RPM.	104
FIGURE 4.11. COMPARISON OF BEARING GLOBAL PERFORMANCE PARAMETERS: MAXIMUM PRESSURE, MAXIMUM TEMPERATURE, FRICTION TORQUE, AND AXIAL FLOW RATE FOR DIFFERENT ROTATIONAL SPEEDS.....	105
FIGURE 4.12. COMPARISON OF PRESSURE PROFILES FOR A TWO-SCRATCH BEARING:(A) CIRCUMFERENTIAL DIRECTION, IN BEARING MID-PLANE, (B) AXIAL DIRECTION AT ANGLES 185° AND 225°. SCRATCH DEPTH OF 116 μM, AT L/3 AND 2L/3.	107
FIGURE 4.13. COMPARISON OF TEMPERATURE PROFILES FOR A TWO-SCRATCH BEARING:(A) CIRCUMFERENTIAL DIRECTION, IN BEARING MID-PLANE, (B) AXIAL DIRECTION AT ANGLES 180° AND 200°. SCRATCH DEPTH OF 116 μM, AT L/3 AND 2L/3. .	108

FIGURE 4.14. COMPARISON OF PRESSURE PROFILES FOR A TWO-SCRATCH BEARING: (A) CIRCUMFERENTIAL DIRECTION, IN BEARING MID-PLANE, (B) AXIAL DIRECTION AT ANGLES 185° AND 225°. SCRATCH DEPTH OF 255 μM, AT L/3 AND 2L/3.	110
FIGURE 4.15. COMPARISON OF TEMPERATURE PROFILES FOR A TWO-SCRATCH BEARING: (A) CIRCUMFERENTIAL DIRECTION, IN BEARING MID-PLANE, (B) AXIAL DIRECTION AT ANGLES 180° AND 200°; SCRATCH DEPTH OF 255 μM, AT 5L/12 AND 5L/12.	111
FIGURE 5.1. COMPARISON OF SIMULATION PRESSURE PROFILES FOR DIFFERENT SCRATCH WIDTHS: (A) CIRCUMFERENTIAL DIRECTION, IN BEARING MID-PLANE, (B) AXIAL DIRECTION, IN P _{MAX} PLANE. SCRATCH WIDTH: 1, 2, 4, 8, 16 MM.	115
FIGURE 5.2. COMPARISON OF SIMULATION CIRCUMFERENTIAL TEMPERATURE PROFILES IN BEARING MID-PLANE FOR DIFFERENT SCRATCH WIDTHS. SCRATCH WIDTH: 1, 2, 4, 8, 16 MM.	116
FIGURE 5.3. COMPARISON OF PRESSURE PROFILES FOR DIFFERENT SCRATCH POSITIONS: A) CIRCUMFERENTIAL DIRECTION, IN BEARING MID-PLANE, (B) AXIAL DIRECTION, IN P _{MAX} PLANE.....	118
FIGURE 5.4. COMPARISON OF SIMULATION TEMPERATURE PROFILES FOR DIFFERENT SCRATCH POSITIONS.	119
FIGURE 5.5. COMPARISON OF SIMULATION BEARING GLOBAL PARAMETERS FOR DIFFERENT SCRATCH DEPTHS.	121
FIGURE 5.6. COMPARISON OF SIMULATION BEARING GLOBAL PARAMETERS FOR DIFFERENT APPLIED LOADS.	122
FIGURE 5.7. SLIDING VELOCITY U COMPONENT ACROSS THE FILM THICKNESS IN MID-SCRATCH AT THE INLET OF HIGH LOADED LOBE, WITH DIFFERENT SCRATCH DEPTHS.	124
FIGURE 5.8. SLIDING VELOCITY U COMPONENT ACROSS THE FILM THICKNESS IN MID-SCRATCH AT THE INLET OF HIGH LOADED LOBE: (A) WITH DIFFERENT LOADS, (B) WITH DIFFERENT SPEEDS.....	126
FIGURE 5.9. COMPARISON OF PRESSURE PROFILES FOR DIFFERENT NUMBER OF SCRATCHES: (A) IN MID-PLANE, (B) AT MAXIMUM PRESSURE LOCATION.	128
FIGURE 5.10. COMPARISON OF SIMULATION TEMPERATURE PROFILES FOR DIFFERENT NUMBER OF SCRATCHES.	128
FIGURE 5.11. SCRATCH GEOMETRY OF A SIXTEEN-SCRATCH BEARING.	129
FIGURE 5.12. COMPARISONS OF BEARING GLOBAL PARAMETERS WITH DIFFERENT SIMULATION MODELS: HYDRODYNAMIC SIMULATION T=45 °C, HYDRODYNAMIC SIMULATION T=65 °C, AND THD SIMULATION: (A) FOR MINIMUM FILM THICKNESS, (B) FOR ATTITUDE ANGLE, (C) FOR ECCENTRICITY RATIO, (D) FOR MAXIMUM PRESSURE.	131
FIGURE 5.13. SCRATCH PROFILE.	132
FIGURE 5.14. 3D VIEW OF THE FLUID FILM PROFILE.	132
FIGURE 5.15. 3D PROFILES OF PRESSURE FOR DIFFERENT GLOBAL TEMPERATURES: T= 45 TO 65 °C.	133
FIGURE 5.16. 3D PROFILE OF THD SIMULATION PRESSURE OF A NON-SCRATCHED BEARING WITH SAME OPERATING CONDITIONS.	134
FIGURE 5.17. COMPARISONS OF FILM THICKNESS, PRESSURE PROFILES FOR RESULTS OBTAINED FROM THE MODELS: (A) FILM THICKNESS IN MID-PLANE, (B) CIRCUMFERENTIAL PRESSURE IN MID-PLANE.	135

List of tables

TABLE 3.1. BEARING AND LUBRICANT CHARACTERISTICS.....	67
TABLE 3.2. A COMPARISON AMONG THE THREE METHODS WITH: $N_x=202$, $N_y=122$	71
TABLE 3.3. EFFECT OF NUMBER OF VOLUMES IN CIRCUMFERENTIAL DIRECTION N_x ($N_y=122$, $N_z=140$).....	72
TABLE 3.4. EFFECT OF NUMBER OF VOLUMES IN CROSS-FILM DIRECTION N_y ($N_x=102$, $N_z=140$).....	72
TABLE 3.5. EFFECT OF NUMBER OF VOLUMES IN AXIAL DIRECTION N_z ($N_x=101$, $N_y=122$).....	72
TABLE 3.6. SIMULATIONS WITH IMPOSED APPLIED LOAD, IMPOSED ECCENTRICITY, IMPOSED POSITION FOR NON-SCRATCH AND SCRATCH BEARING.	80
TABLE 3.7. SIMULATION DATA FOR A PLAIN JOURNAL BEARING, NO PRELOAD, AND NO SCRATCH.	81
TABLE 3.8. SIMULATION DATA FOR A TWO-LOBE JOURNAL BEARING, NO PRELOAD, AND NO SCRATCH.....	84
TABLE 4.1. CASES OF VALIDATION.....	89

Appendix A

HEAT BALANCE MODEL IN THE GROOVE REGION OF THE BEARING

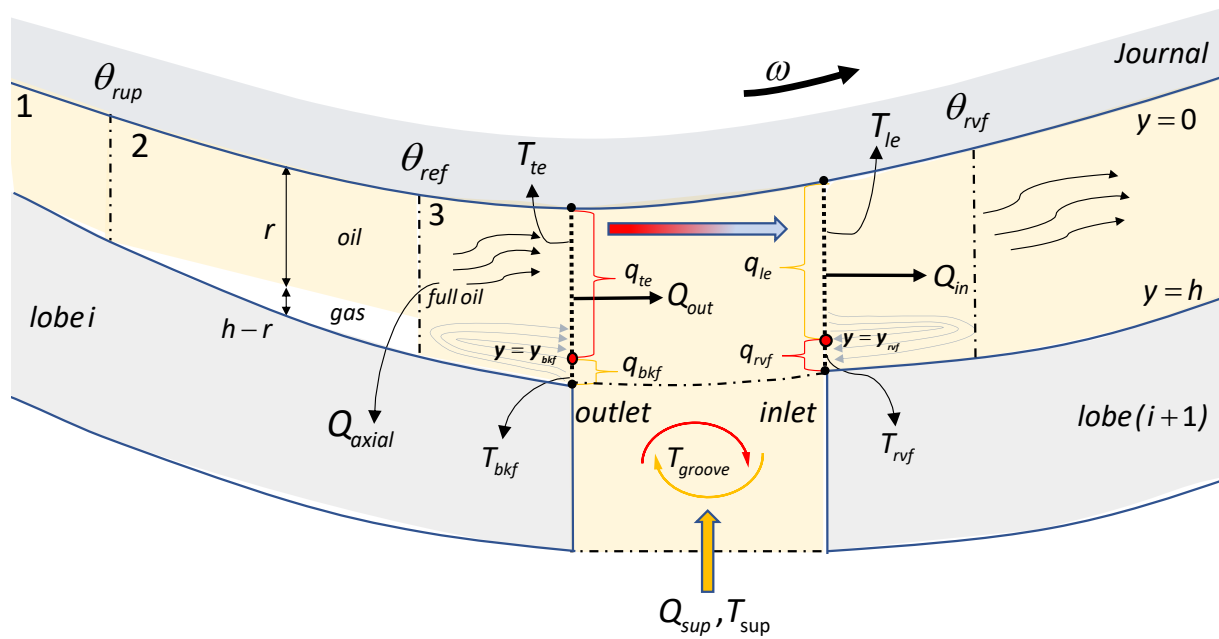


Figure 2.9. Heat balance model in the groove region of the bearing.

Figure 2.9 describes heat fluxes across the boundaries of the groove region considering the oil film reformation, the presence of back flow upstream and reverse flow downstream of the groove. The lubricant film in lobe i is divided into three regions:

- Region 1: full oil film region, starts at a position where the gap is fully filled with oil and ends at the circumferential oil ruptured position θ_{rup} , where oil film starts to rupture.

- Region 2: cavitation region, starts at the ruptured position θ_{rup} and ends at the circumferential reformation position θ_{ref} , where the oil film starts to reform. This zone consists a portion of oil r mixed with a portion of gas $(h-r)$.
- Region 3: reformation region, starts at the oil reformation position θ_{ref} and ends at outlet section. This zone is considered as a full film zone if either the supply oil with a sufficient pressure enters and fills the gas gap in the upstream lubricant film from in the cavitation zone (Figure 2.9) or the height of the gap becomes to be equal or less than the film thickness at the film rupture (this situation occurs for a diverging-converging gap).

At the outlet or the trailing edge of the lobe, due to the supply pressure, oil can go in the opposite direction of the journal rotation to enter the bearing and fill the gas gap of the ruptured oil film from the upstream and creates a full oil film in this region, which is close to the outlet. This flow is defined as the backflow q_{bkf} . At the inlet of the lobe, the same phenomena occur and create the reverse flow. At the inlet of the lobe, a similar phenomenon can appear and create the reverse flow q_{rvf} : this situation occurs for a high journal eccentricity configuration or/and when the film thickness gradient becomes very large (i.e., low value of minimum film thickness).

In the region 1 and 2, the generalized Reynolds and energy equations are solved as normal as in the case which does not consider the reformation of the lubricant near the outlet section of the lobe. In the region 3, due to the supply pressure that might introduce the oil reformation, the backflow, the reverse flow phenomena, the flow rate conservation, and thermal boundary conditions in this region are more complex.

All the notations and details of parameters are described as follows:

- θ_{rup} : oil ruptured circumferential position, where oil film starts to rupture, and the oil film pressure becomes lower than the cavitation pressure.
- θ_{ref} : oil reformation circumferential position
- θ_{rvf} : circumferential position of the extent of the reverse flow zone: the circumferential position where the reverse flow starts and flow up to the groove, at the inlet section.
- y_{bkf} : coordinate (in the across-film direction, y axis) where the back-flow starts, i.e. velocity u component is negative (when back-flow occurs). From this position to the film/bush boundary interface, the oil is going back from the groove into the film, at the outlet section of the lobe.
- y_{rvf} : coordinate (in the across-film direction, y axis) where the reverse flow starts, i.e. velocity u component is negative (when reverse flow occurs). From this position to the film/bush boundary interface, the oil is going from the film into the groove, at the inlet section of the lobe.
- q_{te} : exiting flow rate at the trailing edge of the lobe, where the velocity component u is positive,

$$q_{te} = \int_0^L \int_0^{y_{bkf}} u(x_{out}, y, z) dy dz$$

- q_{bkf} : back-flow rate at the trailing edge of the lobe, where the velocity component u is negative,

$$q_{bkf} = \int_0^L \int_{y_{bkf}}^h u(x_{out}, y, z) dy dz$$

- Q_{out} : net exiting flow rate at the outlet section of the lobe. The net exiting volume flow rate takes into account of the eventual back-flow rate (negative flow rate),

$$Q_{out} = q_{te} + q_{bkf}$$

- q_{le} : entering flow rate at the leading edge of the lobe, where the velocity component u is positive,

$$q_{le} = \int_0^L \int_0^{y_{rvf}} u(x_{in}, y, z) dy dz$$

- q_{rvf} : reverse flow rate at the leading edge of the lobe, where the velocity component u is negative,

$$q_{bkf} = \int_0^L \int_{y_{bkf}}^h u(x_{in}, y, z) dy dz$$

- Q_{in} : net entering flow rate at the inlet section of the lobe. The net entering volume flow rate takes into account of the eventual reverse flow rate (negative flow rate).

$$Q_{in} = q_{le} + q_{rvf}$$

- Q_{axial} : leakage flow rates at the sides of of the lobe, assuming there is no axial flow from the film rupture zone because the axial pressure gradient is nil,

$$Q_{axial}|_{z=0} = \int_{x_{in}}^{R\theta_{rup}} \int_0^h w(x, y, 0) dx dy + \int_{R\theta_{bkf}}^{x_{out}} \int_0^h w(x, y, 0) dx dy$$

$$Q_{axial}|_{z=L} = \int_{x_{in}}^{R\theta_{rup}} \int_0^h w(x, y, L) dx dy + \int_{R\theta_{bkf}}^{x_{out}} \int_0^h w(x, y, L) dx dy$$

$$Q_{axial} = |Q_{axial}|_{z=0}| + |Q_{axial}|_{z=L}|$$

- B_{flow} : flow rate balance in percentage, which represents the mass conservation of all the flows on a given lobe,

$$B_{flow} = 100 \frac{Q_{in} - (Q_{out} + Q_{axial})}{Q_{in}}$$

- Q_{sup} : supply flow rate of fresh oil into the groove, assuming only a part (α) of the exiting flow rate from the previous lobe is recirculating to the following lobe and neglecting the axial flow rate at of both ends for the groove,

$$Q_{sup} = Q_{in} - \alpha Q_{out}$$

- T_{sup} : supply temperature of fresh oil into the groove.
- T_{te} : average temperature of oil at the trailing edge of the lobe (in the zone where velocity component u is positive).
- T_{bkf} : average temperature of oil at the trailing edge of the lobe (in the zone where velocity component u is negative). Note that this temperature will be equal the mixing oil temperature T_{groove} .
- T_{le} : average temperature of oil at the leading edge of the lobe (in the zone where velocity component u is positive). Note that this temperature will be equal the mixing oil temperature T_{groove} .
- T_{rvf} : average temperature of oil at the leading edge of the lobe (in the zone where velocity component u is negative).
- T_{groove} : average temperature of mixing oil inside the groove. T_{groove} is imposed for curly bracket yellow zones at both inlet and outlet sections while the temperature is calculated for curly bracket red zones at both inlet and outlet sections.
- At the outlet section, the boundary temperature of the backflow sub-section is considered equal to the mixed groove temperature while the boundary temperature at the other sub-section is calculated with boundary condition as follows:

$$T|_{x=xout} (at q_{bkf}) = T_{groove}$$

- At the outlet section, the boundary temperature of the reserve sub-section of the flow at the inlet is calculated while the other sub-section is considered equal to the mixed groove temperature:

$$T|_{x=xin} (at q_{le}) = T_{groove}$$

- At the groove, the thermal balance equation can be written as follow:

$$|q_{le}|T_{le} + |q_{bkf}|T_{bkf} = \alpha|q_{te}|T_{te} + |q_{rvf}|T_{rvf} + |Q_{sup}|T_{sup}$$

, where α is the hot oil carry coefficient that represents the portion of hot oil recirculated to the next lobe from the previous one; the value of $\alpha = 1$ means 100 % of the hot oil is recirculated. With above temperature boundary conditions applied, the entering temperature at the leading edge of the lobe can be derived:

$$|q_{le}|T_{groove} + |q_{bkf}|T_{groove} = \alpha|q_{te}|T_{te} + |q_{rvf}|T_{rvf} + |Q_{sup}|T_{sup}$$

$$\Rightarrow T_{le} = T_{groove} = T_{bkf} = \frac{\alpha|q_{te}|T_{te} + |q_{rvf}|T_{rvf} + |Q_{sup}|T_{sup}}{|q_{le}| + |q_{bkf}|}$$

Résumé

Les paliers lisses hydrodynamiques sont des éléments de machine importants utilisés pour supporter les machines tournantes à hautes vitesses telles que les turbines et les compresseurs, en raison de leur durabilité et de leur capacité de charge élevée. Sous des conditions sévères de fonctionnement, ils peuvent s'endommager par une perte de matière qui peut prendre différentes formes, entraînant une chute de la capacité de charge et donc une réduction significative de l'épaisseur du film d'huile. Les rayures sont un type majeur de dommage de surface dans les paliers ; elles peuvent apparaître aussi bien sur la surface du coussinet que sur la surface de l'arbre, induisant de fortes discontinuités géométriques.

Peu de travaux existent dans la littérature mais tous montrent que la présence de rayures a une forte influence sur les performances des paliers. Pour simuler plus précisément et étudier le comportement des paliers lisses rayés, il est donc nécessaire de disposer d'un modèle précis. L'analyse théorique est basée sur la résolution simultanée des équations de Reynolds, d'énergie et de transfert de chaleur dans les solides et dans les fluides. Le modèle thermohydrodynamique développé au moyen de la méthode des volumes finis est écrit en langage FORTRAN. Afin de valider et de compléter la modélisation élaborée, les résultats de la simulation ont été comparés à des données expérimentales de la littérature. Les résultats ont montré de bons accords pour la pression, les profils de température et les paramètres de performance globale du palier. En outre, des études numériques ont également été réalisées pour une large gamme de configurations avec différents nombres de rayures (une, deux et plusieurs), des profondeurs de rayures, des positions de rayures et différents fonctionnements. Les résultats obtenus ont permis d'approfondir les connaissances sur le comportement des paliers lisses rayés.

Mots-clés : *Endommagements de paliers, rayures, lubrification hydrodynamique, paliers, simulations thermohydrodynamiques.*

Abstract

Hydrodynamic plain bearings are important machine components used to support high-speed rotating machinery such as turbines and compressors, due to their durability and high load carrying capacity. Under severe operating conditions, they can be damaged by material loss that can take many forms, resulting in a drop in load capacity and thus a significant reduction in oil film thickness. Scratches are a major type of surface damage in bearings; they can appear on both the bearing surface and the shaft surface, inducing strong geometric discontinuities.

Few works exist in the literature but all show that the presence of scratches has a strong influence on the performance of bearings. In order to simulate more precisely and study the behavior of scratched plain bearings, it is therefore necessary to have an accurate model. The theoretical analysis is based on the simultaneous resolution of Reynolds, energy and heat transfer equations in solids and fluids. The thermohydrodynamic model developed using the finite volume method is written in FORTRAN language. To validate and complete the developed model, the simulation results were compared with experimental data from the literature. The results showed good agreement for pressure, temperature profiles and overall bearing performance parameters. In addition, numerical studies were also performed for a wide range of configurations with different numbers of scratches (one, two and many), scratch depths, scratch positions and different operation. The results obtained have provided further insight into the behavior of scratched plain bearings.

Keywords: *bearing damages, surface scratches, hydrodynamic lubrication, journal bearings, thermohydrodynamic simulations.*